

EDITORIAL OFFICE

EDITOR-IN-CHIEF
Malcolm J. Crocker

MANAGING EDITOR
Marek Pawelczyk

ASSOCIATE EDITORS
Dariusz Bismor
Nickolay Ivanov
Zhuang Li

ASSISTANT EDITORS
Teresa Glowka
Jozef Wiora

EDITORIAL ASSISTANT
Kecie Sharp

EDITORIAL BOARD

Jorge P. Arenas
Valdivia, Chile

Jonathan D. Blotter
Provo, USA

Leonid Gelman
Cranfield, UK

Samir Gerges
Florianópolis, Brazil

Victor T. Grinchenko
Kiev, Ukraine

Colin H. Hansen
Adelaide, Australia

Hanno Heller
Braunschweig, Germany

Hugh Hunt
Cambridge, England

Finn Jacobsen
Lyngby, Denmark

Dan Marghitu
Auburn, USA

Manohar Lal Munjal
Bangalore, India

David E. Newland
Cambridge, England

Kazuhide Ohta
Fukuoka, Japan

Goran Pavic
Villeurbanne, France

Subhash Sinha
Auburn, USA



International Journal of Acoustics and Vibration

A quarterly publication of the International Institute of Acoustics and Vibration

Volume 18, Number 1, March 2013

EDITORIAL

The Jubilee 20th International Congress on Sound
and Vibration (ICSV20)

Malcolm J. Crocker 2

ARTICLES

Numerical and Experimental Studies on the Structure-Borne Noise
Control on a Residential Kitchen Hood

Sinem Öztürk and Haluk Erol 3

Performance of a Base-Isolated Building with System Parameter
Uncertainty Subjected to a Stochastic Earthquake

Sudib K. Mishra and Subrata Chakraborty 7

Experimental Verification of Drill String Vibration Suppression
Using an Adaptive Self-Tuning Controller

*Fesmi Abdul Majeed, Hamad Karki, Mansour Karkoub
and Youssef Lotfy Abdel Magid* 20

An Outward-Wave-Favouring Finite Element-Based Strategy for
Exterior Acoustical Problems

C. S. Jog 27

The Prediction of Nonlinear Responses and Active Stiffness Control
of Moving Slender Continua Subjected to Dynamic Loadings in a
Vertical Host Structure

Stefan Kaczmarczyk and Philip Picton 39

About the Authors 45

INFORMATION

Book Reviews 48



The Jubilee 20th International Congress on Sound and Vibration (ICSV20)

Dear Colleagues,

It is our great pleasure to invite you, together with accompanying persons, to participate in the Jubilee 20th International Congress on Sound and Vibration (ICSV20) to be held from 7 to 11 July 2013 at the Imperial Queen's Park Hotel, Bangkok, Thailand. The ICSV20 is the 20th congress in the series, and several celebratory events are being planned.

Almost 750 abstracts in the fields of acoustics, noise, sound, and vibration from 55 countries have been accepted for presentation. About half of the participants are coming from Asia, including China, Hong Kong, India, Indonesia, Japan, South Korea, Taiwan, Thailand and Vietnam and the rest from Australasia, Europe, Latin America, and North America. Exchange of new findings and ideas is what we anticipate all participants will experience at the ICSV20. This should lead to an expansion of research networks and ultimately strong collaborations between scientists and engineers around the world.

The ICSV20 Scientific Programme will include invited and contributed papers and the following keynote lectures: "Hearing Loss Prevention and Auditory Awareness in the Noisy Workplace" Christian Giguère, Ottawa, Ontario, Canada; "Numerical Prediction of the Signature of Maritime Platforms" Nicole Kessissoglou, Sydney, Australia; "Saving Campbell Diagram for Dynamic Analysis of Complex Rotor Systems" Chong-Won Lee, Taejon, South Korea; "Urban Noise Management and its Practical Implementation" Sergio Luzzi, Florence, Italy; "Statistical Energy Analysis (SEA) Applications in Vibration and Noise" Dhanesh N. Manik, Powai, Mumbai, India; "Applications of the Acoustical Boundary Element Method (BEM) and Related Green's Functions" Martin Ochmann, Berlin, Germany; "Bionic Design of Acoustic Localization System Based on Auditory Orientation Mechanisms" Zhushi Rao, Shanghai, China.

The ICSV20 is sponsored by the International Institute of Acoustics and Vibration (IIAV); the Faculty of Science, Chulalongkorn University; the Acoustical Society of Thailand; and the Science Society of Thailand. The ICSV20 is currently organized in cooperation with the Australian Acoustical Society; the Acoustical Society of China; the Chinese Society of Vibration Engineering; the Hong Kong Institute of Acoustics; the Korean Society for Noise and Vibration Engineering; the Acoustical Society of Singapore; School of Science, Walailak University; and the Pollution Control Department of Thailand.

A special room rates single or double occupancy at the Imperial Queen's Park Hotel, the ICSV20 venue, has been negotiated as follows: Delegate Rates: 90 USD for Deluxe and 107 USD for Premier; Students Rooms single or double occupancy for only 67 USD. These room rates include all taxes, daily breakfast, and free internet access.

The Star Alliance and its members—Adria Airways, Aegean

Airlines, Air Canada, Air China, Air New Zealand, ANA, Asiana Airlines, Austrian Airlines, Brussels Airlines, Croatia Airlines, EgyptAir, Ethiopian Airlines, LOT Polish Airlines, Lufthansa, Scandinavian Airlines, Singapore Airlines, South African Airways, SWISS International Air Lines, TAP Portugal, THAI, Turkish Airlines, United, and US Airways—have been appointed as the official airline network for the ICSV20.

Eighteen exhibitors and sponsors have taken 21 booths: 01dB-Metravib, ACOEM, AM Acoustics, BSWA, DataKustik, ETS Solutions: Larson Davis, G.R.A.S. Sound & Vibration A/S, Geonose, LEGA, LMS, Measuretronix Ltd, Bruel & Kjaer, Microflown Technologies, Norsonic, Polytec, RION, SVANTEK, and Vibration Research Corporation.

Bangkok is a home to numerous conventions and event facilities as well as various kinds of cultural experiences. Having won many international awards, Bangkok is an ideal venue for successful conventions. We are certain that you will enjoy not only the first-rate scientific programme, but also the pleasant environment that Bangkok offers.

The ICSV20 is being held in the exciting country of Thailand, which has a very vibrant culture. A great place to visit, Thailand is one of the world's favourite tourist destinations. This should come as no surprise as Thailand has pristine beaches, coral-fringed islands, world heritage sites, cool mountains, verdant rain forests, fabulous shopping ranging from air-conditioned complexes to the world's largest "flea market," fascinating culture, and typical Thai hospitality. Delegates can experience a variety of unforgettable holiday visits on pre- and post-congress tours in Thailand. You can also visit a number of other countries in Southeast Asia, which are located close to Thailand, such as Cambodia, India, Laos, Malaysia, Myanmar, Nepal, Singapore, and Vietnam. In addition, citizens of most countries do not need a visa, or they can obtain one on arrival.

It is our pleasure to thank Prof. Dr. Supot Han-nongbua, General Chair ICSV20, Dean of Faculty of Science, Chulalongkorn University, Bangkok, Thailand; Prof. Boonchoat Paosawatyanong and Prof. Worawan Bhanthumnavin, Co-Chairs, ICSV20 Local Organising Committee, Chulalongkorn University; Prof. Sorasak Danworaphong, Chair, ICSV20 Technical Programme, Walailak University; and Michel Rosmolen, ICSV20 Exhibition Manager, CEO, Geonose, Bangkok.



Malcolm J. Crocker
Chair, ICSV20 International Organising Committee
Executive Director, International Institute of Acoustics and Vibration (IIAV)

Numerical and Experimental Studies on the Structure-Borne Noise Control on a Residential Kitchen Hood

Sinem Öztürk and Haluk Erol

Istanbul Technical University, Mechanical Engineering Faculty, Gümüßsuyu, 34439, Istanbul, Turkey.

(Received 2 May 2011, revised 27 September 2012, accepted 28 November 2012)

The growing demand for highly efficient household appliances has driven the need for tools to predict, evaluate, and optimize both existing and new designs. Improving the design of the residential kitchen hood requires in-depth knowledge of the structure. In particular, the dynamic behaviour of the structure during the working period needs to be studied carefully during the design stage. A tool for predicting the structure-borne noise behaviour would save a considerable amount of time, reduce the number of prototypes that need to be built, and decrease the development costs. This paper concentrates on reducing the noise generated from the vibrating structure of a residential kitchen hood by using both numerical and experimental methods. Normal modes of the structure were identified, and the results agree well with the finite-element model. To validate the finite element model, an operational deflection-shape analysis of the structure was performed by using the laser Doppler vibrometry method. This study presents the finite element model and the experimental results of a kitchen hood. This study shows that the contribution of structure-borne noise from the vibrating panels to the overall kitchen hood noise levels is significant, especially at low frequencies. Thus, panel vibration is a critical design consideration for end users because of its relationship to noise and comfort.

1. INTRODUCTION

Residential kitchen ventilation is generally used on an intermittent basis. High levels of various contaminants accrue during cooking over a relatively short period of time. The contaminants must be removed quickly and completely, if possible. Kitchen range hoods have been introduced as a solution to these problems. The main function of a typical residential kitchen hood is ventilation. There is an increasing demand for highly efficient, reliable, stylish, and inexpensive range hoods due to the availability of new cooking appliances, and because occupants are increasingly sensitive regarding the issue of indoor air quality. In recent years, the kitchen hood market has become more competitive and requires quick release times for new designs. New designs are expected to be cheaper and to meet higher quality standards with respect to comfort and noise levels. Thus, engineers are required to find alternative design methods to satisfy the market. Once serial manufacturing has started, it is very expensive and difficult to change the design. Design changes can reach the customer within a time period of four months to two years, depending on the magnitude of the changes. Therefore, new methods are required so that the new designs can quickly respond to market conditions. These methods should reduce the engineering costs and must be reliable.

Computer-aided engineering has been widely used as a cost-effective solution for testing new designs. However, the results from the computer-aided engineering software should be validated by using experimental studies. Failing to validate the computational methods can result in serious design errors. For this reason, computer-aided engineering studies should be conducted in parallel with experimental studies. Furthermore, in recent years, the capture efficiency of range hoods has increased. The capacity of the kitchen hood can be improved by increasing the drive unit, preferably without changing the standard external body dimensions. The main source of noise

in kitchen hoods is the vibration that is generated by the drive unit, which consists of a variable speed electric motor and a fan, and by the air flow through the stationary duct. The vibration generated by the drive unit is transmitted to the house through connections. The connections have a complex vibro-acoustical behaviour that is influenced by the various interaction mechanisms. An estimation of the noise produced from a vibrating structure is an important step in the design and development of high-quality kitchen hoods. It is very important to understand the dynamics of a kitchen hood before its construction begins. The most significant challenge that is encountered in noise and vibration control studies of residential kitchen hoods is that generalizing the results is impossible because of the large number of designs of residential kitchen hoods that are used in practice.

A literature review, however, reveals that most research on kitchen hood noise control has been performed by the manufacturers themselves. As a result, the number of publications on this topic is quite limited and may be biased. The first openly available study on the noise control of kitchen hoods was performed by Maggiorana et al.¹ In the study, a combined experimental and theoretical methodology is proposed to address the problem of noise reduction of range hoods. The experimental approach is based on the use of simple microphones and accelerometers to generate a brief characterisation of the noise spectrum and the vibrational characteristics of different models of the product. The second phase of the study is based on theoretical modelling of the structural vibrations and flows by FEM and CFD codes to better understand and identify the primary sources of noise. Once the main problems were identified, some working prototypes of range hoods were created and the possibility of noise reduction was quantified by sound power estimation by using acoustical intensity measurement techniques.

In this study, the noise and the structural vibration behaviour of a residential kitchen hood was analysed by using numeri-

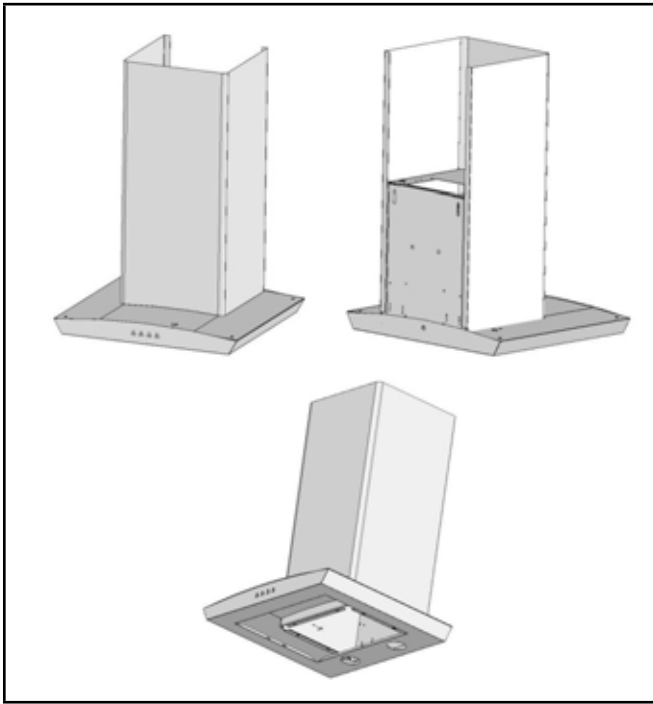


Figure 1. Solid model of the residential kitchen hood and its components.

cal and experimental methods. First, to understand the noise behaviour of the kitchen hood, sound intensity measurements were performed. Then, operational deflection shape measurements were made by using a scanning laser vibrometer. The measurements show that the contribution of structure-borne noise from the vibrating panels to the overall kitchen hood noise levels is significant, especially at low frequencies. Thus, panel vibration is a critical design consideration for end users because of its relationship to comfort and noise. After the initial measurements were made, a numerical model of the kitchen hood was created by using the MSC/Nastran commercial finite-element simulation software. In the numerical model, the panels were modelled as flexible components. The numerical model used in this study has been validated with experimental modal analysis measurements. As a result, an experimentally validated numerical model for a kitchen hood was produced. This model was used to conduct parametric studies for reducing the contribution of structure-borne noise from the vibrating panels to the overall kitchen hood noise levels. A solid model of the residential kitchen hood and its components are shown in Fig. (1).

2. THEORETICAL BACKGROUND

Noise that is produced by vibrating structures such as residential kitchen hoods is often the result of forces and motion that are generated by internal components and transmitted through joints to the structure housing and other supporting structures, which then vibrate and radiate noise into the surrounding areas. To predict the noise radiation with some confidence, the vibration amplitude must be known as a function of its frequency and spatial distribution. Thus, a considerable amount of detail is required for the evaluation of the airborne noise that results from structural vibration.

The radiation ratio, σ , of an arbitrary structure is defined as the sound power radiated by the structure into half space divided by the sound power radiated by a large piston with the same surface area and vibrating with the same root mean

square (RMS) velocity as the structure. The radiation ratio describes the efficiency at which the structure radiates sound compared to a piston of the same surface area. Therefore, for an arbitrary structure with a space-averaged mean-square vibration velocity, \bar{v}^2 , the radiated sound power is

$$\Pi = \rho_0 c S \sigma \langle \bar{v}^2 \rangle, \quad (1)$$

where S is the radiating surface area of the structure, ρ_0 is the density of the fluid medium into which the structure radiates, $\langle \rangle$ represents a time average, $\bar{\quad}$ represents a spatial average, and c is the speed of sound in the fluid medium. It should be noted that the mean-square spatially averaged and time-averaged vibrational velocity is, in fact, the average normal surface velocity. The radiation ratio, σ , provides a powerful relationship between the structural vibrations and the associated radiated sound power. The radiation ratio can be either greater than or less than unity; therefore, it is more appropriate to use the term “ratio,” rather than the term “efficiency,” which is sometimes used in the literature. If the values or relationships for radiation ratios of different types of structural elements can be established, then the estimation of the noise radiation and any subsequent noise control is a relatively easy process—i.e., the radiated sound power can be established directly from the surface vibration levels, which can be obtained either theoretically or experimentally.²

In this study, the structure-borne noise that radiates from the kitchen hood was evaluated using numerically obtained surface vibration levels. To validate the numerical model, an operational deflection shape analysis of the structure was performed by using the laser Doppler vibrometer.

3. NUMERICAL INVESTIGATIONS

To analyse the dynamic behaviour of a residential kitchen hood, a finite-element analysis was conducted by using the general purpose finite-element analysis software, MSC/Nastran. Two types of analyses were performed. Initially, a modal analysis was used to identify the natural frequencies and mode shapes of the structure. Then, a harmonic analysis for three operating speeds was conducted to determine the steady-state response of the residential kitchen hood with a load simulating a variable-speed electric motor that varies sinusoidally with time.

The finite-element model consists of 7560 elements and 12072 nodes. The complete numerical model of the kitchen hood can be seen in our webpage.³ The kitchen hood primarily consists of a formed stainless-steel chassis and a laminated glass front panel. The thickness of the main chassis is 0.60 mm.

It has been shown that the sound power radiated by the structure into half space (i.e., one side of the structure) is proportional to the normal surface velocity.² Therefore, to analyse the structure-borne noise radiated by the kitchen hood surfaces, the normal surface velocity is considered in this study.

4. EXPERIMENTAL STUDIES AND VALIDATION

4.1. Sound Intensity Measurements

Initially, sound intensity measurements were taken for the kitchen hood at three different operating speeds. Sound intensity measurements were performed in accordance with ISO

Table 1. Sound power levels [A-weighted dB].

	(1) Speed [18 Hz]	(2) Speed [24 Hz]	(3) Speed [34 Hz]
Left side	61	68	71
Front	58	64	69
Right side	58	65	68
Total	64	71	74

Table 2. First nine natural frequencies of the kitchen hood.

Experimental [Hz]	Numerical [Hz]
4.40	4.16
4.91	5.92
8.46	8.85
10.11	10.57
13.56	13.60
30.47	29.07
43.56	44.76
48.83	48.83
53.15	52.25

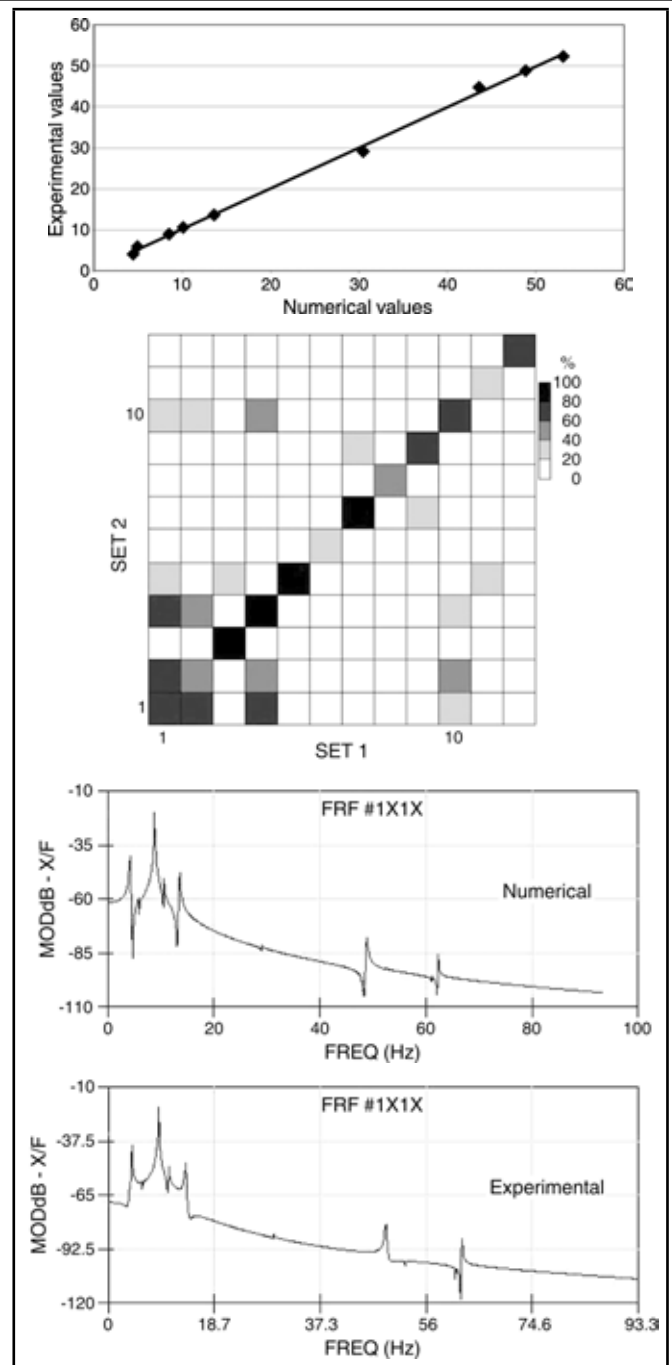
9614. To determine the sound power level, the sound intensity measurements were performed at 88 discrete points on a surface in the form of a rectangular prism. A sound intensity probe (Brüel & Kjær Type 3599), a portable two-channel data acquisition unit, and measurement software (Brüel & Kjær Pulse Type 3560C) were used to conduct the experimental modal analysis. The results from the sound power measurements are summarized in Table 1. The sound intensity mappings on each side of the kitchen hood for the three operating speeds can be seen on our webpage.³ The measurement results indicate that the most significant amount of noise is generated by the shell structure.

Additionally, the new numerical model was solved by using the specified operating conditions, and the results were compared to the measurements of the kitchen hood that was tested under the same conditions. These tests were used to validate the numerical model. The results that were obtained in this study will be used to provide recommendations for the proper use of the numerical model in future studies. To validate the numerical model, two studies were performed on the kitchen hood. First an experimental modal analysis was performed. Then, laser Doppler vibrometry was used to take operational deflection shape measurements for the three operating speeds.

4.2. Modal Analysis

An experimental modal analysis was performed on the kitchen hood. Accelerometers (Brüel & Kjær Type 4507B), a modal hammer (Endevco Type 2302), a portable four-channel data acquisition unit, and general purpose measurement software (Brüel & Kjær Pulse Type 3560D) were used to conduct the experimental modal analysis. First, the measurement points were identified for the experimental modal analysis. Then, to identify the most suitable experimental measurements, preliminary tests were conducted on the experimental models. In each experimental model, the kitchen hood was driven at various points by using the modal hammer to find the most appropriate drive points. Additionally, several suspension positions were tested to determine the most appropriate suspension point.

During the data collection, the measurement period was extended to avoid windowing of the signals. With this extended measurement period, the acceleration measurements converge to zero, which prevents an illusion of leakage. The natural frequencies that resulted from the experimental and numerical modal analysis are shown in Table 2. Table 2 shows that the natural frequencies that were calculated from the numerical model are very close to the natural frequencies that were obtained from the experimental studies. A comparison of the first nine natural frequencies of the housing demonstrates that the

**Figure 2.** Natural frequencies, MAC table, and FRF obtained from experimental and numerical results for the same point on the kitchen hood.

numerical model successfully represents a real system. Figure (2) presents a comparison of the natural frequencies, MAC (Modal Assurance Criterion) table, and the FRF (Frequency Response Function) data that were obtained from the experimental and numerical results for the same point on the housing. In Fig. (2) and Table 2, the natural frequencies that were obtained experimentally are indicated on the horizontal axis, while the natural frequencies that were calculated from the numerical model are indicated on the vertical axis. The natural frequencies are matched according to their order, and a line is drawn through the matching points. The angle of the line is expected to be 45 degrees, and the results show good agreement. Thus, the natural frequencies that were obtained from the numerical and experimental studies are quite consistent. The MAC table shows that the first four mode shapes overlap between 80% and 100%. Higher mode shapes are also con-

Table 3. Calculated overall surface vibration levels according to the existing reference design.

	Operating Speed		
	18 Hz	24 Hz	34 Hz
	Overall surface vibration level [dB]		
Existing design	L_{18}	L_{24}	L_{34}
Case I	$L_{18} - 2.7$	$L_{24} - 1.8$	$L_{34} - 2.8$
Case II	$L_{18} - 8.7$	$L_{24} - 9.8$	$L_{34} - 7.2$
Case III	$L_{18} - 16.5$	$L_{24} - 17.5$	$L_{34} - 14.9$

sistent with high overlap ratios. Figure (2) also shows the FRF data that were obtained at the same point from the experimental and numerical tests. The amplitude and the frequency characteristics are reasonably close for the two data sets.

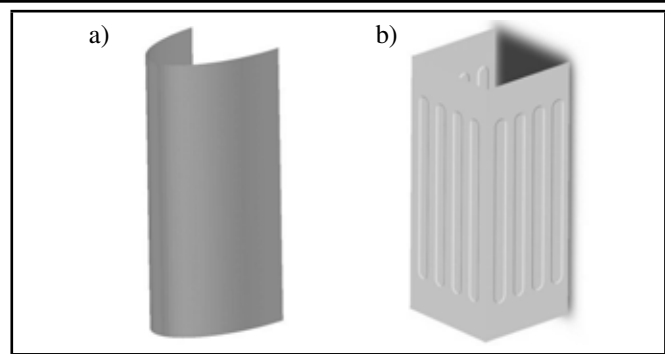
4.3. Operational Deflection Shape Measurements

Operational deflection shapes (ODS) define the dynamic response that the structure exhibits under normal operating conditions. When the residential kitchen hood is operating under steady-state conditions, numerous input forces act on the structure. The potential inputs include, but are not limited to, multi-axial motor vibration, blade imbalance, and airborne noise created from the moving parts. All of these inputs produce responses across the entire structure. The ODS analysis characterizes these responses at selected points throughout the structure with respect to a reference point. Animations of the vibrational response can be generated by using the data that is collected at these points. These animations assist in highlighting areas where the response is large at frequencies of interest, such as the operating frequency and its harmonics. The areas of large response can be correlated to assist in the isolation of particular structure-borne noise components. For the ODS test, the residential kitchen hood was set up normally. The ODS measurements were taken on the kitchen hood for the three operating speeds of 18 Hz, 24 Hz and 34 Hz. Measurements were taken using a Polytec PSV-400 scanning laser Doppler vibrometer. Data acquisition began once the kitchen hood reached its steady-state operating speed. The ODS measurement results for the three operating speeds can be seen on our webpage.³ Along with these results, a distribution of the surface vibrations that were calculated from the numerical model is also presented on our webpage.³ Reasonable agreement was found between the numerical results and the experimentally measured operational deflection shapes.

5. RESULTS AND DISCUSSION

The numerical model can be used to predict the effects that design changes will have on the dynamics of a kitchen hood. In this section, the thickness, shell form, and patterns on the surface of the formed stainless-steel main chassis that had a significant effect on the structure-borne noise behaviour of the kitchen hood are examined. In Case I, the material thickness of a formed stainless-steel main chassis is increased to 1.2 mm. The structural vibration behaviour of the kitchen hood that has an increased thickness compared to the existing hood can be seen on our webpage.³ In this case, the calculated total levels of the surface vibration are less than the existing kitchen hood for each of the three operating speeds. The calculated results are summarized in Table 3.

In Case II, an elliptically shaped kitchen hood is examined by using the numerical model as shown in Fig. 3a). The structural vibration behaviour of the kitchen hood for this case can be seen on our webpage.³ In this case, the calculated total

**Figure 3.** At a) elliptically designed kitchen hood; at b) kitchen hood with patterns on the surface.

levels of the surface vibration are much smaller than the existing kitchen hood for each of the three operating speeds as presented in Table 3.

In the Case III, the kitchen hood with patterns on the surface is examined by using the numerical model as shown in Fig. 3b). The structural vibration behaviour of the kitchen hood for this case can be seen on our webpage.³ In this case, the calculated total levels of the surface vibration are smaller than the existing kitchen hood for the three operating speeds as summarized in Table 3. Of the three case studies, Case III exhibits the largest reduction of the calculated total levels of the surface vibration.

6. CONCLUSIONS

The goal of this study was to construct an engineering design tool that provides a quick and relatively accurate method for determining the structure-borne noise of a residential kitchen hood. To accomplish this goal, a numerical model was developed that uses MSC/Nastran as the FEM simulation software. A good numerical model is beneficial by shortening the product development process and by significantly reducing the cost of prototype development. The software is useful for considering how multiple design variables affect the structure-borne noise of a kitchen hood.

Our numerical method was applied to an existing kitchen hood configuration to compare our numerical predictions with the results that were obtained from experimental measurements. Overall, we found that the experimental and numerical results show acceptable levels of agreement.

This study shows that the contribution of structure-borne noise from the vibrating panels to the overall kitchen hood noise levels is significant, especially at low frequencies. Thus, panel vibration is a critical design consideration for end users because of its relationship to comfort and noise. The parametric studies show that the best design, in terms of structure-borne noise, is the final case study (Case III).

Bibliography

- 1 Maggiorana, P., Rossi, G. L., Morettini, N., Marinelli F., and Morgante, U. Measuring and modelling techniques to approach the problem of noise reduction of domestic kitchen hood, Euronoise, Naples, (2003).
- 2 Norton, M. P. Fundamentals of noise and vibration analysis for engineers, Cambridge University Press, (1989).
- 3 Öztürk, S. and Erol H. Numerical and experimental studies on the structure-borne noise control of a residential kitchen hood, <http://web.itu.edu.tr/erolha/IJAV.html>.

Performance of a Base-Isolated Building with System Parameter Uncertainty Subjected to a Stochastic Earthquake

Sudib K. Mishra

Department of Civil Engineering, Indian Institute of Technology, Kanpur, Uttar Pradesh, India-208016

Subrata Chakraborty

Department of Civil Engineering, Bengal Engineering and Science University, Shibpur, Howrah, West Bengal, India-71103

(Received 21 May 2011, revised 17 February 2012, accepted 14 September 2012)

Base isolation has long been established as an effective tool for improving the seismic performance of structures. The effect of parameter uncertainty on the performance of base isolated structure is investigated in the present study. With the aid of the matrix perturbation theory and first-order Taylor series expansion, the total probability concept is used to evaluate the unconditional response of the system under parameter uncertainty. To do so, the conditional second-order information of responses are obtained by time domain nonlinear random vibration analysis through stochastic linearization. The implications of parametric uncertainty are illustrated in terms of the responses of interest in design applications. The lead rubber bearing isolator, isolating a multistoried building frame, is considered for numerical elucidation. It is observed that, although the randomness in a seismic event dominates, the uncertainty in the system parameters also affects the stochastic responses of the system. Particularly, the variance of the stochastic responses due to parameter uncertainty is notable.

1. INTRODUCTION

Vibration control technologies are widely acclaimed amongst researchers and practicing engineers as a viable alternative to traditional seismic design, which relies on energy dissipation through inelastic deformations of structural elements under earthquake-induced vibrations. In contrast to the traditional design, passive/active vibration control strategies substantially reduce the structural responses to ensure minimal damage to structures. A reduction of response is achieved through control systems, using base isolation (BI), tuned mass dampers, liquid column vibration absorbers, etc. Among these, BI systems have been used and globally accepted as an effective technology to reduce the seismic effects on strategically important structures as well as in retrofitting. In a BI system, the building rests on a system of isolators uncoupling the building from the horizontal component of the ground motion to effectively reduce the seismic load transmission to the structure. Various BI devices, such as rubber bearings (RB), lead rubber bearings (LRB), high-damping rubber bearings (HDRB), friction pendulums (FP), and resilient friction bearing isolators (R-FBI), are conventionally adopted for seismic protection of buildings, bridges, and other infrastructural facilities. These devices use different materials and design strategies to disconnect the superstructure motion from the ground. The effectiveness of BI systems and their performances has been extensively studied.¹⁻⁴ Several studies on stochastic response of base-isolated structures under random earthquakes are also notable.⁵⁻⁷ These studies provide important insight into the

behaviour of structures with BI systems. It is well established that the response of BI systems largely depends on the characteristics of the isolator, such as the yield strength for the LRB and RB types of isolator, optimal damping for R-FBI, and so on. Earlier studies have also provided parameters to ensure optimal performances.⁷⁻⁹ In fact, studies on the optimum design of such systems are well known.⁸⁻¹⁰ However, most of these works are based on deterministic descriptions of the parameters, characterizing the mechanical model of the superstructure-BI system as well as the stochastic load model for the earthquake. A major limitation of the deterministic approach is that the uncertainties in the performance-related decision variables cannot be included in the parameters for the process of optimization. Yet, the efficiency of such a system may be drastically reduced if the parameters are off tuned to the vibrating mode for which it is designed to suppress because of the unavoidable presence of uncertainty in the system parameters. Therefore, the passive vibration control of structures using BI system with uncertain parameters has attracted the interest of the vibration control community.

The developments in the field of passive vibration control by using various passive devices and considering system parameter uncertainty have been improved by many researchers.¹¹⁻¹⁸ However, this is not the case for BI systems. Studies on the performance of BI systems in connection with passive vibration control strategy are very limited. Benfratello et al. indicated that the effect of uncertainty on the response of structure with regard to base isolators and the ground motion filter parameters cannot be ignored.¹⁹ Kawano et al. studied the effect

of uncertain parameters on the nonlinear dynamic response of the BI structure in the framework of Monte Carlo simulation methods.²⁰ It has been demonstrated that uncertain parameters play a significant role on the maximum responses of the BI system. Scruggs et al. proposed a probability-based active control synthesis for seismic isolation of an eight storey base-isolated benchmark structure using uncertain model parameters.²¹ Zhou, Wen, and Cai²² and Zhou and Wen²³ presented two adaptive back-stepping control algorithms for the active seismic protection of building structures using an uncertain hysteretic system. Though studies on the performance of BI systems supplemented by the active vibration control strategies are extensive, the effect of uncertain parameters on the responses and performance of BI systems with passive vibration control is limited.

Thus, in the present study, the effect of system parameter uncertainty on the performance of BI systems is evaluated under a stochastic earthquake load. The response evaluation involves consideration of uncertainty in the properties of the isolated superstructure, isolator, and ground motion characteristics. With the aid of the matrix perturbation theory using first-order Taylor series expansion, the total probability concept is used to evaluate the unconditional response of structures under parameter uncertainty.²⁴ For this, the conditional second-order information of responses are obtained using time domain analysis of nonlinear random vibration by stochastic linearization. Subsequently, the root mean square (RMS) of the top-floor displacement and acceleration (considered to be the performance index) are obtained to study the effect of system parameter uncertainty. Numerical analysis elucidates the effects of parameter uncertainty on the stochastic responses of interest. The implication of the parametric uncertainty is demonstrated in terms of the disparity between the conditional and unconditional stochastic responses and their associated variances.

2. FORMULATIONS

2.1. Response of a Base-Isolated Structure under a Random Earthquake

The structure considered in the present study is idealized as a shear frame isolated by an LRB type of isolator. The idealization of the structure and the LRB is shown in Figs. 1(a) and (b), respectively. Since the BI system substantially reduces the structural response, the isolated structure can reasonably be assumed to behave linearly. The damping of the superstructure is assumed to be the viscous type. The energy is dissipated through the hysteresis of LRB by large shear deformation and by yielding of the lead core. Therefore, the force-deformation behaviour of the LRB is highly nonlinear and is idealized as bilinear (Fig. 1(c))²⁵⁻²⁷ with associated parameters such as yield displacement (q), yield strength (F_Y), pre-yield (k_b), and post-yield stiffness (αk_b). The structure is considered to be excited by the horizontal component of the ground motion only.

The equation of motion for an n -storied superstructure can be expressed as

$$\mathbf{M}\ddot{\mathbf{x}} + \mathbf{C}\dot{\mathbf{x}} + \mathbf{K}\mathbf{x} = -\mathbf{M}\mathbf{r}(\ddot{x}_g + \ddot{x}_b); \quad (1)$$

in which \mathbf{M} , \mathbf{K} , and \mathbf{C} are the mass, stiffness*, and damping matrices of the structure, respectively, of order $n \times n$; $\mathbf{x} = [x_1 \ x_2 \ \dots \ x_n]^T$ is the displacement vector of the superstructure containing the lateral displacement of any floor relative to the isolator, shown in Fig. 1(a). The symbol \mathbf{r} is the influence coefficient vector implying the pseudo-elastic deformation of the respective floor due to a unit deformation of the ground. The symbol \ddot{x}_b is the acceleration of the isolator with respect to the ground and \ddot{x}_g is the earthquake ground acceleration. The details of these matrices are presented in the appendix.

The governing equation of motion for the isolator mass (Fig. 1(b)) can be written as

$$m_b\ddot{x}_b + c_b\dot{x}_b + F_b - c_1\dot{x}_1 - k_1x_1 = -m_b\ddot{x}_g; \quad (2)$$

where m_b is the mass of the base, F_b is the restoring force of the isolator, c_b is the viscous damping in the rubber of the LRB, and k_1 and c_1 are the stiffness and damping of the first storey of the superstructure, respectively.

The bilinear force-deformation behaviour is adopted in this study to model the LRB in which the force-deformation behaviour is expressed by the differential Bouc-Wen model.^{25,26} Following this, the isolator restoring force can be expressed as

$$F_b(x_b, \dot{x}_b, Z) = \alpha k_b x_b + (1 - \alpha)F_y Z; \quad (3)$$

where k_b is the initial elastic stiffness, x_b and \dot{x}_b are the relative displacement and velocity, α is the ratio of post- to pre-yield stiffness (referred as rigidity ratio), and F_y is the yield strength of the LRB. The variable Z is a variable quantifying the hysteretic behaviour of the isolator. Substituting Eq. (3) in Eq. (2) and dividing by m_b , the equation reduces to

$$\ddot{x}_b + \frac{c_b}{m_b}\dot{x}_b + \alpha \frac{k_b}{m_b}x_b + \frac{(1 - \alpha)F_y}{m_b}Z - \frac{c_1}{m_b}\dot{x}_1 - \frac{k_1}{m_b}x_1 = -\ddot{x}_g. \quad (4)$$

The variable Z is governed by the differential equation

$$q\dot{Z} = -\gamma|\dot{x}_b|Z|Z|^{\eta-1} - \beta\dot{x}_b|Z|^\eta + \delta\dot{x}_b; \quad (5)$$

where q is the yield displacement of the isolator. The five parameters β , γ , η , α , and δ in Eq. (5) control the shape of the hysteresis loop. The variable η controls the transition from the elastic to plastic phase; when $\eta \rightarrow \infty$ (infinity), the model becomes elasto-plastic. The nature of the hysteretic behaviour is controlled by β ; $\beta > 0$ implies hardening and $\beta < 0$ results in softening. Presently, the parameters are adopted as $\alpha = 0.05$, $\beta = \gamma = 0.5$, $\delta = 1$, and $\eta = 1$ to correspond the bilinear behaviour. However, such choices lead to smooth transition from the elastic to plastic state, which is adequately taken to be close enough to sharp bilinear behaviour.

The post-yield stiffness of the LRB (αk_b) is selected to provide the specific time period of isolation (T_b), given by

$$T_b = 2\pi\sqrt{\frac{M}{\alpha k_b}}; \quad (6)$$

where $M = \sum_{i=1}^n m_i + m_b$ is the total mass of the isolation-superstructure system, which is the sum of all the floor mass

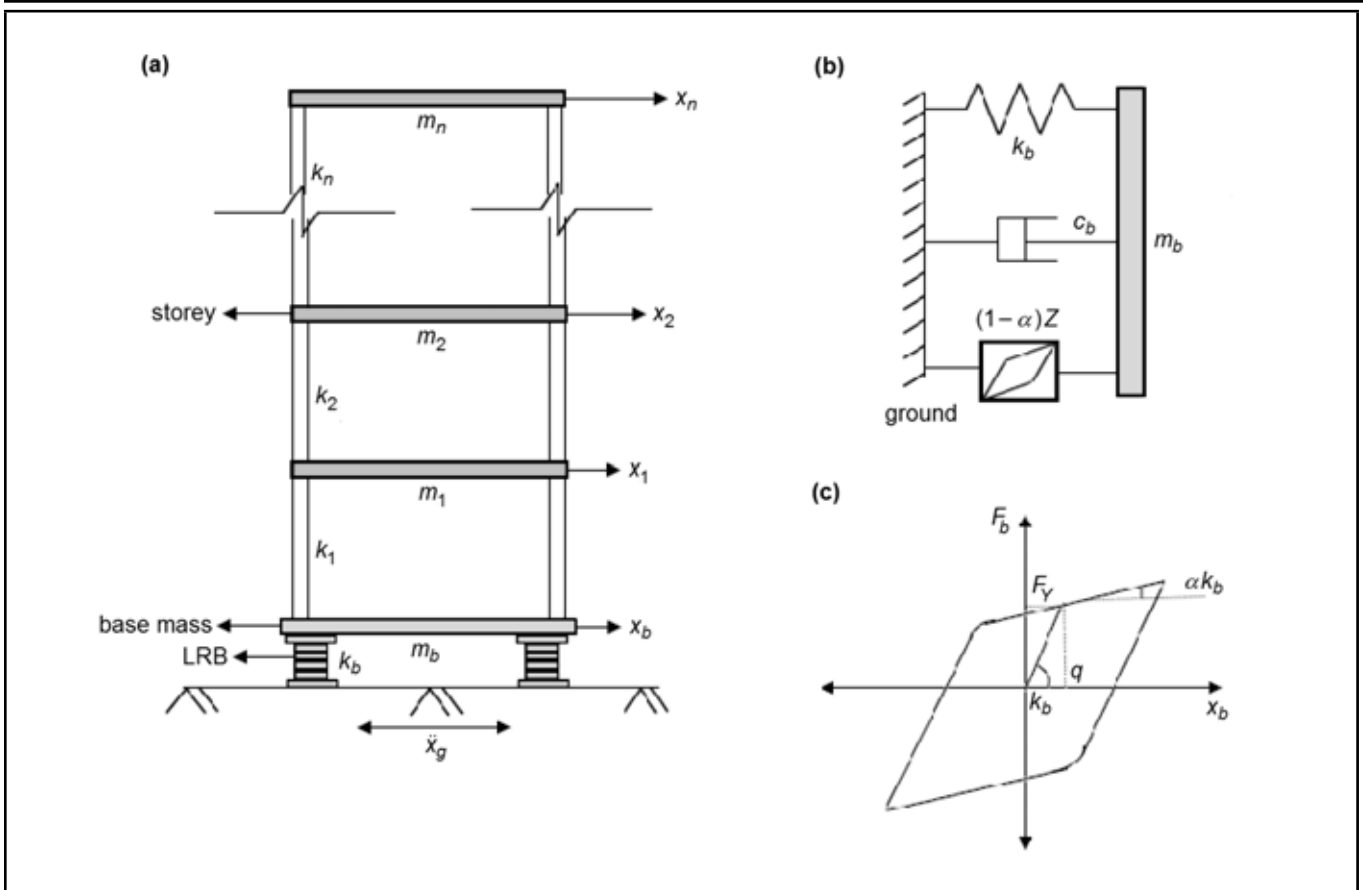


Figure 1. (a) Schematic of the base-isolated structure; (b) Mechanical model of the LRB; and (c) Idealized bilinear hysteresis of the LRB under cyclic loading.

(m_i) and the isolator mass (m_b). The viscous damping (c_b) in the rubber of the LRB is written as

$$c_b = 2\xi_b M\omega_b; \tag{7}$$

where ξ_b is the damping ratio and ω_b is the frequency ($\omega_b = 2\pi/T_b$) of the isolator. The variable q is the displacement corresponding to the yield strength, conveniently normalized (F_0) with respect to the weight ($W = Mg$) of the isolation-structure system:

$$F_0 = \frac{F_Y}{W}; \tag{8}$$

g is the gravitational acceleration. The characteristic parameters of the isolator are, therefore, the time period of isolation (T_b), viscous damping (ξ_b), and the normalized yield strength (F_0). These parameters dictate the performance of isolation in seismic vibration mitigation. The response quantities of the BI system varies monotonically with respect to the isolator time period (i.e., increasing time period reduces the response and vice versa).^{7,8} The response also reduces monotonically with increasing damping for the LRB.^{7,8} However, depending on the type of BI system (e.g., R-FBI), this trend might not be the same, and instead, the optimal value of damping minimizes the response.^{7,8} In the present study, the isolator time period is fixed at 2 s, and the viscous damping in the isolator is taken as 10%.

The nonlinear force-deformation characteristic in Eq. (5) of the LRB is too complicated to be readily incorporated in the state-space formulation for the evaluation of the stochastic responses and the associated sensitivity statistics. This has

been facilitated through stochastic linearization by writing a stochastically equivalent linear form of the nonlinear Eq. (5) as^{27,28}

$$q\dot{Z} + C_e\dot{x}_b + K_e Z = 0; \tag{9}$$

where C_e and K_e are the equivalent damping and stiffness values obtained from the least-square error minimization among the nonlinear equation (Eq. (5)) and the linear equation (Eq. (9)). Presently, for $\eta = 1$, the closed form expressions of the equivalent linear damping and stiffness values are adopted as²⁷

$$C_e = \sqrt{\frac{2}{\pi}} \left\{ \gamma \frac{E[\dot{x}_b Z]}{\sqrt{E[\dot{x}_b^2]}} + \beta \sqrt{E[Z^2]} \right\} - \delta; \tag{10a}$$

$$K_e = \sqrt{\frac{2}{\pi}} \left\{ \gamma \sqrt{E[\dot{x}_b^2]} + \beta \frac{E[\dot{x}_b Z]}{\sqrt{E[Z^2]}} \right\}; \tag{10b}$$

in which $E[]$ is the expectation operator. In stochastic linearization, the responses (x_b, \dot{x}_b) of the system are assumed to be jointly Gaussian. This assumption might not be correct, given that the system is nonlinear in the presence of bilinear hysteresis. However, it is demonstrated that this assumption does not result in serious error so far as the stochastic response evaluation is concerned.^{27,28}

In evaluation of the stochastic response of a structure under a random earthquake, unlike the deterministic time histories, stochastic models are employed to describe the underlying stochastic process. Presently, the well-known Kanai-Tajimi model is considered,^{29,30} the power spectral density of

the ground motion, $S_{\ddot{x}_g}(\omega)$, in this model is expressed as

$$S_{\ddot{x}_g}(\omega) = S_0 \left(\frac{1 + 4\xi_g^2(\omega/\omega_g)^2}{[1 - (\omega/\omega_g)^2]^2 + 4\xi_g^2(\omega/\omega_g)^2} \right); \quad (11)$$

where S_0 is the white-noise intensity of the rock bed excitation responsible for the seismic event; ω_g and ξ_g are the characteristic frequency and damping of the soil media over the rock bed and underlying the building. The variable ω is the frequency component of the ground motion. The parameter S_0 is related to the RMS ground acceleration ($\ddot{u}_{g \max}$) of the earthquake as³¹

$$S_0 = \frac{2\xi_g \ddot{u}_{g \max}}{\pi(1 + 4\xi_g^2)\omega_g}. \quad (12)$$

The state-space formulation can include the white-noise type of ground excitation directly in the formulation, whereas the coloured-noise type of excitation (as in the Kanai-Tajimi model) can be included in the formulation by incorporating the equations for the Kanai-Tajimi filter within the dynamic equations of motion for the superstructure and the isolator. These equations convert the rock bed white noise to colour while passing through the filter. The equations for the Kanai-Tajimi filter can be expressed as

$$\ddot{x}_g = \ddot{x}_f + \ddot{w}; \quad (13a)$$

$$\ddot{x}_f + 2\xi_g\omega_g\dot{x}_f + \omega_g^2x_f = -\ddot{w}. \quad (13b)$$

Substituting Eq. (13b) in Eq. (13a),

$$\ddot{x}_g = -2\xi_g\omega_g\dot{x}_f - \omega_g^2x_f; \quad (14)$$

in which \ddot{w} is the white-noise intensity at the rock bed with power spectral density of S_0 . The variables \ddot{x}_f , \dot{x}_f , and x_f are the response of the Kanai-Tajimi filter. The seismic motion, thus, is introduced in the formulation through incorporating Eq. (13b) and substituting the expression \ddot{x}_g from Eq. (14) in the rest of the equations.

The above equations are now rearranged to represent the state-space form. Multiplying both sides of Eq. (1) with M^{-1} and substituting the expression with $(\ddot{x}_g + \ddot{x}_b)$ from Eq. (4), Eq. (1) can be rewritten as

$$\ddot{\mathbf{x}} = -M^{-1}C\dot{\mathbf{x}} - M^{-1}K\mathbf{x} + \mathbf{r} \left(\frac{c_b}{m_b}\dot{x}_b + \alpha\frac{k_b}{m_b}x_b + \frac{(1-\alpha)F_Y}{m_b}Z - \frac{c_1}{m_b}\dot{x}_1 - \frac{k_1}{m_b}x_1 \right). \quad (15)$$

Similarly, Eq. (2) for the base mass/isolator can be rewritten by dividing both sides by base mass m_b and substituting the expression \ddot{x}_g from the filter Eq. (14) as

$$\ddot{x}_b = -\frac{c_b}{m_b}\dot{x}_b - \alpha\frac{k_b}{m_b}x_b - \frac{(1-\alpha)F_Y}{m_b}Z + \frac{c_1}{m_b}\dot{x}_1 + \frac{k_1}{m_b}x_1 + 2\xi_g\omega_g\dot{x}_f + \omega_g^2x_f. \quad (16)$$

Equation (9) for Z can be rewritten as

$$\dot{Z} = -\frac{C_e}{q}\dot{x}_b - \frac{K_e}{q}Z. \quad (17)$$

Also, the filter equations from Eq. (13b) can be expressed as

$$\ddot{x}_f = -2\xi_g\omega_g\dot{x}_f - \omega_g^2x_f - \ddot{w}. \quad (18)$$

The state variables are introduced in a state vector as

$$\mathbf{Y} = [\mathbf{x}^T \quad x_b \quad Z \quad x_f \quad \dot{\mathbf{x}}^T \quad \dot{x}_b \quad \dot{x}_f]^T. \quad (19)$$

Equations (15)–(18) can be expressed in state-space form as

$$\frac{d}{dt}\mathbf{Y} = \mathbf{A}\mathbf{Y} + \mathbf{w}; \quad (20)$$

where \mathbf{A} is the augmented system matrix and

$$\mathbf{w} = [\mathbf{0} \quad \mathbf{0} \quad \mathbf{0} \quad \mathbf{0} \quad \mathbf{0} \quad \mathbf{0} \quad -\ddot{w}]^T. \quad (21)$$

In the equations above, the vector \mathbf{x} has a dimension equal to the number of structural degrees of freedom (n), and \mathbf{Y} has a size of $(2n + 5)$. The structure of the augmented system matrix \mathbf{A} is provided in the Appendix.

The response of the system can be evaluated by solving Eq. (20). In stochastic dynamic analysis, the statistics, such as covariance of responses, are of interest. It can be shown that the covariance matrix $C_{\mathbf{Y}\mathbf{Y}}$ of the response vector \mathbf{Y} (assumed as Markovian) evolves following an equation of the form³²

$$\frac{d}{dt}C_{\mathbf{Y}\mathbf{Y}} = \mathbf{A}C_{\mathbf{Y}\mathbf{Y}}^T + C_{\mathbf{Y}\mathbf{Y}}\mathbf{A}^T + \mathbf{S}_{\mathbf{w}\mathbf{w}}. \quad (22)$$

$C_{\mathbf{Y}\mathbf{Y}}$ has dimensions of $(2n + 5, 2n + 5)$ with its terms as

$$C_{Y_i Y_j} = E[Y_i Y_j]. \quad (23)$$

The matrix $\mathbf{S}_{\mathbf{w}\mathbf{w}}$ contains a term that quantifies the intensity of the white-noise excitation at the rock bed, denoted as S_0 . Following the structure of \mathbf{w} , matrix $\mathbf{S}_{\mathbf{w}\mathbf{w}}$ has all terms that equal zero, except the last diagonal, which is $2\pi S_0$.

The covariance of responses can be obtained by solving Eq. (22). It should be noted that even though the stochastic linearization is adopted for the nonlinear isolator behaviour, the system still shows the nonlinear characteristics because the equivalent linear stiffness and damping are still functions of the responses

$$C_e = f(\dot{x}_b, Z); \quad K_e = g(\dot{x}_b, Z); \quad (24)$$

where f and g refer to the nonlinear functions of the response quantities \dot{x}_b and Z , the isolator velocity, and hysteretic displacement, respectively (as in Eq. (10a) and (10b)). In solving Eq. (22), these terms are modified in each iteration, following the response statistics of the previous steps. Iterations stops (converges) when the response from two successive steps are practically identical.

The equations for response statistics of their derivative process (such as acceleration $\ddot{\mathbf{x}}$, \ddot{x}_b) are obtained as

$$C_{\dot{\mathbf{Y}}\dot{\mathbf{Y}}} = \mathbf{A}C_{\mathbf{Y}\mathbf{Y}}\mathbf{A}^T + \mathbf{S}_{\mathbf{w}\mathbf{w}}. \quad (25)$$

The RMS responses are obtained from their covariance:

$$\sigma_{Y_i} = \sqrt{C_{Y_i Y_i}}. \quad (26)$$

The absolute top-floor acceleration (\ddot{u}_n) and the relative top-floor displacement (x_n) are two important design parameters for a BI system. The RMS of the top-floor displacement response is given by

$$\sigma_{x_n} = \sqrt{C_{YY}(n, n)}; \quad (27)$$

and the top-floor acceleration (\ddot{u}_n) is obtained by summing up the relative top-floor (\ddot{x}_n), isolator-base (\ddot{x}_b), and the ground acceleration (\ddot{x}_g) as

$$\ddot{u}_n = \ddot{x}_g + \ddot{x}_b + \ddot{x}_n. \quad (28)$$

Then, the RMS top-floor acceleration can be written as

$$\sigma_{\ddot{u}_n} = \sqrt{C_{\dot{Y}\dot{Y}}(2n+3, 2n+3) + C_{\dot{Y}\dot{Y}}(2n+4, 2n+4) + \frac{C_{\dot{Y}\dot{Y}}(2n+5, 2n+5)}{C_{\dot{Y}\dot{Y}}(2n+5, 2n+5)}}; \quad (29)$$

where $\sigma_{\ddot{x}_g}^2 = C_{\dot{Y}\dot{Y}}(2n+3, 2n+3)$, $\sigma_{\ddot{x}_b}^2 = C_{\dot{Y}\dot{Y}}(2n+4, 2n+4)$, and $\sigma_{\ddot{x}_n}^2 = C_{\dot{Y}\dot{Y}}(2n+5, 2n+5)$ are the variance of ground acceleration, acceleration of the isolator, and top-floor acceleration, respectively.

Subsequently, whenever they are discussed, the displacement and accelerations represent the motion of the top floor in the superstructure. The stochastic dynamic analysis, presented herein, is based on an earthquake load modelled as a stationary stochastic process. Extending this analysis to a non-stationary earthquake model will be straight forward. However, doing so will involve evaluating the time-dependent response statistics.

2.2. Sensitivity of Stochastic Response under Parametric Uncertainty

The stochastic response evaluation presented above assumes that the system parameters are deterministic.³³ However, uncertainties in the system parameters may lead to large and unexpected excursion of responses, causing drastic reduction in accuracy and precision of safety evaluation.³⁴ In design of such a system, apart from the stochastic nature of earthquake loading, the uncertainties with regard to these parameters are expected to be influential. The sensitivities of the stochastic responses with respect to the uncertain parameters are essential in considering the effects of parametric uncertainty. The formulation to obtain the sensitivities is presented.

The random variability is reasonably assigned to the parameters of the isolator, the structure, and in the earthquake load, denoted by

$$\theta = [k \quad c \quad k_b \quad c_b \quad F_Y \quad \xi_g \quad \omega_g \quad S_0]^T; \quad (30)$$

where θ is the vector of random design parameters, k is the uniform storey stiffness, c is the uniform damping of each storey, and the other parameters are defined earlier. For simplicity of presentation, uniform storey stiffness and damping are considered herein. However, the proposed formulation is not restricted to such an assumption and can easily be applied for varying values of k and c along different stories. First-order sensitivity of the base of Eq. (22) with respect to the i -th parameter θ_i is written as

$$\frac{d}{dt} \frac{\partial C_{YY}}{\partial \theta_i} = \mathbf{A} \frac{\partial C_{YY}}{\partial \theta_i} + \frac{\partial C_{YY}}{\partial \theta_i} \mathbf{A}^T + \mathbf{B}; \quad (31)$$

in which $\frac{\partial C_{YY}}{\partial \theta_i}$ is the sensitivity of response covariance (C_{YY}) with respect to the parameter θ_i , and \mathbf{B} is defined by

$$\mathbf{B} = \frac{\partial \mathbf{A}}{\partial \theta_i} C_{YY}^T + C_{YY} \frac{\partial \mathbf{A}^T}{\partial \theta_i} + \frac{\partial \mathbf{S}_{ww}}{\partial \theta_i}. \quad (32)$$

It should be noted that Eq. (31) has the same form as Eq. (22) and can be solved similarly. The sensitivity of the time derivative processes (i.e., acceleration) can be obtained with

$$\frac{\partial C_{\dot{Y}\dot{Y}}}{\partial \theta_i} = \mathbf{A} \frac{\partial C_{YY}}{\partial \theta_i} \mathbf{A}^T + \mathbf{B}_1; \quad (33)$$

where

$$\mathbf{B}_1 = \mathbf{A} C_{YY} \frac{\partial \mathbf{A}^T}{\partial \theta_i} + \frac{\partial \mathbf{A}}{\partial \theta_i} C_{YY} \mathbf{A}^T + \frac{\partial \mathbf{S}_{ww}}{\partial \theta_i}. \quad (34)$$

The second-order sensitivity is obtained by further differentiating Eq. (33) with respect to the parameter θ_j . After rearranging the terms, the equation for the second-order sensitivity becomes

$$\frac{d}{dt} \frac{\partial^2 C_{YY}}{\partial \theta_i \partial \theta_j} = \mathbf{A} \frac{\partial^2 C_{YY}}{\partial \theta_i \partial \theta_j} + \frac{\partial^2 C_{YY}}{\partial \theta_i \partial \theta_j} \mathbf{A}^T + \mathbf{C}; \quad (35)$$

where \mathbf{C} is given as

$$\mathbf{C} = \frac{\partial \mathbf{A}}{\partial \theta_j} \frac{\partial C_{YY}}{\partial \theta_i} + \frac{\partial C_{YY}}{\partial \theta_i} \frac{\partial \mathbf{A}^T}{\partial \theta_j} + \frac{\partial^2 \mathbf{A}}{\partial \theta_i \partial \theta_j} C_{YY}^T + \frac{\partial \mathbf{A}}{\partial \theta_i} \frac{\partial C_{YY}}{\partial \theta_j} + C_{YY} \frac{\partial^2 \mathbf{A}^T}{\partial \theta_i \partial \theta_j} + \frac{\partial C_{YY}}{\partial \theta_j} \frac{\partial \mathbf{A}^T}{\partial \theta_i} + \frac{\partial^2 \mathbf{S}_{ww}}{\partial \theta_i \partial \theta_j}. \quad (36)$$

The statistics for the respective time derivative processes are also expressed as

$$\frac{\partial^2 C_{\dot{Y}\dot{Y}}}{\partial \theta_i \partial \theta_j} = \mathbf{A} \frac{\partial^2 C_{YY}}{\partial \theta_i \partial \theta_j} \mathbf{A}^T + \mathbf{C}_1; \quad (37)$$

where \mathbf{C}_1 is given by

$$\mathbf{C}_1 = \mathbf{A} \frac{\partial C_{YY}}{\partial \theta_i} \frac{\partial \mathbf{A}^T}{\partial \theta_j} + \frac{\partial \mathbf{A}}{\partial \theta_j} \frac{\partial C_{YY}}{\partial \theta_i} \mathbf{A}^T + \frac{\partial \mathbf{A}}{\partial \theta_j} C_{YY} \frac{\partial \mathbf{A}^T}{\partial \theta_i} + \mathbf{A} \frac{\partial C_{YY}}{\partial \theta_j} \frac{\partial \mathbf{A}^T}{\partial \theta_i} + \mathbf{A} C_{YY} \frac{\partial^2 \mathbf{A}^T}{\partial \theta_i \partial \theta_j} + \frac{\partial^2 \mathbf{A}}{\partial \theta_i \partial \theta_j} C_{YY} \mathbf{A}^T + \frac{\partial \mathbf{A}}{\partial \theta_i} C_{YY} \frac{\partial \mathbf{A}^T}{\partial \theta_j} + \frac{\partial \mathbf{A}}{\partial \theta_i} \frac{\partial C_{YY}}{\partial \theta_j} \mathbf{A}^T + \frac{\partial^2 \mathbf{S}_{ww}}{\partial \theta_i \partial \theta_j}. \quad (38)$$

Equations (31) and (35) can be solved similarly for first- and second-order sensitivity, respectively. It should be mentioned that some of the matrices involved in Eq. (35) for evaluating \mathbf{C} are null. This is because \mathbf{A} and \mathbf{S}_{ww} have zero-th/first-order terms, which are a function of random variables θ_i , which vanishes after first-/second-order differentiation with respect to θ_i .

The sensitivities of the RMS responses are obtained by differentiating Eq. (26) with respect to the i -th random parameter as

$$\frac{\partial \sigma_{Y_m}}{\partial \theta_i} = \frac{1}{2} \frac{1}{\sqrt{C_{Y_m Y_m}}} \frac{\partial C_{Y_m Y_m}}{\partial \theta_i};$$

$$\frac{\partial^2 \sigma_{Y_m}}{\partial \theta_i \partial \theta_j} = \frac{1}{2} \frac{1}{\sqrt{C_{Y_m Y_m}}} \left[\frac{\partial^2 C_{Y_m Y_m}}{\partial \theta_i \partial \theta_j} - \frac{1}{2} \frac{1}{C_{Y_m Y_m}} \left(\frac{\partial C_{Y_m Y_m}}{\partial \theta_i} \right)^2 \right]. \quad (39)$$

In the above equation, Y_m is the response; σ_{Y_m} is the RMS response of Y_m . The terms $\frac{\partial \sigma_{Y_m}}{\partial \theta_i}$ and $\frac{\partial^2 \sigma_{Y_m}}{\partial \theta_i \partial \theta_j}$ represent the first- and second-order sensitivity with respect to the parameters θ_i and θ_j , respectively.

It should be mentioned here that the system parameter matrix **A**, defined in the Appendix, is an explicit function of uncertain model parameters, θ . Thus, the derivatives can be directly obtained by differentiating with respect to each parameter. However, the formulation does not impose any limit to the number of elements or degrees of freedom used in the analysis. But with an increasing number of elements, the matrices will be bigger to accommodate the computational demand. For more complex super-structural systems, involving finite element modelling for response evaluation, the matrix **A** cannot be obtained explicitly. For implicitly generated element mass, stiffness, and the damping matrix of the system, the differentiation can be carried out through a sequence of calculations or, alternatively, by finite difference approximation and can subsequently be used to obtain the partial derivative of **A**. There are important practical considerations for computing derivatives that are required in structural sensitivity analysis.^{34,35}

2.3. Parameter Uncertainty and Unconditional Stochastic Response

The stochastic response of a structure under earthquake loading depends on the system parameters and can be expanded around the mean value of the uncertain parameters (with the assumption that the random variability is small) using the Taylor series. The random system parameter (θ_i) can be viewed as the superposition of the deterministic mean component ($\bar{\theta}_i$) with a zero mean deviatoric component ($\Delta\theta_i$). Thus, the Taylor series expansion of the RMS response at the mean value of the random parameters can be written as

$$\sigma_{Y_m} = \sigma_{Y_m}(\bar{\theta}_i) + \sum_{i=1}^{nv} \frac{\partial \sigma_{Y_m}}{\partial \theta_i} \Delta\theta_i + \frac{1}{2} \sum_{i=1}^{nv} \sum_{j=1}^{nv} \frac{\partial^2 \sigma_{Y_m}}{\partial \theta_i \partial \theta_j} \Delta\theta_i \Delta\theta_j; \tag{40}$$

in which nv is the total number of random variables involved, and the derivative of the respective response quantities are the sensitivity terms addressed in the previous section. Assuming that the uncertain random variables are uncorrelated, the quadratic approximation provides the expected value of the unconditional RMS response as

$$\sigma_{Y_m} = \sigma_{Y_m}(\bar{\theta}_i) + \frac{1}{2} \sum_{i=1}^{nv} \frac{\partial^2 C_{Y_m Y_m}}{\partial \theta_i^2} \sigma_{\theta_i}^2; \tag{41}$$

where $\sigma_{\theta_i}^2$ is the standard deviation of the i -th random parameter. The linear approximation of the Taylor series expansion furnishes the variance of the RMS response:

$$\text{var}[\sigma_{Y_m}] = \sigma_{\sigma_{Y_m}}^2 = \sum_{i=1}^{nv} \left(\frac{\partial \sigma_{Y_m}}{\partial \theta_i} \right)^2 \sigma_{\theta_i}^2. \tag{42}$$

Such responses are referred to as unconditional because the condition that the structural parameters to be deterministic has been relaxed while estimating such responses.³³

Table 1. Statistical properties of the random system parameters.

Parameters	Mean	Coefficient of variation	Distribution
storey stiffness (k)	5830 kN/m	5%–15%	normal
storey damping (c)	264499.5 kNs/m		normal
isolator stiffness (k_b)	56791296 kN/m		normal
isolator damping (c_b)	10%		normal
isolator yield-strength (F_Y)	5% of total weight (W)		normal
ground damping (ξ_g)	60%		normal
ground frequency (ω_g)	5 rad/s		normal
seismic intensity (S_0)	0.05 m/s ²		normal

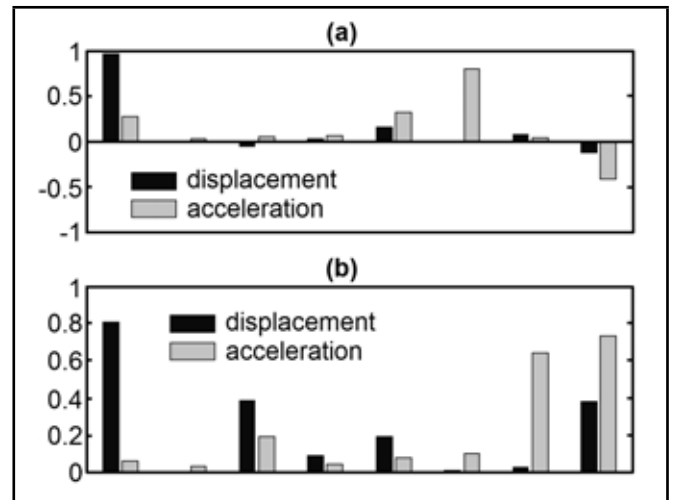


Figure 2. The normalized (a) second-order and (b) first-order terms dictating the contribution of individual stochastic parameters in affecting the unconditional response and their variances.

3. NUMERICAL ILLUSTRATIONS

A five-storied shear building ($n = 5$) is studied to investigate the effects of parametric uncertainty on the performance of a BI system subject to stochastic earthquake. The mass, stiffness, and damping (m_i, k_i, ξ_i) of each floor are assumed to be identical. The values of stiffness and mass for each storey are assigned to provide the desired value of time period (T) to the superstructure (varying from 0.1 s to 1 s) employed for parametric study. The uniform viscous damping ratio (ξ) is taken as 2%, unless specifically mentioned. The LRB is characterized with a mass ratio (m_b/m) of 1, the viscous damping ratio (ξ_b) of 10%, and the normalized yield strength (F_0) of 0.05, unless otherwise specified. The parameters characterizing the random earthquakes are ω_g, ξ_g , and S_0 . All random parameters in the study are assumed to be statistically independent, normally distributed, and the properties are listed in Table 1.

In prior to present the response of the BI system under parameter uncertainty, the relative importance of the random system parameters are studied through a bar chart sensitivity analysis (see Figs. 2(a) and 2(b)) in order to assess the contribution of the individual random variable in affecting the responses (shown in Eqs. (41) and (42)). In these figures, the first- and second-order sensitivity terms are multiplied by the variance of the respective random variables. While plotting, the terms are normalized with respect to the square root of sum of all squared terms. For first-order terms (governing the variance of

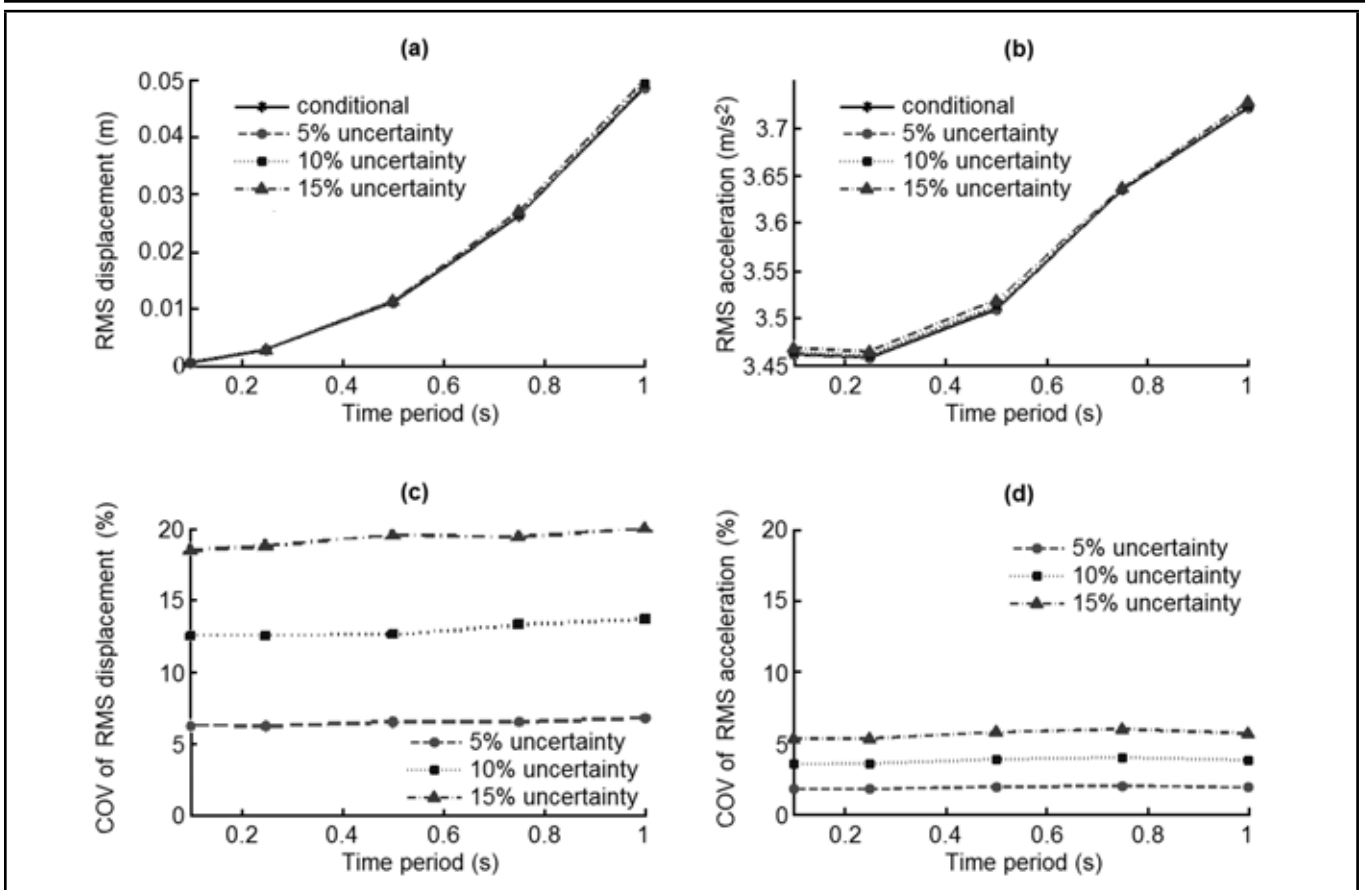


Figure 3. Conditional and unconditional RMS top-floor (a) displacement and (b) acceleration, and coefficient of variation of top-floor (c) displacement and (d) acceleration with varied superstructure flexibilities and different degrees of uncertainty.

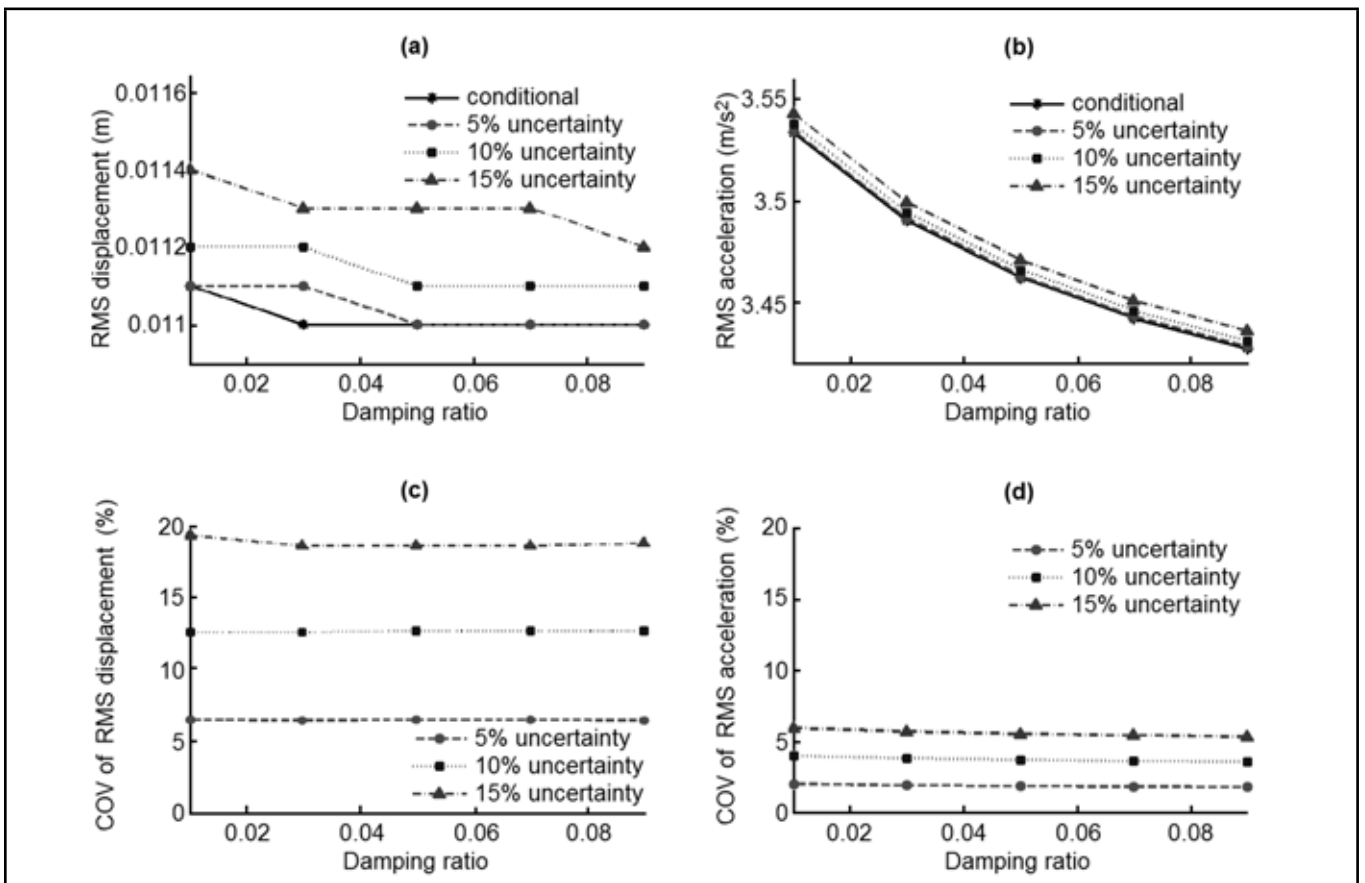


Figure 4. Conditional and unconditional RMS top-floor (a) displacement and (b) acceleration, and coefficient of variation of top-floor (c) displacement and (d) acceleration with varied superstructure damping for different degrees of uncertainty.

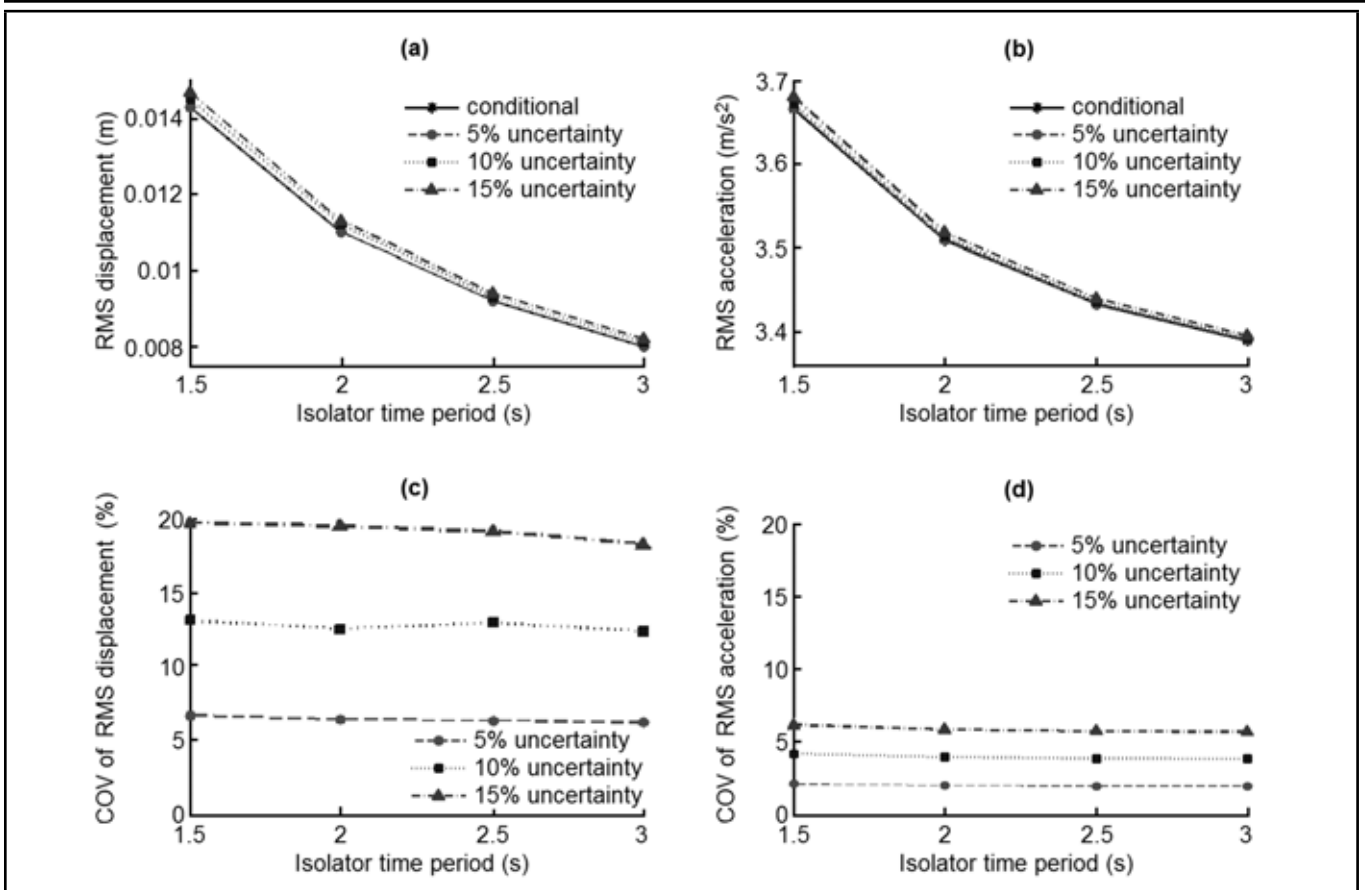


Figure 5. Conditional and unconditional RMS top-floor (a) displacement and (b) acceleration, and coefficient of variation of top-floor (c) displacement and (d) acceleration with varied isolation time period and different degrees of uncertainty.

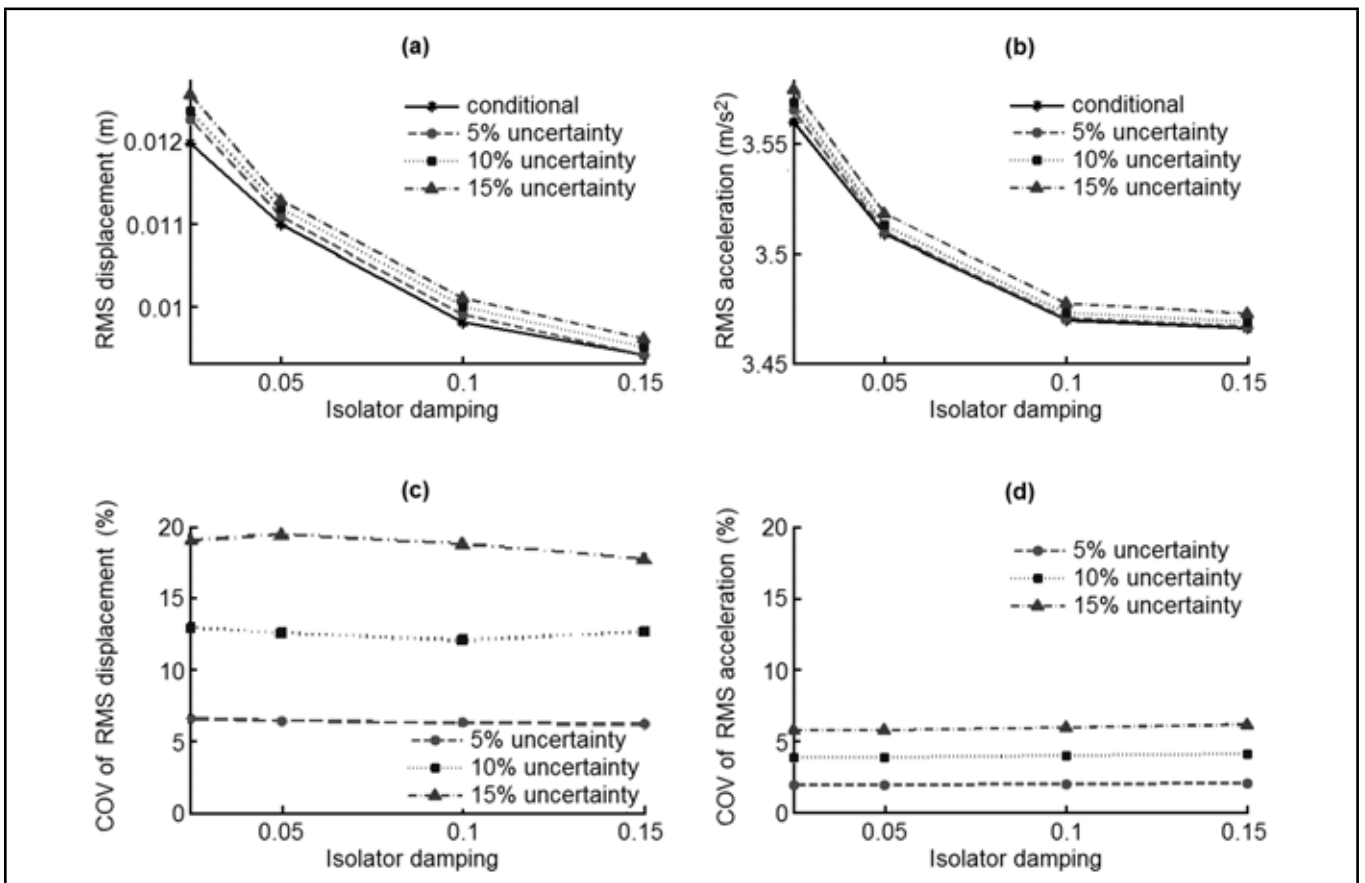


Figure 6. Conditional and unconditional RMS top-floor (a) displacement and (b) acceleration, and coefficient of variation of top-floor (c) displacement and (d) acceleration with varied isolation damping and different degrees of uncertainty.

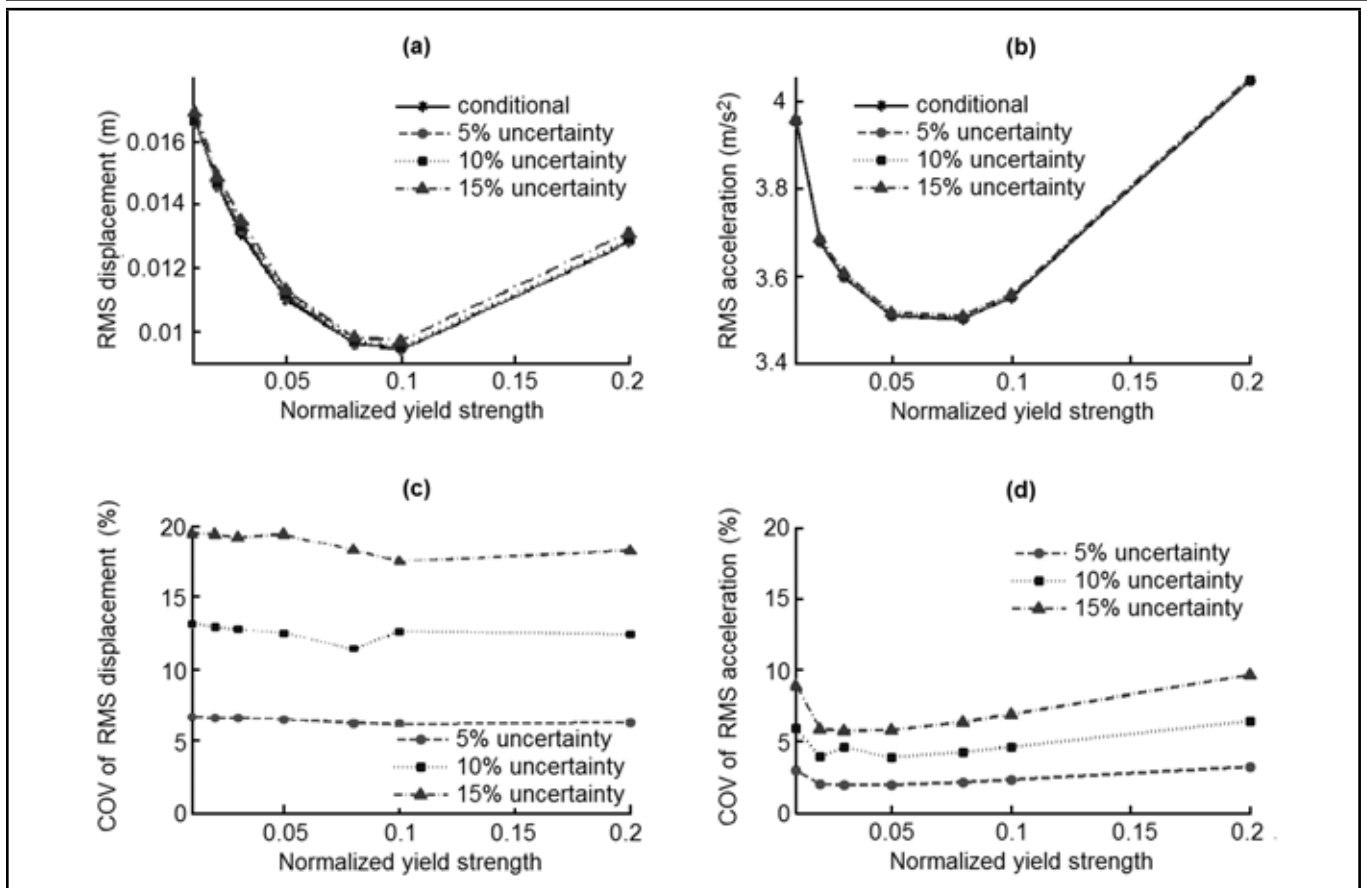


Figure 7. Conditional and unconditional RMS top-floor (a) displacement and (b) acceleration, and coefficient of variation of top-floor (c) displacement and (d) acceleration with varied yield strength of isolator and different degrees of uncertainty.

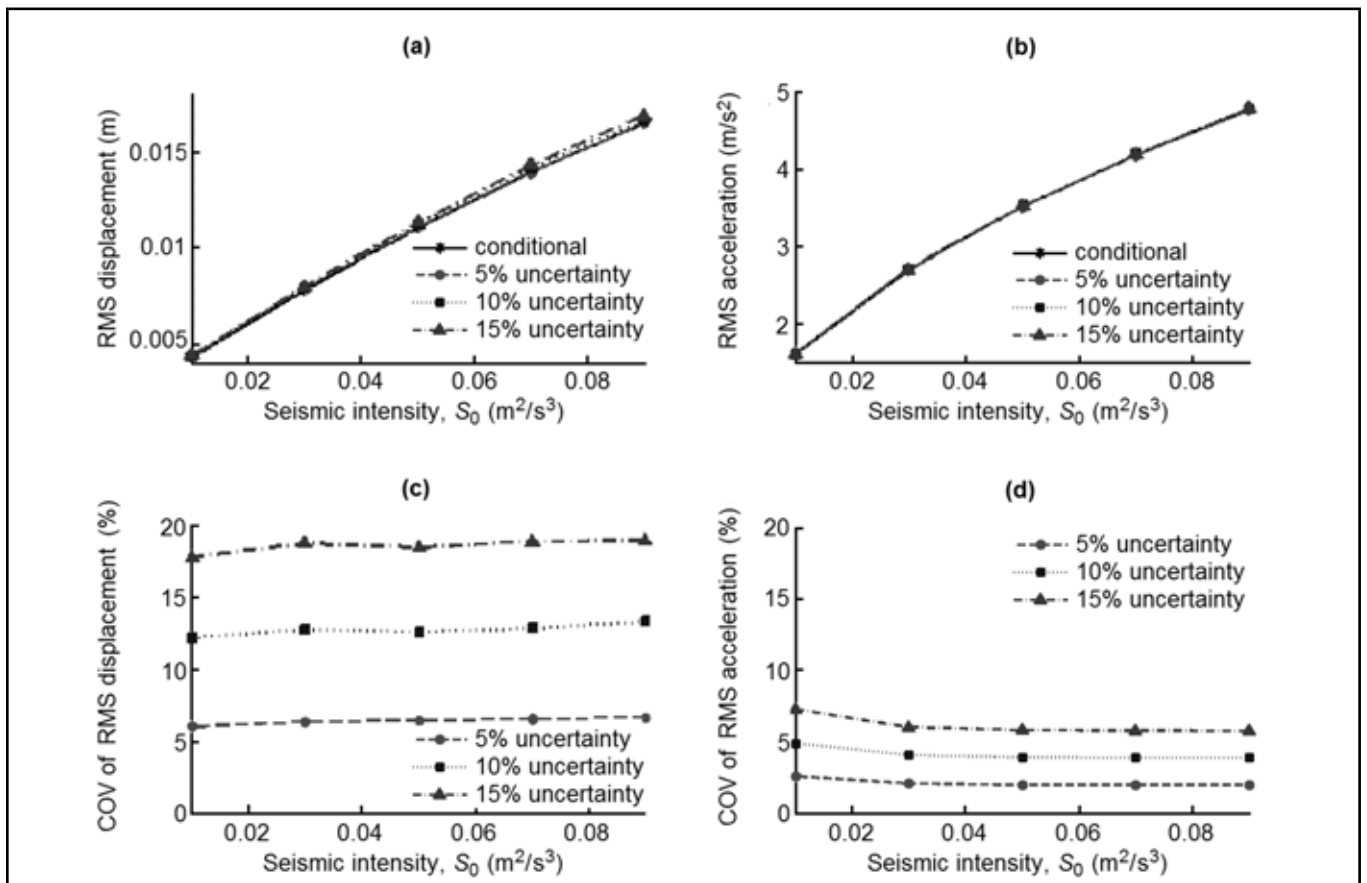


Figure 8. Conditional and unconditional RMS top-floor (a) displacement and (b) acceleration, and coefficient of variation of top-floor (c) displacement and (d) acceleration with varied seismic intensity and different degrees of uncertainty.

unconditional response), this is expressed as

$$\frac{(\partial f / \partial x_i) \sigma_{x_i}}{\sqrt{\sum_{i=1}^{nv} (\partial f / \partial x_i)^2 \sigma_{x_i}^2}}; \quad (43)$$

and a similar expression is used for contribution of the second-order terms (governing the unconditional response). Figure 2 clearly indicates that the superstructure stiffness is the most important parameter as far as the top-floor displacement responses are concerned, whereas the top-floor acceleration response is primarily affected by the uncertainty in the ground frequency (ω_g) and intensity of the earthquake (S_0). The second-order sensitivity of both the responses with respect to the seismic intensity is negative. It is noteworthy that the first-order sensitivity of top-floor acceleration with respect to the ground frequency is much higher than the ground damping, whereas for the second-order sensitivity, the trend is the opposite. These observations conform to the fact that the displacement response is governed by the system stiffness, whereas the floor acceleration, being a measure of the amount of seismic force transmitted to the structure, is dictated by the seismic ground motion.

Though the uncertainty in the excitation process dominates the performance of the BI system, the uncertainties in the system parameters, in particular, the superstructure stiffness, damping, and yield strength of the LRB have noticeable influence and cannot be neglected. With this nature of the parametric randomness and the relative importance, the conditional and unconditional response of the system and the associated coefficient of variation are studied subsequently.

The conditional and the unconditional responses of the BI system are presented for varied superstructure flexibilities in Figs. 3(a) and 3(b). The superstructure flexibilities are expressed in terms of the time period of the superstructure. The parametric uncertainty increases the RMS displacement and acceleration, shown in Figs. 3(a) and 3(b). The increase in the RMS acceleration is, however, lesser than the RMS displacement. This difference might be the result of the absolute acceleration including ground acceleration, which is irrespective of the parametric uncertainty. The coefficient of variation for the respective unconditional responses are shown in Figs. 3(c) and 3(d). It should be noted that the coefficient of variation increases with increasing randomness for the range of considered superstructure flexibilities. The coefficient of variation for the RMS displacement is almost three orders of magnitude higher compared to that of RMS acceleration.

The variations of the conditional and unconditional responses of the BI system are shown with respect to the varied damping of the superstructure in Figs. 4(a) and 4(b). It is important to note that the deterministic system underestimates the superstructure RMS displacement and acceleration. The difference increases with an increasing level of uncertainty. Observing the parametric variations of responses with the superstructure damping, it can be inferred that the RMS acceleration response is more sensitive to the variation of damping. However, the change of coefficient of variation of the acceleration with an increasing level of randomness in system parameters

is less than that of the displacement, implying less sensitivity of the acceleration to uncertainty.

The conditional and unconditional responses are presented with varied time period of isolation in Figs. 5(a)–(d). These figures also show that the unconditional responses are greater than the respective conditional responses. The coefficient of variation of the acceleration is seen to be a few orders of magnitude less than that of displacement.

The parametric variation of the responses and their coefficients of variation are shown with respect to isolator damping in Figs. 6(a)–(d). As described earlier, for different level of randomness in the system parameters, the unconditional responses and associated coefficients of variation are affected differently. The displacement is more affected by the uncertainty compared to the acceleration, as shown in terms of the unconditional responses and associated coefficients of variation. The effect of uncertainty uniformly affects the disparities among the conditional and unconditional responses. The coefficient of variation of the unconditional responses does not change significantly with the variations of isolator damping, confirmed by Figs. 6(c) and (d).

The responses of the BI system are further studied with regard to varied yield strength of the isolator in Figs. 7(a)–(d). As described earlier, the conditional responses are lower compared to the respective unconditional responses. It is noteworthy that the isolator yield strength presents the optimal value for which acceleration/displacement is the minimum. Obviously, the optimal yield strength values for minimum displacement and acceleration are not necessarily identical. It should be noted that the associated coefficient of variation of the displacement is almost irrespective of the parametric variations of the yield strength (Fig. 7(c)), whereas the coefficient of variation for the acceleration shows a definite trend with respect to varying isolator yield strength (Fig. 7(d)). The coefficient of variation of the unconditional acceleration response decreases first and then starts increasing with increasing yield strength of the isolator, which is unlikely for the variations of the responses presented so far. Comparing Figs. 7(b) and 7(d), it is observed that the optimal values of the yield strength corresponding to the minimum RMS acceleration might not ensure that the respective coefficient of variation is also at the minimum. Thus, designers must deal with two conflicting objective functions, i.e., the minimization of the unconditional RMS response and its variance. This problem can formally be addressed by formulating it as bi-objective optimization in order to minimize the unconditional RMS response as well as its dispersion (coefficient of variation) simultaneously—referred to as robust design optimization (RDO). The optimum LRB parameters in RDO are achieved from a set of Pareto optimal solutions by ensuring the desired level of robustness in the design. The issue is emphasized, though not studied, in this paper.

It is noteworthy that the trend in Figs. 7(a) and (b) might not necessarily be the same as that observed in an isolated structure subject to a particular ground motion time history, even though for large numbers of ground motion time histories, the average trend should match that of the stochastic response in an ensemble.

Table 2. Disparities among the conditional and unconditional responses for ranges of parameter variations.

System parameters	Lower and upper value	Uncertainty (cov, %)	Discrepancy among cond. and uncond. top-floor displacement (%)		Discrepancy among cond. and uncond. top-floor acceleration (%)	
			Lower	Upper	Lower	Upper
Structural period	0.1 1.0	5	0.27	0.41	0.020	0.019
		10	1.10	1.43	0.08	0.07
		15	2.48	3.08	0.19	0.17
Structural damping	0.01 0.09	5	0.00	0.00	0.03	0.03
		10	0.90	0.90	0.90	0.11
		15	2.70	1.81	0.27	0.25
Isolator period	1.5 2.5	5	0.00	0.00	0.044	0.02
		10	1.40	1.25	0.17	0.08
		15	2.80	2.50	0.39	0.18
Isolator yield strength	0.01 0.20	5	0.0	0.0	0.015	0.017
		10	0.60	0.78	0.055	0.066
		15	1.80	2.34	0.12	0.15
Isolator damping	0.025 0.10	5	2.5	0.0	0.15	0.02
		10	3.33	1.06	0.25	0.08
		15	5.00	2.13	0.42	0.20
Seismic intensity	0.01 0.09	5	0.00	0.00	0.018	0.030
		10	0.00	0.60	0.025	0.12
		15	2.32	2.42	0.20	0.27

ble sense. This is due to the wide disparities which exist in the power spectrum of a particular ground motion time history and the idealized Kanai-Tajimi spectra, employed in this stochastic analysis.

The behaviour is further studied for earthquake scenario of different intensities, shown in Figs. 8(a)–(d). With increasing seismic intensity, the RMS response increases for obvious reasons. The coefficient of variation of the unconditional displacement response is almost three times higher than the corresponding acceleration response. However, the coefficient of variation for both is insensitive to the variations in the seismic intensities (Figs. 8(c) and (d)).

The discrepancies among the conditional and unconditional responses and the associated coefficients of variation have been presented, along with the parametric variations of responses with the structural and isolator parameters. Though the variations of the response coefficients of variation are quite obvious from the plots, the response values and associated disparities (in %) are presented in Table 2 to provide more precise estimates of the disparities. The particular cases presented here correspond to the minimum and maximum value of the respective parameters considered in the parametric study. Table 2 shows that the differences among the conditional and unconditional RMS displacement responses could be as high as 5%, whereas for acceleration response, the difference is around 0.5%. The associated coefficients of variation are around 20% for displacement and 8% for acceleration (Figs. 7(c), 7(d), 8(c), and 8(d)). These differences (particularly for displacement) are substantial, considering the fact that the peak value of the responses could be as high as three to four times (peak factor) of the respective RMS values.^{31,32} Thus, system parameter uncertainty is a critical issue in response evaluation and design of BI systems in order to ensure the desired level of seismic safety.³⁵

4. CONCLUSIONS

The effects of system parameter uncertainty on the performance of BI systems subject to a stochastic earthquake load has been examined. This study incorporates the effects of system parameter uncertainty in the response evaluation through perturbation-based analysis of the dynamic equations of motion. The degree of parameter uncertainty is assumed to be small so that the linear first-order perturbation analysis is valid. The responses are found to be in parity with the results obtained from the usual random vibration analysis assuming deterministic system parameters. However, a definite change in the responses occurs when the effects of system parameter uncertainty are included. In general, the efficiency of a BI system tends to decrease as the level of uncertainty increases, though efficiency is not completely eliminated. Therefore, even though the randomness in the seismic events dominates, the random variations of the system parameters play a significant role. The randomness in the structural stiffness governs the unconditional RMS displacements and associated coefficient of variation, whereas the randomness in the characteristic ground frequency and intensity governs the unconditional RMS acceleration response and coefficient of variation. The unconditional RMS responses are always greater than (floor displacement, acceleration) the conditional responses. The discrepancies among the conditional and unconditional RMS responses are observed to be 5% for the superstructure displacement, with the maximum possible value of isolator damping. The respective coefficient of variation of the unconditional responses for the top-floor superstructure displacement and acceleration are around 19% and 6%, respectively. With the observed discrepancies amongst the conditional and unconditional responses and coefficient of variation, the peak value of the respective responses could be significantly different from the conditional one. Thus, disregarding the system uncertainty might lead to an unsafe design. From the parametric variations of the responses with respect to the isolator yield strength, it is observed that the optimal yield strength exists to ensure the best performance, which might be affected by the uncertainty. The optimum value of the yield strength might be based on two mutually conflicting objective function containing the minimization of both the unconditional responses as well as the associated standard deviations, thus making the problem ideal for reliability-based robust optimization. However, this aspect requires further study.

REFERENCES

- Spencer, B. F. and Nagarajaiah S. State of the art of structural control, *Journal of the Art of Structural Control*, **129** (7), 845–856, (2003).
- Buckle, I. and Mayes, R. Seismic isolation: History, application, and performance—A world view, *Earthquake Spectra*, **6** (2), 161–201, (1990).
- Symans, M. D. and Constantinou, M. C. Semi-active control systems for seismic protection of structures: A state-

- of-the-art review, *Engineering Structures*, **21**, 469–487, (1999).
- 4 Jangid, R. S. and Datta, T. K. Seismic behaviour of base-isolated buildings: A state-of-the-art review, *Structures and Buildings*, **110** (2), 186–202, (1995).
 - 5 Ribakov, Y. Selective controlled base isolation system with magnetorheological dampers, *Earthquake Engineering and Structural Dynamics*, **31** (6), 1301–1324, (2002).
 - 6 Taflanidis, A. A. and Jia, G. A simulation-based framework for risk assessment and probabilistic sensitivity analysis of base-isolated structures, *Earthquake Engineering and Structural Dynamics*, **40** (14), 1629–1651, (2011).
 - 7 Jangid, R. S. Stochastic response of building frames isolated by lead-rubber bearings, *Structural Control Health Monitoring*, **17** (1), 1–22, (2010).
 - 8 Jangid, R. S. Optimum lead-rubber isolation bearings for near-fault motions, *Engineering Structures*, **29** (10), 2503–2513, (2007).
 - 9 Baratta, A. and Corbi, L. Optimal design of base-isolators in multi-storey buildings, *Computers and Structures*, **82** (23–26), 2199–2209, (2004).
 - 10 Yen, Y. J., Huang, P. C., and Wan S. Modifications on base isolation design ranges through entropy-based classification, *Expert Systems with Applications*, **36** (3:1), 4915–4922, (2009).
 - 11 Li, H. N. and Ni, X. L. Optimization of non-uniformly distributed multiple tuned mass damper, *Journal of Sound and Vibration*, **308** (1–2), 80–97, (2007).
 - 12 Marano, C., Trentadue, F., and Greco, R. Stochastic optimum design criteria for linear damper devices for seismic protection of buildings, *Structural and Multidisciplinary Optimization*, **33** (6), 441–455, (2007).
 - 13 Taflanidis, A. A., Beck, J. L., and Angelides, D. C. Robust reliability-based design of liquid column mass dampers under earthquake excitation using an analytical reliability approximation, *Engineering Structure*, **29** (12), 3525–3537, (2007).
 - 14 Chakraborty, S. and Roy, B. K. Reliability based optimum design of Tuned Mass Damper in seismic vibration control of structures with bounded uncertain parameters, *Probabilistic Engineering Mechanics*, **26** (2), 215–221, (2011).
 - 15 Debbarma, R., Chakraborty, S., and Ghosh, S. Optimum design of tuned liquid column dampers under stochastic earthquake load considering uncertain bounded system parameters, *International Journal of Mechanical Sciences*, **52** (10), 1385–1393, (2010).
 - 16 Debbarma, R., Chakraborty, S., and Ghosh, S. Unconditional reliability based design of tuned liquid column dampers under stochastic earthquake load considering system parameter uncertainties, *Journal of Earthquake Engineering*, **14** (7), 970–988, (2010).
 - 17 Marano, G. C., Sgobba, S., Greco, R., and Mezzina, M. Robust optimum design of tuned mass dampers devices in random vibrations mitigation, *Journal of Sound Vibration*, **313** (3–5), 472–492, (2008).
 - 18 Marano, G. C., Greco, R., and Sgobba, S. A. A comparison between different robust optimum design approaches: Application to tuned mass dampers, *Probabilistic Engineering Mechanics*, **25** (1), 108–118, (2010).
 - 19 Benfratello, S., Caddemi, S. and Muscolino G. Gaussian and non-Gaussian stochastic sensitivity analysis of discrete structural system, *Computers and Structures*, **78** (1–3), 425–434, (2000).
 - 20 Kawano, K., Arakawa, K., Thwe, M., and Venkastaramana, K. Seismic response evaluations of base-isolated structures with uncertainties, structural stability and dynamics, *Proc. International Conference on Structural Stability and Dynamics*, Singapore, **16–18**, 889–894, (2002).
 - 21 Scruggs, J. T., Taflanidis, A. A., and Beck, J. L. Reliability-based control optimization for active base isolation systems, *Structural Control and Health Monitoring*, **13** (2–3), 705–723, (2006).
 - 22 Zhou, J., Wen, C., and Cai, W. Adaptive control of a base isolated system for protection of building structures, *Journal of Vibration and Acoustics*, **128** (2), 261–268, (2006).
 - 23 Zhou, J. and Wen, C. Control of a hysteretic structural system in base isolation scheme, adaptive backstepping control of uncertain systems, *Lecture Notes in Control and Information Sciences*, **372**, 199–213, (2008).
 - 24 Li, J. and Chen, J. B. First passage of uncertain single degree-of-freedom nonlinear oscillations, *International Journal for Numerical Methods in Engineering*, **65** (6), 882–903, (2006).
 - 25 Ismail, M., Ikhouane, F., and Rodellar, J. The hysteresis Bouc-Wen model, a survey, *Archive of Computational Methods in Engineering*, **16** (2), 161–188, (2009).
 - 26 Wen, Y. K. Method of random vibration of hysteretic systems, *Journal of Engineering Mechanics*, **102** (2), 249–263, (1976).
 - 27 Atalik, T. S. and Utku, S. Stochastic linearization of multidegree of freedom nonlinear systems, *Earthquake Engineering and Structural Dynamics*, **4** (4), 411–420, (1976).
 - 28 Roberts, J. B. and Spanos, P. D. *Random Vibrations and Statistical Linearization*, Wiley, New York, (2003).
 - 29 Kanai, K. Semi-empirical formula for the seismic characteristics of the ground, *Bulletin of Earthquake Research Institute*, **35**, 309–325, (1957).
 - 30 Tajimi, H. A statistical method of determining the maximum response of a building structure during an earthquake, *Proc. World Conference on Earthquake Engineering*, **11**, 781–798, (1960).

$$\begin{bmatrix}
 \begin{matrix} 0 & \dots & 0 \\ \vdots & n \times n & \vdots \\ 0 & \dots & 0 \\ 0 & \dots & 0 \\ 0 & 3 \times n & 0 \\ 0 & \dots & 0 \end{matrix} & 0 & 0 & 0 & \begin{matrix} 1 & \dots & 0 \\ \vdots & n \times n & \vdots \\ 0 & \dots & 1 \\ 0 & \dots & 0 \end{matrix} & 0 & 0 \\
 \begin{matrix} M^{-1}K_{11} - \frac{k_1}{m_b} & \dots & M^{-1}K_{1n} \\ \vdots & M^{-1}K_{ij} - \delta_{ij} \frac{k_1}{m_b} & \vdots \\ M^{-1}K_{n1} - \frac{k_1}{m_b} & \dots & M^{-1}K_{nn} \end{matrix} & \begin{matrix} \alpha \frac{k_b}{m_b} & \frac{(1-\alpha)F_Y}{m_b} & 0 \\ \vdots & \vdots & \vdots \\ \alpha \frac{k_b}{m_b} & \frac{(1-\alpha)F_Y}{m_b} & 0 \end{matrix} & \begin{matrix} M^{-1}C_{11} - \frac{c_1}{m_b} & \dots & M^{-1}C_{1n} \\ \vdots & M^{-1}C_{ij} - \delta_{ij} \frac{c_1}{m_b} & \vdots \\ M^{-1}C_{n1} - \frac{c_1}{m_b} & \dots & M^{-1}C_{nn} \end{matrix} & \begin{matrix} \frac{c_b}{m_b} & 0 \\ \vdots & \vdots \\ \frac{c_b}{m_b} & 0 \end{matrix} & 0 & 0 \\
 \begin{matrix} \frac{k_1}{m_b} & \dots & 0 \\ 0 & \dots & 0 \end{matrix} & \begin{matrix} -\alpha \frac{k_b}{m_b} & -\frac{(1-\alpha)F_Y}{m_b} & \omega_g^2 \\ 0 & 0 & -\omega_g^2 \end{matrix} & \begin{matrix} \frac{c_1}{m_b} & \dots & 0 \\ \vdots & \vdots & \vdots \\ 0 & \dots & 0 \end{matrix} & \begin{matrix} -\frac{c_b}{m_b} & 2\xi_g \omega_g \\ \vdots & \vdots \\ -\frac{c_b}{m_b} & -2\xi_g \omega_g \end{matrix} & 0 & 0
 \end{bmatrix} \quad (A.1)$$

- ³¹ Sun, J. Q. *Stochastic Dynamics and Control*, Elsevier, Amsterdam, (2006).
- ³² Lutes, D. L. and Sarkani, S. *Random Vibrations, Analysis of Structural and Mechanical Systems*, Elsevier, Burlington, Massachusetts, (2004).
- ³³ Jensen, H. A. Design and sensitivity analysis of dynamical systems subjected to stochastic loading, *Computers and Structures*, **83** (14), 1062–1075, (2005).
- ³⁴ Jensen, H. A. Structural optimization of non-linear systems under stochastic excitation, *Probabilistic Engineering Mechanics*, **21** (4), 397–409, (2006).
- ³⁵ Chaudhuri, A. and Chakraborty, S. Sensitivity evaluation in seismic reliability analysis of structures, *Computer Methods in Applied Mechanics and Engineering*, **193** (1–2), 59–68, (2004).

$$\mathbf{K} = \begin{bmatrix} k_1 + k_2 & -k_2 & \dots & \dots & \dots \\ -k_2 & k_2 + k_3 & \dots & \dots & \dots \\ \dots & -k_i & k_i + k_{i+1} & -k_{i+1} & \dots \\ \dots & \dots & \dots & k_n + k_{n-1} & -k_n \\ \dots & \dots & \dots & -k_n & k_n \end{bmatrix} \quad (A.2)$$

$$\mathbf{C} = \begin{bmatrix} c_1 + c_2 & -c_2 & \dots & \dots & \dots \\ -c_2 & c_2 + c_3 & \dots & \dots & \dots \\ \dots & -c_i & c_i + c_{i+1} & -c_{i+1} & \dots \\ \dots & \dots & \dots & c_n + c_{n-1} & -c_n \\ \dots & \dots & \dots & -c_n & c_n \end{bmatrix} \quad (A.3)$$

in which k_i and c_i are the stiffness and damping of the i -th storey of the building. The damping for the i -th storey is expressed as

$$c_i = 2\xi\sqrt{k_i m_i}; \quad (A.4)$$

where ξ is the viscous damping ratio of the superstructure.

The matrix for the rock bed seismic motion, characterized by the white noise of intensity S_0 is expressed as

$$\mathbf{S}_{ww} = \begin{bmatrix} 0 & 0 & \dots & 0 & 0 \\ 0 & 0 & \dots & 0 & 0 \\ \vdots & \vdots & \ddots & \vdots & \vdots \\ 0 & 0 & \dots & 0 & 0 \\ 0 & 0 & \dots & 0 & 2\pi S_0 \end{bmatrix} \quad (A.5)$$

which is a square matrix of dimension $(2n + 5)$.

APPENDIX

The structure of the augmented system matrix (Eqs. (20) and (22)) \mathbf{A} for a n -storied shear building is given in Eq. A.1 All the parameters in the matrices have already been defined in the main text. The variable δ_{ij} is the Kronecker's delta defined as $\delta_{ij} = 1$ when $i = j$ and $\delta_{ij} = 0$ when $i \neq j$. The augmented stiffness ($\mathbf{M}^{-1}\mathbf{K}$) and damping ($\mathbf{M}^{-1}\mathbf{C}$) matrices are indicated in the respective block of dimension $n \times n$.

The mass matrix is diagonal containing the storey mass in each diagonal term. The stiffness and damping matrices take the following form:

Experimental Verification of Drill String Vibration Suppression Using an Adaptive Self-Tuning Controller

Fesmi Abdul Majeed and Hamad Karki

Mechanical Engineering Department, Petroleum Institute, Abu Dhabi, P.O. Box 2533, UAE

Mansour Karkoub

Mechanical Engineering Department, Texas A&M, Doha, P.O. Box 23874, Qatar

Youssef Lotfy Abdel Magid

Electrical Engineering Department, Petroleum Institute, Abu Dhabi, P.O. Box 2533, UAE

(Received 16 November 2011, revised 20 September 2012, accepted 14 November 2012)

Drill bit whirl is a common phenomenon in rotary drilling rigs. It causes severe drill collar damage and borehole enlargement, leading to an irrevocable decrease in drilling efficiency. The majority of the research in this field concentrates on designing new drill bits or placing shock absorbers near the bottom hole assembly to minimize the damage caused by drill bit whirling. However, practically, vibrations in rotary drilling are minimized by tuning the upper rotary table speed or varying the weight on drill bit. This work explores the design and implementation of an adaptive controller to minimize vibrations of drill bits, particularly bit whirl. The developed controller achieves the vibration mitigation by varying the upper rotary speed. Moreover, the developed control law takes into account the vibrational frequencies and critical operating speeds of the drill string, thus also being capable of avoiding resonant vibrations. Experimental results are provided to prove the vibration mitigation capability of the developed controller.

NOMENCLATURE

$A(z)$	Discrete process model denominator
$B(z)$	Discrete process model numerator
$C(z)$	Discrete noise model numerator
$D(z)$	Discrete noise model denominator
E	Compression constant
$e(k)$	Discrete process noise vector
f	Controller selected frequency of operation
f_n	Natural frequency
G	Shear constant
k	Discrete time instant
L	Length of the drill string
N	Critical speed of operation
n	Normal frequency of operation
$n(t)$	White noise
t	Continuous time instant
$u(k)$	Discrete process input
$u(t)$	Process Input
$y(k)$	Discrete Process output
$y(t)$	Process output

1. INTRODUCTION

Bit whirl is a common phenomenon arising due to high lateral vibrations in rotary drilling rigs. It causes reduction of drilling efficiency, drill pipe bending, and well borehole enlargement. Hence, lateral vibrations of the drill bit are the most destructive type of vibrations in rotary drilling.¹⁻³

Drill bit whirl can also occur when drill bits have an imbalance in the drill bit design during manufacturing or when there

is a slight bend in the drill collars due to high lateral vibrations.⁴ Both of these imperfections cause lateral vibrations to be predominant.⁵

Most of the commercially available drill bits have imbalances in the range of 2% to 10%, with 2% only for a very high commercially graded bit.⁶ To overcome this manufacturing imbalance and reduce drill bit whirl, many new drill bit models were designed.⁶⁻⁹ However, these designs cannot mitigate bit whirl completely due to manufacturing imbalances. Practical solutions to minimizing and stabilizing drill string vibrations using current monitoring technology include changing the upper rotary speed or varying the weight on bit.¹⁰ This study attempts to provide a practical solution to minimizing drill bit whirl using adaptive controllers.

Adaptive controllers are a very exciting new technology, and a few researchers have recently developed and tested adaptive controllers to mitigate drill string vibrations. Fubin et al. developed an adaptive proportional-integral-derivative (PID) control strategy of the drilling rotary system to eliminate the stick-slip oscillation of the bit.¹¹ The main objective of the adaptive PID controller is to improve system characteristics of the output-to-input and dynamic response. The results of the controller have been proven only in simulations. Jijón et al.¹² designed an adaptive observer and analysed the Drilling-Oscillation Killer (D-OSKIL) control law proposed by C. Canudas-de Wit et al.¹³ The D-OSKIL controller uses a vertical force (weight on the bit) as an additional variable to eliminate the stick-slip effect. Jijón et al.¹² tried to improve the control law with an additional adaptive observer so that the unknown states of the system could be estimated. Smoother

estimates were obtained; however, no different control law has been proposed. Li, Qizhi, and Nurzat developed a time-varying sliding mode adaptive controller for the mathematical model of a rotary drilling system.¹⁴ The controller used is PID, and the simulation results proved a good time response for the bit. However, the vibrational frequencies of the upper and lower rotary and their angular velocity magnitudes were not clear. The simulations showed a good tracking performance, but in our view, the drill bit is an underactuated part of the rotary drilling system,¹⁵ and hence its accurate movements cannot be completely predicted or verified through simulations.

The literature review revealed a gap for a practically applicable control solution to drill bit whirl. This study attempts to design an adaptive control law for drill bit whirl. The controller we developed and its efficiency were also tested experimentally on a laboratory prototype of rotary drilling.

2. THEORETICAL METHOD AND FINDINGS

During our experiments, the vibration associated with the drill string increased substantially when operated near or at some critical speeds. Dareing¹⁶ states that various vibrational modes (lateral, torsional, and axial) have separate excitation frequencies associated with each of them, and hence there is a need for identifying these critical speeds in order to better avoid these speeds during operation. Dareing also developed a formula which proves a direct proportional relation between the critical speeds and the natural frequencies of the drill collar (tubular steel sections—the component of the drill string near to the drill bit). However, the drill collar length changes during drilling operation as the drill borehole becomes deeper. The natural frequencies of the drill collar associated with each of the vibrational modes also change.^{16–18} Even though most of the designed controllers fail to include this significant theory, Bailey et al. developed a bottom hole assembly modelling tool that avoids the critical modes causing resonance for a particular operating range.¹⁹

Drill bit imbalance together with borehole friction increases the lateral vibrations in rotary drilling. Experimental tests were conducted on the laboratory prototype of a rotary drilling rig to analyse the system behaviour. Initially, tests were conducted with an imbalance of 5.2% added on the drill bit, based on research findings from Jansen⁴ and Warren, Brett, and Sinor⁶ to account for drill pipe eccentricity. The experimental tests conducted to detect the natural frequencies of the system are discussed below.

The laboratory set up with the imbalanced bit was operated at three speeds, spanning from low to high, selected from the normal operational speed range (30–100 RPM) used in rotary drilling. The angular velocity of the drill bit was logged during operation using rotary encoders and programmed using a developed MATLAB program to plot the fast Fourier transformation (FFT) response. The FFT frequency response of the drill bit angular velocity was analysed to detect the system natural frequencies (Fig. 1). It was noticed that the system has more than one natural frequency, and the resonant frequencies of the system do not change when varying the operational speed.

In order to analyse the borehole effect on the drill bit whirl dynamics, a layer of natural rubber sponge was added as a lining to the casing surrounding the drill bit to represent the frictional effect of mud and fluid on the drill bit within the bore-

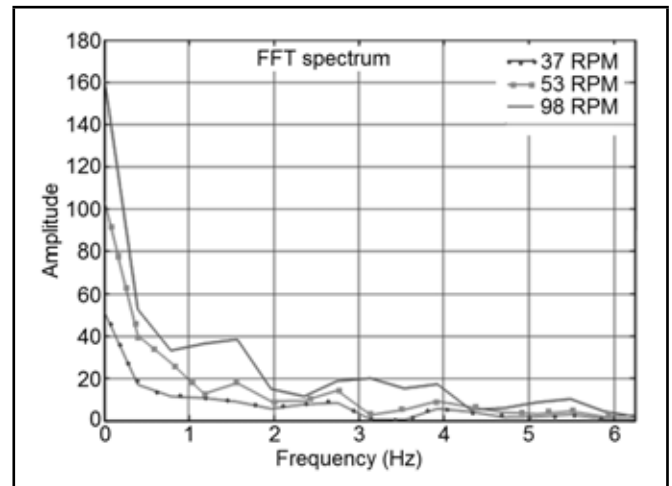


Figure 1. FFT response of imbalanced drill bit whirling with no borehole effect.

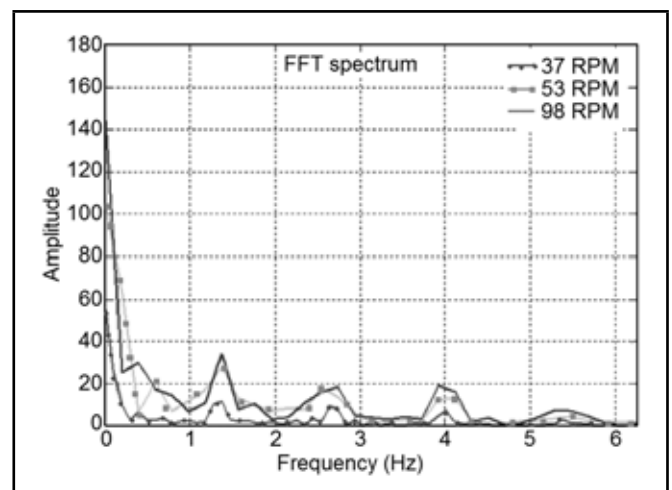


Figure 2. FFT response of drill bit whirling with borehole friction effect.

hole. The system was again run on the previous operational speeds. The FFT frequency response of the drill bit angular velocity was again plotted using the developed MATLAB program. More prominent vibrations were now exhibited by the system. The obtained FFT plot is exhibited in Fig. 2.

Comparing the FFT plot in Fig. 2 with Fig. 1, it should be noted that the resonant modes are excited and more prominent when the external borehole effect is present. Experimentally, the lateral and torsional vibrations exhibited by the drilling system were noticeably more severe under borehole friction.

Using the data in the frequency response plots, the critical speeds for the system for the various excitational modes were found. The speeds were obtained to closely match the calculated speeds using the formula developed (Eq. (10)) by Dareing.¹⁶ If the system is operated at operational speeds near or at the critical resonant frequencies in the plots above, high vibration should be exhibited. The recordings of the experiments conducted to observe the resonant vibrations near the critical speeds are plotted in Figs. 3(a)–(d).

In Figs. 3(a)–(d), the residual signal is the difference between the angular velocities of the upper and lower flywheels. It should be noted that the limit cycling is present and noticeable at 53 and 83 RPM. However, they are not visible in the plots for 23 and 69 RPM, though the lower flywheel was visibly whirling due to the friction imposed by the rubber sponge

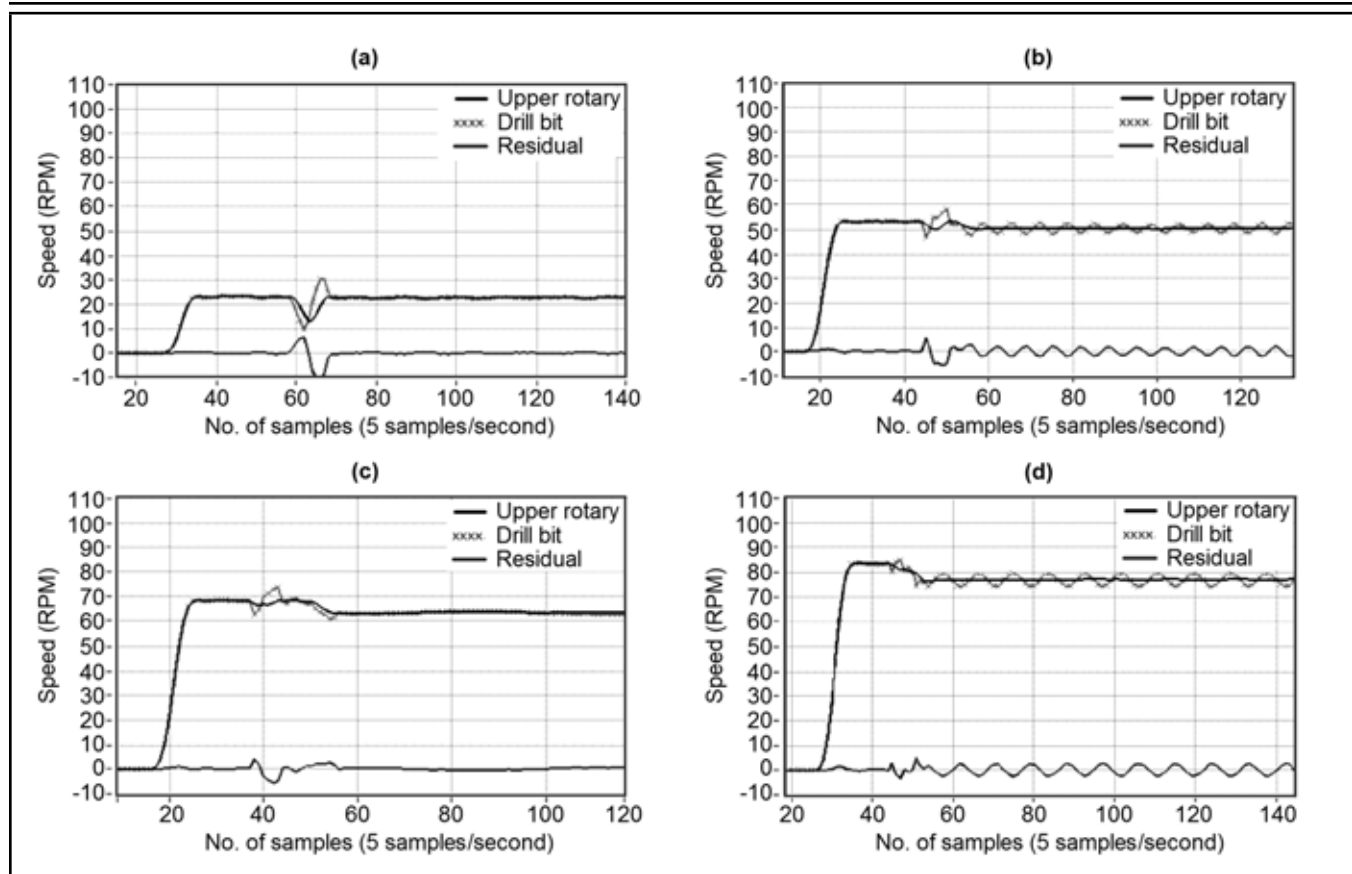


Figure 3. Experimental response at (a) 23 RPM, (b) 53 RPM, (c) 69 RPM, and (d) 83 RPM.

lining on the casing. The tests confirmed the calculated values of the critical operational speeds. The lateral vibrations causing the whirl effect is reflected in the bit angular velocity at critical speeds of operation, and they disappeared at other operational speeds. The tests also proved the significance of developing a control law which could effectively avoid operating the drilling system near its critical operational speeds.

3. CONTROL METHODOLOGY AND EXPERIMENTAL RESULTS

The control strategy which would minimize the vibrations affecting the drill string and stabilize it must ensure that the drill string is operated at a velocity away from its critical speeds of rotation. The drill string natural frequencies and critical speeds vary during the drilling process as the well deepens and the drill string length changes. This fact poses a challenge to developing a method to identify the critical speeds of the system during drilling operation. New tools which have been developed, such as the BlackBox downhole dynamics data recorder, can log dynamic data, and researchers have identified methods for online detection of natural frequencies for complex nonlinear systems.²⁰⁻²² The controller should adapt its control output to effectively stabilize the system based on the identified natural frequencies and critical speeds. The complete control system has four objectives: (1) to detect the vibration of the system above an acceptable threshold value, (2) to force the system to operate at a stable operating speed away from its critical speeds, (3) to pull or free the axially displaced drill bit from the fluid/mud forces to a point near its centre of rotation, and (4) to resume normal operating speeds as soon as

the vibration decreases below the threshold.

The point of the control law is that the rotary drilling system is a stable system affected by external disturbances which make the system unstable. Thus, the control law effectively returns the system to its initial stable dynamics by helping the system to free itself from the destabilizing forces and forcing the system to operate in its stable region.

3.1. Adaptive Control

According to its definition, an adaptive control changes or adapts the design of the control algorithm to accommodate changes in the plant or its environment. There are two major types of adaptive control: self-tuning and model reference. This research uses self-tuning adaptive control. Model reference control requires a reference model. Because the drill string length changes as the rotary drilling progresses, the model for the system would also change; this fact implies the need for using an additional system to identify the model for the system continuously and developing the controller based on its performance. This would unnecessarily complicate the situation because, as described earlier, it is important to detect online the natural frequencies of the system to generate an efficient control law. Model reference control applied here would then necessitate a two-fold online identification system. Adaptive control applied to complex systems itself is quite complex and requires good data synchronization. Based on the fact that it is best to simplify where possible without losing quality results, this research aimed to develop a self-tuning adaptive control law which can be implemented and analysed experimentally.

Self-tuning control of a plant has three major parts: (1) a feedback control law, (2) a control design algorithm, and (3) an online identifier. The feedback control law should be designed to give control performance based on the data from the online identifier. The online identifier should provide good estimates of the data required to form the control law. The control design algorithm uses the estimate of the online identifier to update the feedback control law.

For the current research system, these three parts can be defined as follows. The adaptive control signal serves as the feedback control law; the synchronization of the flow of data using vibration detector, the command signal selector, and signal generation serve as the control design algorithm; and the online natural frequency identifier serves as the online identifier.

The adaptive control law developed for the research is a combined application of minimum variance and gain scheduling algorithms.

3.2. Minimum Variance Control

Consider a discrete process model:

$$y(t) = \frac{z^{-k}B(z)}{A(z)}u(t) + \frac{C(z)}{A(z)}n(t); \quad (1)$$

where $y(t)$ is the output, $u(t)$ the input, $n(t)$ is white noise at any sampled instant t , and k is the process delay. Assume $k > 0$ and

$$E[n(t)n(s)] = \begin{cases} 0, & s \neq t \\ \sigma^2, & s = t \end{cases} \quad (2)$$

Then, the control law for minimal output variance is obtained as

$$u(t) = \frac{-G(z)}{B(z)F(z)}y(t); \quad (3)$$

by solving for

$$C(z) = A(z)F(z) + z^{-k}G(z). \quad (4)$$

The rotary drilling system is an underactuated system, with the drill bit being the underactuated part.¹⁵ The drill bit is also the part experiencing vibrations and the source of phenomena such as bit whirl, stick slip, etc. The underactuation of the drill bit poses a serious problem to the results, which could be obtained practically by the application of any control law. This is because the control objective is to minimize the vibrations of the underactuated part, meaning it cannot be directly controlled, and the objective made complicated by the fact that the underactuated part is affected by unpredictable and uncontrollable external disturbances (i.e., well borehole friction, hard rocks, etc). However, it is possible in simulations and has been widely demonstrated in numerous studies.^{11,14,23}

In order to practically achieve the control objectives, a new control mechanism based on gain scheduling must be applied. Previous research by Dareing¹⁶ and Cobern^{17,18} suggests the importance of avoiding the critical speeds during rotary drilling operation as the more predictable method of minimizing the vibrations at drill bit. Dareing¹⁶ developed equations relating the critical speeds of resonance to the natural frequencies of the rotary drilling system:

$$N = 60f_n; \quad (5)$$

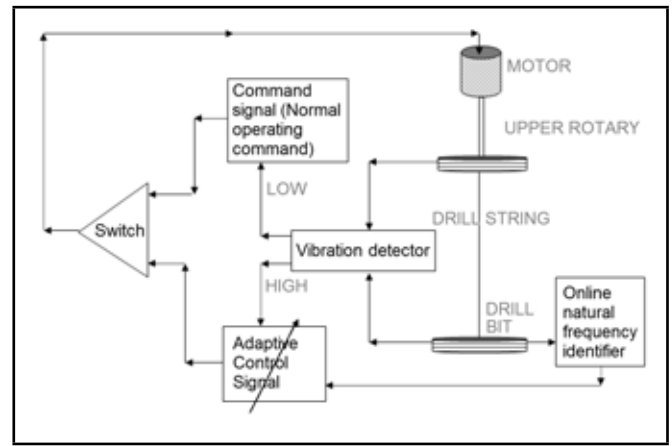


Figure 4. Schematic of adaptive controller implementation.

for a natural frequency f_n of the drilling system, the critical speed of operation of the drilling process to cause excitation is N .

However, the natural frequency is inversely related to the length of the drill string,¹⁶ and hence, the natural frequencies corresponding to different modes of vibrations will change continuously during drilling as the well deepens.

The natural frequency of the fundamental drill collar longitudinal mode is

$$f_{na} = \frac{1}{4L} \sqrt{\frac{E}{\rho}}; \quad (6)$$

the natural frequency of the fundamental drill collar torsional mode is

$$f_{n\theta} = \frac{1}{4L} \sqrt{\frac{G}{\rho}}; \quad (7)$$

where E and G are the compression and shear constants of drill string material and L is the length of the drill string.

The above equations were used for developing the control law which selects the appropriate speed of operation for the drilling system based on gain scheduling the natural frequencies of the process obtained by the online identification procedure, as detailed in Appendix A. The literature review resulted in the conclusion that the best possible method to minimize vibrations in drill strings is to develop a controller which adapts itself according to the natural frequencies of the system.

The applied control law is

$$u(t) = 60f \sin 2\pi nt; \quad (8)$$

where f is the low frequency of the drilling process, which is also not near any of the natural frequencies of the system, and n is the original frequency of drilling. The selection of f is the task of the control design algorithm. The critical speeds of the system were calculated using Eq. (5). The frequency f was selected so that the calculated resonant frequencies were avoided. The variable f is taken up by the adaptive controller, which produces the control signal as defined by the control law in Eq. (8). The motor connected to the upper rotary table is run by the control law developed in Eq. (8) until the vibration levels fall below the predetermined threshold values. Once the vibration levels are lowered, normal operation is resumed.

The control objectives were met by a complex synchronization achieved between the operating command signal, the de-

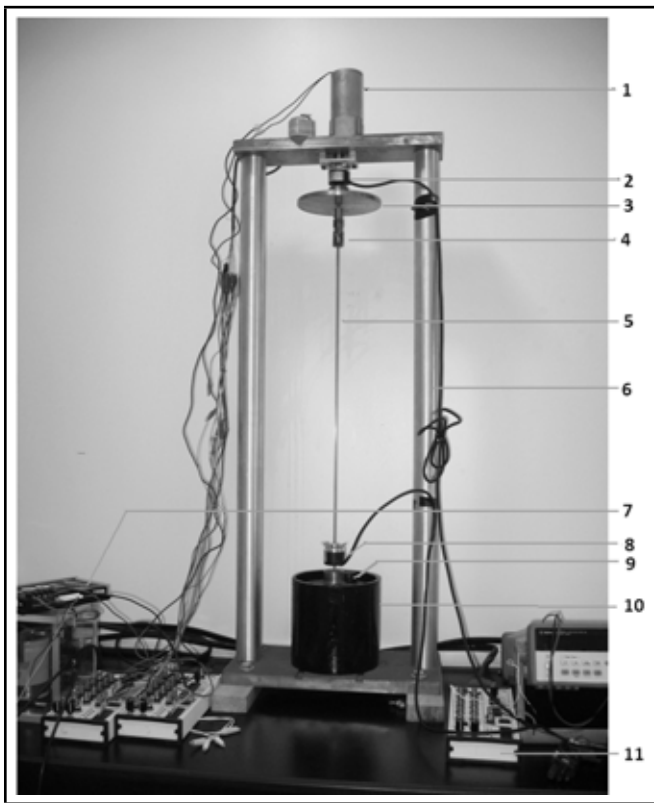


Figure 5. Laboratory arrangement.

veloped adaptive controller signal, and the rotary drilling hardware system. The flow of signals and their synchronization are depicted in Fig. 4. The angular velocities of the upper rotary and drill bit were used by the vibration detector and the online natural frequency identifier as data. The data was measured by rotary encoders and logged using LabVIEW programs. The vibration detector played an important part in deciding the level of vibrations and switched the motor excitation signal between the operating speed and control signal. The vibration detector was designed and developed using the LabVIEW Virtual Instrument. The threshold value is determined by the amount of vibration level the system could withstand and varies for every system depending on external factors such as the borehole effects, length of the drill string, etc. The amplitude of the control signal used to run the motor was selected by the adaptive controller using the system natural frequency data to operate the system at a speed away from the system’s critical frequency. The control signal was designed to be sinusoidal so that the system can force itself out of any friction or holding force at the drill bit end. The vibration detector was responsible for the switch back of the excitation signal to normal operating speed once the vibration level was reduced and maintained below threshold level for a specific time.

4. DISCUSSION

The drilling process was simulated in the laboratory by a simple experimental setup (Fig. 5 and Table 1) which captures the major features of a rotary drilling system. In a rotary drilling rig, an electric generator energizes the turntable, which provides the driving force for the entire drilling unit. The drill string is attached to the turntable and can vary in length from 8 to 10 km. The lower part of the drill string has drill collars

Table 1. Parts of the laboratory setup from Fig. (5).

Part number	Name of the part
1	DC Motor
2	Upper incremental Encoder
3	Upper rotary table
4	Universal Joint
5	Drill string
6	Metal frame
7	PWM Amplifier
8	Lower incremental encoder
9	Drill bit
10	Metal casing
11	NI DAQ BNC 2120

Table 2. Least squares based parameter estimates for selected Box-Jenkins model.

Terms	Parameter estimates	Terms	Parameter estimates
b_0	1.0345	f_3	-0.0442
b_1	0.512	c_1	-0.2482
b_2	0.3147	c_2	-0.7141
f_1	0.5825	d_1	-1.2031
f_2	0.3153	d_2	0.7316

and the drill bit. The laboratory setup was run by operating a motor which rotates a large rotor connected to the motor shaft. A drill string (1 m long made of carbon steel chosen due to its similarity to actual drill string material) was attached to the upper rotor by a universal joint. This joint provided two degrees of rotational freedom (DOF) about the x and y axes. The motor rotation provided the setup with one DOF of rotation about the z axes. Another flywheel was connected to the end of the drill string. It served to represent the drill bit and the mass of the drill collars. A casing surrounded the lower flywheel, representing the oil well borehole and its friction effects. Incremental encoders were used to measure the angular velocities of the upper rotor and the flywheel representing the drill bit. Two incremental encoders were used: one to measure the speed of the upper flywheel and a second one to measure the speed of the lower flywheel.

The practical experimentation was preceded by simulations using an identified mathematical model for the system using the BlackBox system identification method.²⁴ The identified Box-Jenkins model takes the following form:

$$y(k) = z^{-m} \frac{B(z^{-1})}{F(z^{-1})} u(k) + \frac{C(z^{-1})}{D(z^{-1})} e(k); \quad (9)$$

where $y(k)$, $u(k)$, and $e(k)$ are the output, input, and white noise at any instant k . And,

$$B(z) = 1 + b_1 z^{-1} + b_2 z^{-2} + \dots + b_{nb} z^{-nb}; \quad (10)$$

$$C(z) = 1 + c_1 z^{-1} + c_2 z^{-2} + \dots + c_{nc} z^{-nc}; \quad (11)$$

$$D(z) = 1 + d_1 z^{-1} + d_2 z^{-2} + \dots + d_{nd} z^{-nd}; \quad (12)$$

$$F(z) = 1 + f_1 z^{-1} + f_2 z^{-2} + \dots + f_{nf} z^{-nf}; \quad (13)$$

nb , nc , nd , and nf are the orders of the polynomials $B(z)$, $C(z)$, $D(z)$, and $F(z)$, respectively.

The Box-Jenkins model has orders $nb = 2$, $nf = 3$, noise model $nc = 2$ and $nd = 2$, and delay = 0. The parameter coefficients were estimated using the least squares principle and are listed in Table 2.

The adaptive control scheme in Fig. 4 was implemented on the laboratory setup for two operational speeds. In Fig. 6, the laboratory setup was operated at 54 RPM. The drill bit angular velocity was recorded and are plotted in Fig. 6. The drill

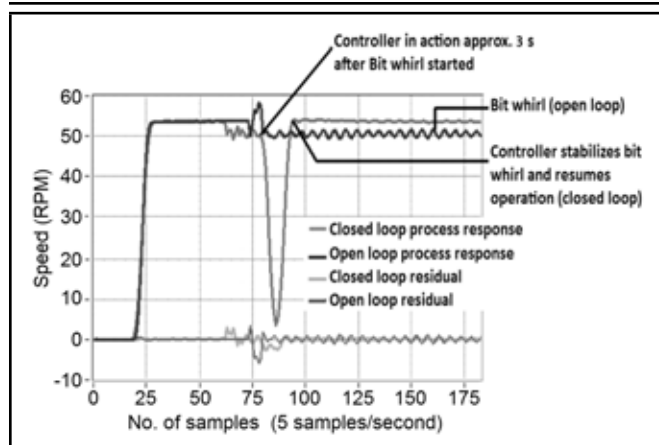


Figure 6. Experimental results of bit whirl and control in open and closed loop at operating speeds of 54 RPM.

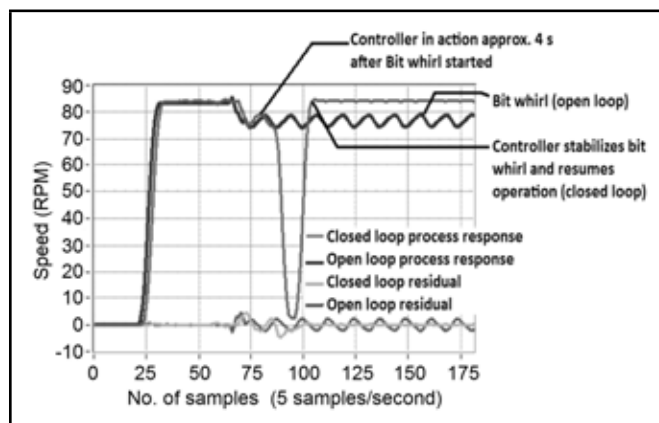


Figure 7. Experimental results of bit whirl and control in open and closed loop at operating speeds of 84 RPM.

bit rotates with no major vibrations until the drill bit starts whirling due to an external effect. When operated in an open loop, the drill bit continues whirling. However, when operated in a closed loop, the adaptive controller detects the increased vibration level and starts the control action when the vibration persists above the threshold value for a specified time, as depicted in Fig. 6. The controller forces the command signal to switch the upper rotary to the adaptive tuned control signal. The control signal is based on the control law given in Eq. (8). The control signal forces the drill bit to equilibrium by operating it such that it is taken away from its resonant modes of frequency. As soon as the vibration detector identified that the vibration levels of the drill bit have come down and remain within the threshold value, it forced the switch to resume normal operation. The residual signals in open and closed loop tests are also depicted in Fig. 6.

The differences in the angular velocity denote that the upper rotary and drill bit are operating at different magnitudes and phases during the vibrations. This indicates the presence of lateral and torsional vibrations at the same time. During closed loop operation, the controller minimized both the vibration effects and the residual signal was stable and near zero.

Figure 7 shows the plot of the open and closed loop operation of the system at 84 RPM. Results similar to this discussion were seen. A clear reduction in vibration and fast resuming of the normal operation were achieved by the controller.

5. CONCLUSIONS

The drill bit whirl phenomenon is very common in rotary drill rigs and has never been practically controlled by the application of an advanced control technology. The major vibration mitigation approaches have been new designs of drill bits and the introduction of dampers near the bottom hole assembly. An adaptive controller approach was developed in this study to stabilize and minimize drill bit vibrations. Well-defined relations between the vibrations and critical operating speeds were utilized to form the control law. The developed control law was implemented using LabVIEW programs, rotary encoders, and NI BNC2120 data acquisition devices. The controller effectiveness was practically tested on a laboratory scale setup of rotary drilling with well borehole friction effects, inducing bit whirling. The adaptive controller approach was proven successful and stabilization of the drill bit, and vibration mitigation of all three axes were achieved.

REFERENCES

- Schlumberger, Drillstring vibrations and vibration modeling, Retrieved from http://www.slb.com/~media/Files/drilling/brochures/drilling_opt/drillstring_vib_br.ashx, (2010).
- Donadieu, B. and Mathur, R. Technical Paper AADE, NTCE-05-03, Best practices for drilling with rotary steerable and real-time drilling optimization service, *National Technical Conference & Exhibition*, New Orleans, Louisiana, (2009).
- Zare, J., Hashemi, S. J., and Rashed, G. Finite element analysis of drillstring lateral vibration, *Scientific Research and Essays*, **6** (13), 2682–2694, (2011).
- Jansen, J. D. Non-linear rotor dynamics as applied to oilwell drillstring vibrations, *Journal of Sound and Vibration*, **147** (1), 115–135, (1991).
- Brett, J. F., Warren, T. M., and Behr, S. M. Bit whirl — A new theory of PDC bit failure, *SPE Drilling Engineering*, **5** (4), 275–280, (1990).
- Warren, T. M., Brett, J. F., and Sinor, L. A. Development of a whirl-resistant bit, *SPE Drilling Engineering*, **4**, 267–274, (1990).
- Pastusek, P. E., Cooley, C. H., Sinor, L. A., and Anderson, M. Directional and stability characteristics of anti-whirl bits with non-axisymmetric loading, *SPE Annual Technical Conference and Exhibition*, Washington, D. C., (1992).
- Chen, S. L., Blackwood, K., and Lamine, E. Field investigation of the effects of stick-slip, lateral, and whirl vibrations on roller-cone bit performance, *SPE Drilling & Completion*, **7** (1), 15–20, (2002).
- Johnson, S. A new method of producing laterally stable PDC drill bits, *SPE Drilling & Completion*, **23** (3), 314–324, (2008).
- Navarro-Lopez, E. M. and Suarez-Cortez, R. Practical approach to modelling and controlling stick-slip oscillations in oilwell drillstrings, *Proceedings of the IEEE International Conference on Control Applications*, Taipei, Taiwan, 1454–1460, (2004).

- ¹¹ Fubin, S., Linxiu, S., Lin, L., and Qizhi, Z. Adaptive PID control of rotary drilling system with stick slip oscillation, *International Conference on Signal Processing Systems*, **2**, 289–292, (2010).
- ¹² Jijón, R. B., Canudas-de-Wit, C., Niculescu, S., and Dumon, J. Adaptive observer design under low data rate transmission with applications to oil well drill-string, *Proceedings of the American Control Conference*, Baltimore, Maryland, 1973–1978, (2010).
- ¹³ Canudas-de Wit, C., Rubio, F., and Corchero, M. A. D-OSKIL: A new mechanism for controlling stick-slip oscillations in oil well drillstrings, *IEEE Trans. Control Sys. Tech.*, **16**, 1177–1191, (2008).
- ¹⁴ Lin, L., Qizhi, Z., and Nurzat, R. Time-varying sliding mode adaptive control for rotary drilling system, *Journal of Computers*, **6** (3), 564–570, (2011).
- ¹⁵ Majeed, F. A., Karki, H., Magid, Y. A., and Karkoub, M. Managing oil drilling efficiency in bend drill pipes—An under actuated system perspective, *Proceedings of World Congress on Sustainable Technologies*, IEEE, UK/RI Chapter, 129–133, (2011).
- ¹⁶ Dareing, D. W. Drill collar length is a major factor in vibration control, *SPE Journal of Petroleum Technology*, **36** (4), 637–644, (1984).
- ¹⁷ Cobern, M. and Wassell, M. E. Laboratory testing of an active drilling vibration monitoring & control system, *AADE National Technical Conference and Exhibition*, Houston, Texas, (2005).
- ¹⁸ Cobern, M., Perry, C. A., Barbely, J. A., Burgess, D. E., and Wassell, M. E. Drilling tests of an active vibration damper, *SPE/IADC Drilling Conference*, (2007).
- ¹⁹ Bailey, J. R., Biediger, E.A.O., Sundararaman, S., Carson, A. D., Elks, W. C., Dupriest, F. E. Development and application of a BHA vibrations model, *International Petroleum Technology Conference*, Kuala Lumpur, Malaysia, (2008).
- ²⁰ Kim, K. J., Eman, K. F., and Wu, S. M. Identification of natural frequencies and damping ratios of machine tool structures by the dynamic data system approach, *International Journal of Machine Tools Design*, **24** (3), 161–169, (1984).
- ²¹ Bodruzzaman, M., Devgan, S. S., Mach, K. D., and Clay, C. High-resolution estimation and on-line monitoring of natural frequency of aircraft structure specimen under random vibration, *Proceedings of the IEEE Aerospace and Electronics Conference*, (1994).
- ²² Xu, X., Zhang, Z., Hua, H., and Chen, Z. Identification of time-varying modal parameters using a time-varying autoregressive approach, *Imac-Xxi: Conference & Exposition on Structural Dynamics*, (2003).
- ²³ Navarro-Lopez, E. M. and Cortes, D. Sliding-mode control of a multi-DOF oil well drill string with stick-slip oscillations, *Proceedings of the American Control Conference*, 3837–3842, (2007).
- ²⁴ Majeed, F. A., Karki, H., Magid, Y. A., and Karkoub, M. Analysis of the method of black box modeling of drill string dynamics by least squares method, *Proceedings of International Conference on Mechanical and Electrical Technology*, 257–261, (2010).
- ²⁵ Basu, B., Nagarajaiah, S., and Chakraborty, A. Online identification of linear time-varying stiffness of structural systems by wavelet analysis, *Structural Health Monitoring*, **7** (1), 21–36, (2008).

APPENDIX A

For online identification of natural frequency of a multi-DOF system by wavelet transforms, a linear MDOF system with m degrees of freedom represented by

$$\mathbf{M}\ddot{\mathbf{X}} + \mathbf{C}(t)\dot{\mathbf{X}} + \mathbf{K}(t)\mathbf{X} = \mathbf{R}f(t);$$

is considered, where \mathbf{M} , $\mathbf{C}(t)$, and $\mathbf{K}(t)$ are the mass, time-varying damping, and time-varying stiffness matrices, respectively; \mathbf{R} is the influence vector for forces at different degrees of freedom; and $f(t)$ is a forcing function. The displacement response vector is denoted by $\mathbf{X}(t)$.

If the elements K_{lj} ; $l, j = 1, \dots, m$ in the stiffness matrix have discontinuities at a finite number of points, then it is possible to divide the time in several segments with indices arranged as to $t_0 < t_1 < \dots < t_n$ such that all K_{lj} ; $l, j = 1, \dots, m$ are a continuous function in $[t_{i-1}, t_i]$. Further, it is assumed that the variations of all K_{lj} are slower than the fundamental (lowest) frequency of the system (corresponding to the longest period). It subsequently follows that assuming a variation of $\mathbf{X}(t)$ with slowly varying amplitude $\phi(t)_i^k$ and slowly varying frequency $\omega_{ki}(t)$ at the k^{th} mode in the time interval $[t_{i-1}, t_i]$, the displacement vector and its derivatives can be represented by

$$\begin{aligned} \mathbf{X} &= \phi(t)_i^k e^{i\omega_{ki}(t)t}; \\ \dot{\mathbf{X}} &= i\omega_{ki}(t)\phi(t)_i^k e^{i\omega_{ki}(t)t}; \\ \ddot{\mathbf{X}} &= -\omega_{ki}^2(t)\phi(t)_i^k e^{i\omega_{ki}(t)t}. \end{aligned}$$

Substitution of Eq. (11a)–(11c) in the homogeneous free vibration equation corresponding to Eq. (1) leads to the time-varying eigenvalue problem with eigenvalues $\omega_{ki}^2(t)$ and eigenvectors $\phi(t)_i^k$; $k = 1, 2, \dots, m$. If the system in Eq. (1) is assumed to be lightly damped, then using wavelet transformations, the natural frequency corresponding to the k^{th} mode in the j_k^{th} band can be obtained as

$$\omega_{0jk} = \frac{\sigma + 1}{2} \frac{\pi}{a_{jk}};$$

where a_{jk} is the discrete parameter used for wavelet transform and $a_j = \sigma^j$ where σ is a scalar.²⁵

An Outward-Wave-Favouring Finite Element-Based Strategy for Exterior Acoustical Problems

C. S. Jog

Facility for Research in Technical Acoustics (FRITA), Dept. of Mechanical Engg., Indian Institute of Science, Bangalore 560012, India

(Received 30 November 2011, revised 10 September 2012, accepted 14 November 2012)

This work presents a finite element-based strategy for exterior acoustical problems based on an assumed pressure form that favours outgoing waves. The resulting governing equation, weak formulation, and finite element formulation are developed both for coupled and uncoupled problems. The developed elements are very similar to conventional elements in that they are based on the standard Galerkin variational formulation and use standard Lagrange interpolation functions and standard Gaussian quadrature. In addition and in contrast to wave envelope formulations and their extensions, the developed elements can be used in the immediate vicinity of the radiator/scatterer. The method is similar to the perfectly matched layer (PML) method in the sense that each layer of elements added around the radiator absorbs acoustical waves so that no boundary condition needs to be applied at the outermost boundary where the domain is truncated. By comparing against strategies such as the PML and wave-envelope methods, we show that the relative accuracy, both in the near and far-field results, is considerably higher.

1. INTRODUCTION

The main difficulty that arises in solving exterior acoustical problems is the unboundedness of the domain. Although the boundary element method yields accurate results, the computational cost and memory requirements for large-scale problems can be prohibitive. Finite element methods can be more cost-effective due to the sparse nature of the matrices. Among the finite element-based techniques, one popular approach has been to truncate the computational domain at some distance away from the radiator or scatterer, and to impose a boundary condition at this artificial boundary (see Givoli¹ for a description of the classical approaches and to Qi and Geers² for a relatively recent approach known as the perfectly matched layer (PML)). Yet another approach involves infinite elements.³⁻⁹ Both approaches have their merits and demerits, which have been discussed in detail in the references cited.

Most of the work towards improving the former approach has focused either on devising and implementing higher-order absorbing conditions or on modifying these conditions to make them applicable for non-spherical truncation boundaries. The goal in this study is to improve upon the former approach, not by modifying the boundary conditions, but by modifying the function that is being solved for, namely the pressure field. The assumed form of the pressure field favours outgoing waves, which makes it easier for the resulting finite element formulation to capture the solution. Summarizing, note the following:

1. The proposed formulation is a modification of the conventional approach based on absorbing boundary conditions; the computational domain and input data are exactly the same; and the computational cost is also almost the same as for the conventional formulation.
2. The most crucial aspect of the proposed formulation is that

it is based on a Cartesian framework and, thus, avoids the cumbersome use of angular coordinates and the problems associated with them. In particular, it allows the elements to be used directly in the vicinity of the radiator or scatterer, which is in contrast to existing wave envelope and related formulations, where an inner mesh of conventional elements has to be used, leading to poorer accuracy (see section 4.2 for a comparison). In addition, there is no problem of ill-conditioning, as for example, occurs in the radial-direction matrices in some infinite finite element formulations (see, e.g., Bhandakkar and Jog⁹ and Dreyer and Estorff¹⁰). Although researches have attempted to alleviate this ill-conditioning¹⁰ the fact remains that non-standard interpolations, such as Legendre or Jacobi polynomials, must be used.

3. Since an oscillatory part is separated out in the proposed formulation, the resulting finite element formulation has to capture a more gently varying function in most problems, resulting in much higher accuracy compared to the conventional formulation. In this connection, I mention that both the near- and far-field results presented in this study were obtained from raw nodal values without the use of the Helmholtz integral equation (which can be computationally very expensive to evaluate and which is used to obtain accurate far-field results³⁻⁵).
4. Since it uses only a first-order (spherical) damper, the implementation is very simple. Similar to the PML method, each layer of elements added around the radiator/scatterer absorbs acoustical waves so that no boundary condition needs to be applied at the truncated boundary. Note that the PML method is not only more complicated but also fails to yield good accuracy even on relatively simple problems, such as the dilatational motion of a spherical surface unless

a large acoustical domain is used.² In addition, implementing the PML requires setting several numerical parameters such as the width of the layer and the number of divisions as well as the PML coefficients and their maximal values, requiring an optimization of these parameters.^{11,12} Methods that are coupled to the PML inherit its problems. For example, Huttunen, Kaipio, and Monk¹³ mention that several PML parameters must be properly adjusted to reduce numerical reflections to an acceptable level. Even after such an optimization is carried out, the accuracy could be poor, even on simple problems, as discussed in section 4.1. In contrast, in the proposed method—apart from the radius of the circumscribing spherical boundary—no factors need to be adjusted by the user.

Section 2 briefly presents the conventional formulation and then the proposed formulation, and section 3 extends the proposed formulation to coupled problems. Section 4 presents several numerical examples involving uncoupled/coupled and radiation/scattering problems. The conclusions are presented in section 5.

2. FORMULATION

Before presenting the proposed formulation, I briefly review the conventional formulation involving absorbing boundary conditions on the surface where the infinite domain is truncated. In this work, we consider only the case where the loading, and hence the pressure response, is time-harmonic, i.e.,

$$p = \tilde{p}e^{i\omega t}; \quad (1)$$

where ω is the angular frequency. The wave equation in this case reduces to the Helmholtz equation given by

$$\nabla^2 \tilde{p} + k^2 \tilde{p} = 0; \quad (2)$$

where, with c denoting the acoustic wave speed, $k = \omega/c$ is the wave number. Although in interior acoustical problems (in the absence of absorbers), \tilde{p} is real-valued; in the case of the exterior problem being solved in this study, \tilde{p} is complex-valued because of the damping-like effect that arises due to the infinite domain (see Eq. (9) below). If Ω denotes the domain over which the problem is being solved, Γ denotes its boundary and \mathbf{n} denotes the unit normal to the boundary, then the variational formulation of the above equation, obtained by multiplying Eq. (2) by the variation p_δ and carrying out an appropriate integration by parts, is given by

$$\int_{\Omega} (\nabla p_\delta \cdot \nabla \tilde{p} - k^2 p_\delta \tilde{p}) d\Omega = \int_{\Gamma} p_\delta \nabla \tilde{p} \cdot \mathbf{n} d\Gamma. \quad (3)$$

In an exterior radiation problem, the normal velocity v_n is specified over part of the boundary Γ_r , while over the part of the boundary Γ_∞ where the domain is truncated, appropriate absorbing conditions (see below) that approximate the Sommerfeld radiation condition are specified. In a scattering problem, the total pressure \tilde{p} is assumed to be decomposed into an incident pressure field p_{inc} and a scattered field p_{scat} , both of which individually satisfy Eq. (2), and the scattered field satisfies the Sommerfeld radiation condition as well. Thus, in the

scattering problem, we can solve for the scattered field by replacing \tilde{p} with p_{scat} in Eq. (3). If the boundary over which the scattering occurs is denoted by Γ_s and u_n denotes the normal displacement of the scatterer boundary, then

$$\nabla \tilde{p} \cdot \mathbf{n} = \nabla p_{\text{inc}} \cdot \mathbf{n} + \nabla p_{\text{scat}} \cdot \mathbf{n} = \rho_f \omega^2 u_n;$$

which implies that

$$\nabla p_{\text{scat}} \cdot \mathbf{n} = -\nabla p_{\text{inc}} \cdot \mathbf{n} + \rho_f \omega^2 u_n.$$

Thus, with ρ_f denoting the density of the acoustical fluid, the boundary conditions on the radiating and scattering surfaces Γ_r and Γ_s are

$$\nabla \tilde{p} \cdot \mathbf{n} = -\rho_f i \omega v_n \quad (\text{radiation}); \quad (4a)$$

$$\nabla p_{\text{scat}} \cdot \mathbf{n} = -\nabla p_{\text{inc}} \cdot \mathbf{n} + \rho_f \omega^2 u_n \quad (\text{scatterer}). \quad (4b)$$

If, for example, the incident wave is a plane wave of the form

$$p_{\text{inc}} = p_i e^{i\mathbf{k} \cdot \mathbf{x}}; \quad (5)$$

where \mathbf{x} is the position vector, then

$$\nabla p_{\text{inc}} \cdot \mathbf{n} = p_i i(\mathbf{k} \cdot \mathbf{n}) e^{i\mathbf{k} \cdot \mathbf{x}}.$$

Although I present the formulation for the radiation problem below, the formulation for the scattering problem can be obtained by replacing \tilde{p} with p_{scat} . I take Γ_∞ to be a sphere of radius R throughout this work and use a spherical damper of the form used by Bayliss and Turkel¹⁴:

$$\nabla \tilde{p} \cdot \mathbf{n} = -\frac{\tilde{p}}{R} - ik\tilde{p}. \quad (6)$$

The finite element formulation is obtained by discretizing the pressure field and its variation as

$$\tilde{p} = \mathbf{N}_p \hat{\mathbf{p}}, \quad p_\delta = \mathbf{N}_p \hat{\mathbf{p}}_\delta; \quad (7a)$$

$$\nabla \tilde{p} = \mathbf{B}_p \hat{\mathbf{p}}, \quad \nabla p_\delta = \mathbf{B}_p \hat{\mathbf{p}}_\delta; \quad (7b)$$

where $\mathbf{N}_p = [N_1 \ N_2 \ \dots]$ is the standard Lagrange shape function matrix, and

$$\mathbf{B}_p = \begin{bmatrix} \frac{\partial N_1}{\partial x} & \frac{\partial N_2}{\partial x} & \dots \\ \frac{\partial N_1}{\partial y} & \frac{\partial N_2}{\partial y} & \dots \\ \frac{\partial N_1}{\partial z} & \frac{\partial N_2}{\partial z} & \dots \end{bmatrix}. \quad (8)$$

By substituting the above discretizations into Eq. (3) and using the arbitrariness of $\hat{\mathbf{p}}_\delta$, we obtain the finite element equations

$$[\mathbf{K}_p - \omega^2 \mathbf{M}_p + i\omega \mathbf{C}_p] \hat{\mathbf{p}} = \hat{\mathbf{f}}_p; \quad (9)$$

where with R written as $|\mathbf{x}|$,

$$\mathbf{K}_p = \int_{\Omega} \mathbf{B}_p^T \mathbf{B}_p d\Omega + \int_{\Gamma_\infty} \frac{1}{|\mathbf{x}|} \mathbf{N}_p^T \mathbf{N}_p d\Gamma; \quad (10)$$

$$\mathbf{M}_p = \int_{\Omega} \frac{1}{c^2} \mathbf{N}_p^T \mathbf{N}_p d\Omega; \quad (11)$$

$$\mathbf{C}_p = \int_{\Gamma_\infty} \frac{1}{c} \mathbf{N}_p^T \mathbf{N}_p d\Gamma; \quad (12)$$

$$\hat{\mathbf{f}}_p = - \int_{\Gamma_r} \rho_f i \omega v_n \mathbf{N}_p^T d\Gamma. \quad (13)$$

For the scattering problem, where, for example, the incident wave is given by Eq. (5),

$$\hat{\mathbf{f}}_p = - \int_{\Gamma_s} p_i i(\mathbf{k} \cdot \mathbf{n}) e^{i\mathbf{k} \cdot \mathbf{x}} \mathbf{N}_p^T d\Gamma.$$

Note that in the above formulation, the damping matrix \mathbf{C}_p is exclusively due to the boundary condition on Γ_∞ . If (ξ, η) are the natural coordinates used for parametrizing the surface, then the expressions for the normal and the area element are

$$\mathbf{n} = \frac{\frac{\partial \mathbf{x}}{\partial \xi} \times \frac{\partial \mathbf{x}}{\partial \eta}}{\left\| \frac{\partial \mathbf{x}}{\partial \xi} \times \frac{\partial \mathbf{x}}{\partial \eta} \right\|};$$

$$d\Gamma = \left\| \frac{\partial \mathbf{x}}{\partial \xi} \times \frac{\partial \mathbf{x}}{\partial \eta} \right\| d\xi d\eta.$$

Since the same interpolation functions are used for \tilde{p} and p_δ (see Eq. (7a)), the above formulation corresponds to the Bubnov-Galerkin method. Other choices, such as, for example, the interpolation functions for p_δ and \tilde{p} being complex-conjugates of each other, are also possible; see Astley¹⁵ and Eq. (29).

The proposed formulation is as follows. Instead of the pressure assumed to be of the form given by Eq. (1), we assume it to be of the form

$$p = \frac{1}{|\mathbf{x}|} G(\mathbf{x}) e^{i(\omega t - k|\mathbf{x}|)}; \quad (14)$$

where $|\mathbf{x}| = \sqrt{\mathbf{x} \cdot \mathbf{x}}$, and $G(\mathbf{x})$ is an unknown complex-valued function which is to be determined by an approximation strategy such as the finite element method. The above form assumes that the ‘‘centre’’ of the radiating body is at the origin; if instead the centre is at \mathbf{x}_0 , \mathbf{x} should be replaced with $\mathbf{x} - \mathbf{x}_0$ in the above expression. Note the following:

1. The form of the pressure in Eq. (14) favours outgoing waves, while the form in Eq. (1), allows for both incoming and outgoing waves. The spherical damping condition given by Eq. (6) and (15) below leads to the condition $(\nabla G) \cdot \mathbf{n} = 0$ on Γ_∞ . Thus, similar to the PML, no boundary condition needs to be imposed on Γ_∞ . A higher-order damper was also tried but did not result in any significant improvement in the results.
2. From Atkinson,¹⁶ we know that the far-field pressure is proportional to $e^{-ik|\mathbf{x}|}/|\mathbf{x}|$, which provides a justification for the use of Eq. (14). In the near-field, of course, the field is generally more complicated, but the function $G(\mathbf{x})$ (to be determined) compensates for the difference. The fact that it does so effectively will be shown in section 4 by means of various nontrivial problems in which $G(\mathbf{x})$ has a complicated variation.
3. Since the oscillatory part is separated, $G(\mathbf{x})$ is a more gently varying function compared to \tilde{p} , resulting in higher overall accuracy, as will be clear in section 4.

4. The differences of the proposed formulation from the wave envelope formulation of Astley¹⁷ and Astley and Eversman¹⁸ are discussed at the end of this section.
5. The use of $|\mathbf{x}|$ instead of the radial spherical coordinate r is the most critical aspect of the proposed formulation; it ensures that the formulation can be carried out with respect to a Cartesian basis, thus avoiding the use of angular coordinates, which can be quite cumbersome.⁹ Since the formulation is then exactly analogous to that for conventional elements, one can use these elements in the direct vicinity of the radiator or scatterer (except when the origin is part of the acoustic domain, in which case, conventional elements are used in the vicinity of the origin as discussed towards the end of this section). Since in most situations, conventional elements do not need to be used at all, the use of the proposed method results in a dramatic reduction in computational cost. In contrast, with most infinite element formulations, one needs a mesh of conventional elements between the radiator/scatterer and a circumscribing boundary such as an ellipsoid, with infinite elements used in the exterior of this boundary. Although there have been attempts to alleviate this problem,¹⁹⁻²¹ they involve very complicated formulations.

We now derive the governing equations and boundary conditions for $G(\mathbf{x})$. From Eq. (1) and (14), we see that

$$\tilde{p} = \frac{1}{|\mathbf{x}|} G(\mathbf{x}) e^{-ik|\mathbf{x}|}. \quad (15)$$

Using the fact that

$$\nabla |\mathbf{x}| = \mathbf{x}/|\mathbf{x}|$$

and

$$\nabla(1/|\mathbf{x}|) = -\mathbf{x}/|\mathbf{x}|^3;$$

we get

$$\nabla \tilde{p} = \left[\nabla G - \frac{1}{|\mathbf{x}|} ik \mathbf{x} G - \frac{1}{|\mathbf{x}|^2} \mathbf{x} G \right] \frac{e^{-ik|\mathbf{x}|}}{|\mathbf{x}|}; \quad (16)$$

$$\nabla^2 \tilde{p} = \left[\nabla^2 G - \frac{2}{|\mathbf{x}|} ik \nabla G \cdot \mathbf{x} - \frac{2}{|\mathbf{x}|^2} \nabla G \cdot \mathbf{x} - k^2 G \right] \frac{e^{-ik|\mathbf{x}|}}{|\mathbf{x}|}. \quad (17)$$

Substituting Eqs. (15) and (17) into Eq. (2), we get the governing equation for $G(\mathbf{x})$ as

$$\nabla^2 G - \frac{2}{|\mathbf{x}|} \left(ik + \frac{1}{|\mathbf{x}|} \right) \nabla G \cdot \mathbf{x} = 0. \quad (18)$$

If \mathbf{n} denotes the unit normal to the boundary, then from Eq. (16), we get

$$\nabla G \cdot \mathbf{n} - \frac{1}{|\mathbf{x}|} \left(ik + \frac{1}{|\mathbf{x}|} \right) (\mathbf{x} \cdot \mathbf{n}) G = |\mathbf{x}| e^{ik|\mathbf{x}|} (\nabla \tilde{p} \cdot \mathbf{n}). \quad (19)$$

The variational formulation for G is obtained by multiplying Eq. (18) by the variation G_δ and carrying out an appropriate

integration by parts. We get

$$\int_{\Omega} \left[\nabla G_{\delta} \cdot \nabla G + \frac{2}{|\mathbf{x}|} G_{\delta} \left(ik + \frac{1}{|\mathbf{x}|} \right) \nabla G \cdot \mathbf{x} \right] d\Omega = \int_{\Gamma} G_{\delta} \nabla G \cdot \mathbf{n} d\Gamma. \quad (20)$$

Substituting Eq. (19) into Eq. (20), we get

$$\int_{\Omega} \left[\nabla G_{\delta} \cdot \nabla G + \frac{2}{|\mathbf{x}|} G_{\delta} \left(ik + \frac{1}{|\mathbf{x}|} \right) \nabla G \cdot \mathbf{x} \right] d\Omega - \int_{\Gamma} \frac{1}{|\mathbf{x}|} G_{\delta} \left(ik + \frac{1}{|\mathbf{x}|} \right) (\mathbf{x} \cdot \mathbf{n}) G d\Gamma = \int_{\Gamma} G_{\delta} |\mathbf{x}| e^{ik|\mathbf{x}|} (\nabla \tilde{p} \cdot \mathbf{n}) d\Gamma. \quad (21)$$

On the radiating surface Γ_r , $\nabla \tilde{p} \cdot \mathbf{n}$ is as given by Eq. (4a), while on Γ_{∞} , by using Eq. (6) and (15), we have $\nabla G \cdot \mathbf{n} = 0$; thus, similar to the PML, no boundary condition needs to be imposed on Γ_{∞} . It follows that, for a radiation problem, Eq. (21) can be written as

$$\int_{\Omega} \left[\nabla G_{\delta} \cdot \nabla G + \frac{2}{|\mathbf{x}|} G_{\delta} \left(ik + \frac{1}{|\mathbf{x}|} \right) \nabla G \cdot \mathbf{x} \right] d\Omega - \int_{\Gamma_r} \frac{1}{|\mathbf{x}|} G_{\delta} \left(ik + \frac{1}{|\mathbf{x}|} \right) (\mathbf{x} \cdot \mathbf{n}) G d\Gamma = - \int_{\Gamma_r} G_{\delta} |\mathbf{x}| e^{ik|\mathbf{x}|} \rho_f i \omega v_n d\Gamma. \quad (22)$$

Note that on the surface Γ_r , the term $e^{ik|\mathbf{x}|}$ does not vary rapidly (e.g., if Γ_r is a sphere, then it is a constant), and hence standard Gaussian quadrature can be used. Note also that on symmetry surfaces in the finite element model where $\nabla \tilde{p} \cdot \mathbf{n} = 0$, since $\mathbf{x} \cdot \mathbf{n} = 0$, it follows from Eq. (19) that $\nabla G \cdot \mathbf{n}$ is also zero.

The finite element formulation is obtained by discretizing G using the same interpolations as used for \tilde{p} in Eq. (7), i.e.,

$$G = N_p \hat{g}, \quad G_{\delta} = N_p \hat{g}_{\delta}; \quad (23a)$$

$$\nabla G = B_p \hat{g}, \quad \nabla G_{\delta} = B_p \hat{g}_{\delta}, \quad (23b)$$

with B_p given by Eq. (8). Substituting these interpolations into Eq. (22), and using the arbitrariness of \hat{g}_{δ} , we get the finite element matrix equation as

$$[\mathbf{K}_g + i\omega \mathbf{C}_g] \hat{g} = \hat{f}_g; \quad (24)$$

where

$$\mathbf{K}_g = \int_{\Omega} \left[B_p^T B_p + \frac{2}{|\mathbf{x}|^2} N_p^T \mathbf{x}^T B_p \right] d\Omega - \int_{\Gamma_r} \frac{\mathbf{x} \cdot \mathbf{n}}{|\mathbf{x}|^2} N_p^T N_p d\Gamma; \quad (25)$$

$$\mathbf{C}_g = \int_{\Omega} \frac{2}{c|\mathbf{x}|} N_p^T \mathbf{x}^T B_p d\Omega - \int_{\Gamma_r} \frac{\mathbf{x} \cdot \mathbf{n}}{c|\mathbf{x}|} N_p^T N_p d\Gamma; \quad (26)$$

$$\hat{f}_g = - \int_{\Gamma_r} \rho_f i \omega v_n |\mathbf{x}| e^{ik|\mathbf{x}|} N_p^T d\Gamma. \quad (27)$$

Comparing Eq. (24) with Eq. (9), we see that in the proposed formulation, the M_p matrix is absent, while the damping terms are due to integrals over the domain Ω and boundary Γ_r instead of over Γ_{∞} . In addition, because outgoing waves are favoured, the matrices are also unsymmetric. However, since the matrices are still sparse, it does not result in a significant increase in computational cost. Once \hat{g} is determined, the pressure field is recovered using Eq. (15).

In the case of scattering by a rigid body, we approximate the scattered field p_{scat} as $G(\mathbf{x})e^{-ik|\mathbf{x}|}/|\mathbf{x}|$ so that we end up with the same equation as Eq. (24) with Γ_s in the place of Γ_r , and the load vector, when the incident wave is as given by Eq. (5), now given by

$$\hat{f}_g = - \int_{\Gamma_s} p_i i(\mathbf{k} \cdot \mathbf{n}) |\mathbf{x}| e^{i(\mathbf{k} \cdot \mathbf{x} + k|\mathbf{x}|)} N_p^T d\Gamma.$$

When the origin is part of the acoustical domain (e.g., radiation from a circular plate in a baffle), we use conventional elements in the region between the radiator (or scatterer) and a sphere Γ_1 whose radius is denoted by r_1 , and the proposed elements in the region between Γ_1 and Γ_{∞} . In order to ensure continuity of the pressure field at the interface Γ_1 , we modify Eq. (15) to

$$\tilde{p} = \frac{r_1}{|\mathbf{x}|} G(\mathbf{x}) e^{ik(r_1 - |\mathbf{x}|)}. \quad (28)$$

The matrix formulation presented in Eq. (24) remains unaltered because of this scaling by a constant—the only difference being that one multiplies the expression for \hat{f}_g by e^{-ikr_1}/r_1 , and one uses Eq. (28) instead of Eq. (15) while recovering the actual pressure field from $G(\mathbf{x})$. The matrix formulation for the conventional formulation also remains unaltered except that matrices that are evaluated over Γ_{∞} are now evaluated over Γ_1 , ensuring continuity of $\nabla \tilde{p} \cdot \mathbf{n}$ (in a weak sense) between the two types of elements.

It may appear that an approximation of the type $\tilde{p} = G(\mathbf{x})e^{-ik|\mathbf{x}|}$ may bypass the use of conventional elements altogether, even when the origin is part of the acoustic domain; however, numerical experiments show that the results are poor in the vicinity of the origin since $\nabla \tilde{p}$ has a term $\mathbf{x}/|\mathbf{x}|$ that becomes indeterminate at the origin, leading to ill-conditioning. The second-order damper presented in the work of Bossut and Decarpigny²² was also tried both with this approximation and the conventional formulation, but resulted only in a marginal improvement, especially since I ensured that R is chosen such that $kR \gg 1$.

In the wave-envelope method of Astley and Eversman^{17,18} one substitutes

$$\tilde{p} = \frac{1}{|\mathbf{x}|} G(\mathbf{x}) e^{-ik|\mathbf{x}|}; \quad p_{\delta} = \frac{1}{|\mathbf{x}|} G_{\delta}(\mathbf{x}) e^{ik|\mathbf{x}|}; \quad (29)$$

into the conventional variational formulation given by Eq. (3). The result is equations of the same form as Eq. (24), but with different \mathbf{K}_g , \mathbf{C}_g and \hat{f}_g matrices as given by

$$\mathbf{K}_g = \int_{\Omega} \frac{1}{|\mathbf{x}|^2} \left[B_p^T B_p + \frac{1}{|\mathbf{x}|^2} \left(N_p^T N_p - N_p^T \mathbf{x}^T B_p - B_p^T \mathbf{x} N_p \right) \right] d\Omega + \int_{\Gamma_{\infty}} \frac{1}{|\mathbf{x}|^3} N_p^T N_p d\Gamma; \quad (30)$$

$$C_g = \int_{\Omega} \frac{1}{c|\mathbf{x}|^3} \left[\mathbf{N}_p^T \mathbf{x}^T \mathbf{B}_p - \mathbf{B}_p^T \mathbf{x} \mathbf{N}_p \right] d\Omega + \int_{\Gamma_{\infty}} \frac{1}{c|\mathbf{x}|^2} \mathbf{N}_p^T \mathbf{N}_p d\Gamma; \quad (31)$$

$$\hat{\mathbf{f}}_g = - \int_{\Gamma_r} \frac{1}{|\mathbf{x}|} \rho_f i \omega v_n e^{ik|\mathbf{x}|} \mathbf{N}_p^T d\Gamma. \quad (32)$$

When used in conjunction with conventional elements, one again uses Eq. (28) for the pressure and its complex conjugate for the variation so that one multiplies the above $\mathbf{K}_g, \mathbf{C}_g$ by r_1^2 and $\hat{\mathbf{f}}_g$ by r_1/e^{ikr_1} . Since the weak continuity of $\nabla \hat{p} \cdot \mathbf{n}$ is automatically satisfied, no boundary condition needs to be imposed at Γ_1 . Note the following:

1. The derivation of the above wave envelope elements has been carried out using the same critical idea of replacing r by $|\mathbf{x}|$ as used for the proposed method and thus leads to the same advantage of being able to replace conventional elements in most problems. In line with the equivalence shown between these two approaches for some one-dimensional problems with piecewise-linear shape functions,²³ the results obtained using the above approach are very similar to the results obtained using the proposed formulation. (Note, however, that the matrix expressions as given by Eqs. (25)–(27) are not only more compact, and hence more economical to compute, but are also simpler to implement since they do not involve any integrals over Γ_{∞} .) The original wave envelope formulation^{17,18} is, however, based on a separation of the shape functions into radial and angular directions necessitating the use of an inner mesh of conventional elements and leading to poorer accuracy, as shown in section 4.
2. The radial direction is treated in a special manner even in recent enhancements of the wave envelope formulation in the literature, and other complications are involved, such as the need to choose weighting functions for these elements and the location of virtual source nodes; for example, see the rather involved way of constructing the radial shape functions as discussed in section IIC of Astley et al.,²⁰ or as discussed by Cremers and Fyfe,²⁴ the difficulties associated with identifying the source location for radiators of arbitrary shape, which can lead to large meshes of conventional elements. Again, in contrast, in this formulation, the radial direction is not treated in a special manner, since the oscillatory terms associated with the radial direction have already been eliminated a priori (thus, we use standard Lagrange shape functions). And since they are similar to conventional elements, no factors need to be adjusted, no weights need to be chosen, and no virtual source nodes need to be identified.

3. COUPLED FORMULATION

I first briefly present the so-called pressure formulation²⁵ for coupled problems within the conventional setup and then present a formulation analogous to this pressure formulation for the proposed method. Assume that three-dimensional elements, such as tetrahedral or hexahedral elements, are used to

conduct the structural analysis. If $\hat{\mathbf{u}}$ denotes the vector of the displacement degrees of freedom,

$$\mathbf{N}_u = \begin{bmatrix} N_1 & 0 & 0 & N_2 & 0 & 0 & \dots \\ 0 & N_1 & 0 & 0 & N_2 & 0 & \dots \\ 0 & 0 & N_1 & 0 & 0 & N_2 & \dots \end{bmatrix}; \quad (33)$$

denotes the shape function matrix (i.e., $\mathbf{u} = \mathbf{N}_u \hat{\mathbf{u}}$); Γ_{wet} denotes the wet surface (i.e., the interface between the structure and the acoustic fluid); \mathbf{n} denotes the unit normal to the surface; and $\mathbf{K}_s, \mathbf{M}_s,$ and \mathbf{C}_s denote the stiffness, mass, and damping matrices for the structure, then the matrix equations for a radiation problem can be written as

$$\begin{bmatrix} \mathbf{K}_{uu} & \mathbf{K}_{up} \\ \mathbf{K}_{pu} & \mathbf{K}_{pp} \end{bmatrix} \begin{bmatrix} \hat{\mathbf{u}} \\ \hat{\mathbf{p}} \end{bmatrix} = \begin{bmatrix} \hat{\mathbf{f}}_u \\ \hat{\mathbf{f}}_p \end{bmatrix}; \quad (34)$$

where, with $\mathbf{K}_p, \mathbf{M}_p, \mathbf{C}_p,$ and $\hat{\mathbf{f}}_p$ given by Eqs. (10)–(13),

$$\begin{aligned} \mathbf{K}_{uu} &= \mathbf{K}_s - \omega^2 \mathbf{M}_s + i\omega \mathbf{C}_s; \\ \mathbf{K}_{up} &= \int_{\Gamma_{\text{wet}}} \mathbf{N}_u^T \mathbf{n} \mathbf{N}_p d\Gamma; \\ \mathbf{K}_{pu} &= - \int_{\Gamma_{\text{wet}}} \rho_f \omega^2 \mathbf{N}_p^T \mathbf{n}^T \mathbf{N}_u d\Gamma; \\ \mathbf{K}_{pp} &= \mathbf{K}_p - \omega^2 \mathbf{M}_p + i\omega \mathbf{C}_p. \end{aligned}$$

The normal \mathbf{n} that occurs in the expressions for \mathbf{K}_{up} and \mathbf{K}_{pu} represents the outward unit normal to the structural and fluid domains, respectively. The load vector $\hat{\mathbf{f}}_u$ is due to the external loading on the structure; for example, if a given pressure p_s acts on part of the surface Γ_p , then $\hat{\mathbf{f}}_u = - \int_{\Gamma_p} p_s \mathbf{N}_u^T \mathbf{n} d\Gamma$. In the case of the scattering problem considered in the previous section, where the scattering now occurs over the wet surface Γ_{wet} , the above set of equations remains the same, with $\hat{\mathbf{p}}$ now denoting the nodal variables for the scattered pressure and

$$\begin{aligned} \hat{\mathbf{f}}_u &= - \int_{\Gamma_{\text{wet}}} p_i e^{i\mathbf{k} \cdot \mathbf{x}} \mathbf{N}_u^T \mathbf{n} d\Gamma \\ \hat{\mathbf{f}}_p &= - \int_{\Gamma_{\text{wet}}} p_i i(\mathbf{k} \cdot \mathbf{n}) e^{i\mathbf{k} \cdot \mathbf{x}} \mathbf{N}_p^T d\Gamma. \end{aligned}$$

Similar to the uncoupled formulation in the previous section and coupled formulation above, we get the coupled equations for the proposed formulation as

$$\begin{bmatrix} \mathbf{K}_{uu} & \mathbf{K}_{ug} \\ \mathbf{K}_{gu} & \mathbf{K}_{gg} \end{bmatrix} \begin{bmatrix} \hat{\mathbf{u}} \\ \hat{\mathbf{g}} \end{bmatrix} = \begin{bmatrix} \hat{\mathbf{f}}_u \\ \hat{\mathbf{f}}_g \end{bmatrix}; \quad (35)$$

where, with $\mathbf{K}_g, \mathbf{C}_g,$ and $\hat{\mathbf{f}}_g$ given by Eqs. (25)–(27),

$$\begin{aligned} \mathbf{K}_{uu} &= \mathbf{K}_s - \omega^2 \mathbf{M}_s + i\omega \mathbf{C}_s; \\ \mathbf{K}_{ug} &= \int_{\Gamma_{\text{wet}}} \frac{1}{|\mathbf{x}|} e^{-ik|\mathbf{x}|} \mathbf{N}_u^T \mathbf{n} \mathbf{N}_p d\Gamma; \\ \mathbf{K}_{gu} &= - \int_{\Gamma_{\text{wet}}} \rho_f \omega^2 |\mathbf{x}| e^{ik|\mathbf{x}|} \mathbf{N}_p^T \mathbf{n}^T \mathbf{N}_u d\Gamma; \\ \mathbf{K}_{gg} &= \mathbf{K}_g + i\omega \mathbf{C}_g - \int_{\Gamma_{\text{wet}}} \frac{\mathbf{x} \cdot \mathbf{n}}{|\mathbf{x}|} \left(ik + \frac{1}{|\mathbf{x}|} \right) \mathbf{N}_p^T \mathbf{N}_p d\Gamma. \end{aligned}$$

The load vector $\hat{\mathbf{f}}_u$ is as in the conventional formulation above for both the radiation and scattering problems. For the scattering problem,

$$\hat{\mathbf{f}}_g = - \int_{\Gamma_{wet}} p_i i(\mathbf{k} \cdot \mathbf{n}) |\mathbf{x}| e^{i\mathbf{k} \cdot \mathbf{x} + ik|\mathbf{x}|} \mathbf{N}_p^T d\Gamma.$$

As in the uncoupled case, once $\hat{\mathbf{g}}$ is found, \tilde{p} is recovered using Eq. (15). Thus, the great simplicity of formulation and implementation inherent in the uncoupled case carries over to the coupled problem.

For both the coupled and uncoupled problems presented above, an axisymmetric formulation can be developed easily from the three-dimensional formulation. If (r, z) represent the coordinates in the cylindrical coordinate system and ξ represents the natural coordinate parametrizing the boundary in the finite element framework, then the normal and the area element are given by

$$\mathbf{n} = \left(\frac{dz/d\xi}{\sqrt{(dr/d\xi)^2 + (dz/d\xi)^2}}, -\frac{dr/d\xi}{\sqrt{(dr/d\xi)^2 + (dz/d\xi)^2}} \right);$$

$$d\Gamma = 2\pi r \sqrt{\left(\frac{dr}{d\xi}\right)^2 + \left(\frac{dz}{d\xi}\right)^2} d\xi;$$

while the \mathbf{B}_p and \mathbf{N}_u matrices are obtained by a straightforward modification of Eqs. (8) and (33).

4. NUMERICAL EXAMPLES

I present several numerical examples, involving both radiation and scattering in the coupled and uncoupled frameworks, to illustrate the performance of the proposed method. The pressure values presented are directly the nodal values obtained from the finite element formulation, and no use is made of the Helmholtz integral equation to compute the far-field pressure, as is done in the case of some infinite elements.⁹ In many examples, a high value of R is deliberately chosen to show the high accuracy of the far-field pressure. The values of the input data and the corresponding results are in SI (or appropriate consistent) units.

Since the proposed method is similar to the conventional method, which uses absorbing boundary conditions (described briefly in section 2), I shall compare the proposed method with the conventional method; the similarity is borne out by the fact that both strategies use the same mesh and other input data. Wherever possible, we also carry out comparisons with other techniques such as the boundary element method, infinite element method, PML, ultra-weak variational formulation, etc. I use either 9-node axisymmetric elements or a combination of 18-node wedge and 27-node hexahedral elements in both the formulations. When used within the context of the conventional formulation, these elements are denoted by B9 and B18/B27, while they are denoted by A9 and W18/S27 when used within the context of the proposed formulation. In the coupled problems presented, standard displacement-based elements are used to conduct the structural analysis and are obviously of the same order as the acoustic elements in order

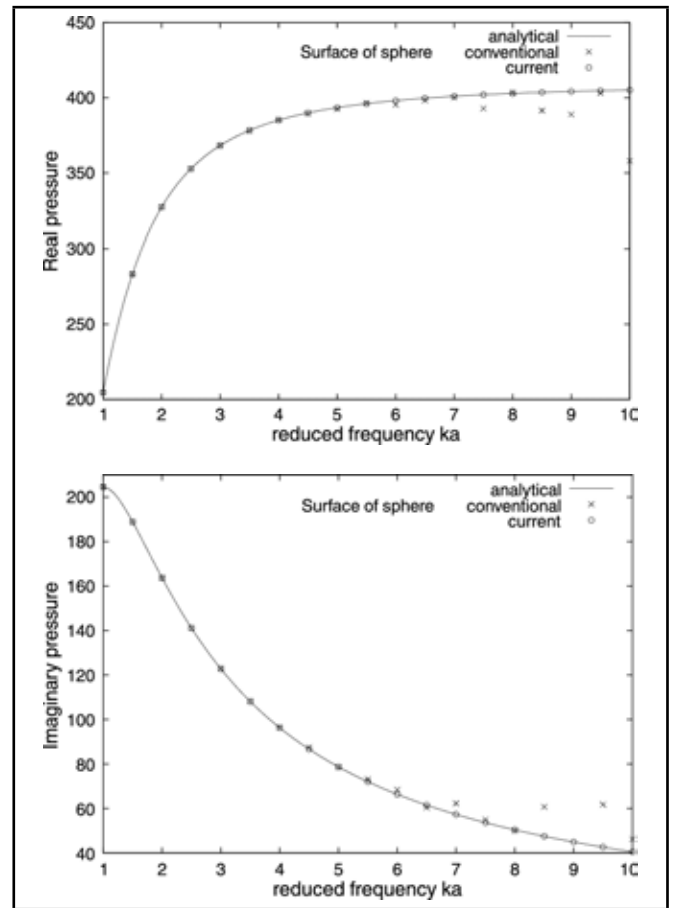


Figure 1. Comparison of the numerically and analytically obtained real and imaginary parts of the surface pressure for various frequencies in the pulsating sphere problem.

to maintain compatibility with the acoustic mesh. Full integration (in both the structural and acoustic elements) and uniform meshes are used in all the examples. The Watson Sparse Matrix Package solver is used to solve the system of equations.^{26,27}

4.1. Pulsating Sphere Problem

A sphere of radius $a = 10$ vibrates with uniform radial velocity $u_0 = 1$. The analytical solution²⁸ for the pressure as a function of the radial distance r is

$$\tilde{p}(r) = \frac{\rho_f c u_0}{r} \frac{ika^2}{1 + ika} e^{-ik(r-a)}.$$

Due to symmetry, I model only half of the sphere using a uniform mesh of 16×16 axisymmetric elements (almost identical results are obtained if one solves the problem using three-dimensional elements, i.e., by discretizing one-eighth of the domain using an equivalent mesh of 18-node wedge and 27-node hexahedral elements). The bounding surface is taken to be a sphere of radius $R = 50$. The properties used are $\rho_f = 1.2$ and $c = 341$. Since $G(\mathbf{x})$ is a constant in this problem, the exact solution is captured by the proposed method irrespective of the mesh density and bounding radius R . Thus, this problem acts like a patch test for the proposed formulation.

A comparison of the real and imaginary parts of the surface and far-field pressures against the analytical solution for various frequencies of oscillation is shown in Figs. (1) and (2).

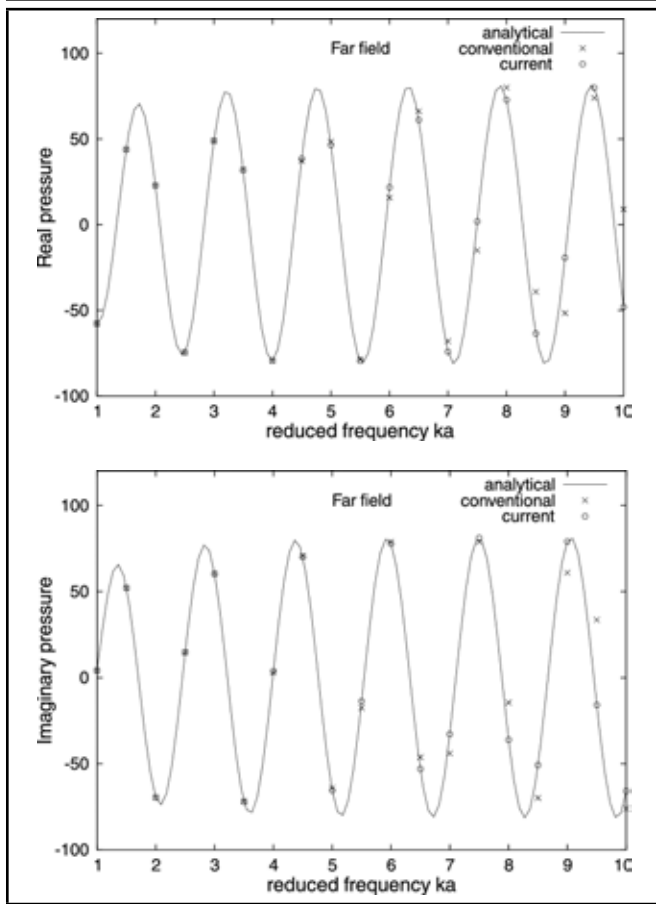


Figure 2. Comparison of the numerically and analytically obtained real and imaginary parts of the pressure at $r = 50$ for various frequencies in the pulsating sphere problem.

As seen from Figs. (1) and (2), although the conventional formulation yields good results at low frequencies, it results in significant errors at higher frequencies, while the proposed formulation yields very accurate results over the entire frequency range, even at points that lie on the outer bounding surface. I have also verified that the proposed formulation continues to yield the exact result, both in the near and far-field (including at $r = R$), over the entire frequency range when $R = 90$, with the same mesh density as used when $R = 50$, thus showing the insensitivity to mesh density in this particular example. In addition, one can obtain almost the exact particle velocity (which is proportional to $\nabla \tilde{p}$) over the entire frequency range, and over the entire domain.

Huttunen et al.¹³ consider the very similar problem of a point source, which is solved using the ultra-weak variational formulation combined with the PML. In spite of carrying out extensive tests to determine the optimal value of various parameters in their method and in spite of using a very fine mesh (see Huttunen et al.'s Fig. (2)), the errors in their solution are large (see Huttunen et al.'s Fig. (4)), even on this simple problem.

4.2. Oscillating Sphere Problem

A rigid sphere of radius $a = 10$ oscillates along the z -axis as shown in Fig. (3). The analytical solution²⁹ for the pressure as a function of the radial distance r from the centre of the sphere and the angle θ between the radius vector and the

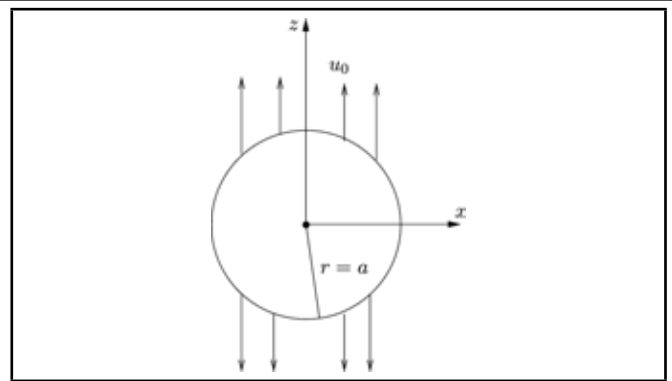


Figure 3. Oscillating sphere problem geometry.

velocity vector is

$$\tilde{p}(r, \theta) = \rho_f c u_0 \left(\frac{a}{r}\right)^2 \cos \theta \frac{i k a (1 + i k r)}{2(1 + i k a) - (k a)^2} e^{-i k (r - a)}.$$

An axisymmetric mesh of $n_r \times n_\theta = 16 \times 32$ is used to discretize the domain. The material properties and the value of R are chosen to be the same as in the pulsating sphere problem, and u_0 is taken as unity. The solution obtained at $(0, 0, a)$ and $(0, 0, R)$ for various frequencies of oscillation is shown in Figs. (4) and (5). The high relative accuracy of the proposed formulation is again evident from these figures. Almost the same high accuracy is obtained both in the near and far-field over the entire frequency range shown, even for a much larger choice of radius of the bounding sphere, such as $R = 90$ (with the same $n_r \times n_\theta$ mesh as used for $R = 50$).

Although I have shown the results only up to $ka = 10$, the agreement with the analytical solution continues to be good, both in the near and far-field, for very large ka . For example, for $ka = 200$ (when there are only 0.125 elements per wavelength), the analytical values of pressure at $r = 10$ and $r = 50$ are $(409.2, 2.046)$ and $(-36.015, -73.49)$, while the numerical values are $(409.242, 2.02)$ and $(-36.03, -73.5)$, respectively. As an illustration, the variation of the real part of the pressure (normalized using a factor of $\rho_f c u_0$) for $ka = 100$ as a function of r/a at $\theta = 0$, and as a function of $\cos \theta$ at $r = a$, using the same mesh and material data mentioned above, are shown in Fig. (6); note that the conventional method fails completely at these high frequencies.

Even beyond $ka = 200$, the accuracy of the proposed formulation reduces very gradually. In contrast, with the wave envelope method of Astley, Macaulay, and Coyette,¹⁹ there are differences between the analytical and numerical results even for as small a ka value as 2π (see Astley, Macaulay, and Coyette's Fig. (9b)).

4.3. Radiation from an Elastic Hollow Sphere

The inner surface of an elastic hollow sphere of inner and outer radii r_1 and r_2 is loaded with a uniform time-harmonic pressure $p_0 e^{i\omega t}$. If (λ, μ) denote the Lamé constants for the solid, and if ρ_s denotes its density, then the wave number in the solid is

$$k_s = \omega \sqrt{\rho_s} / \sqrt{\lambda + 2\mu}.$$

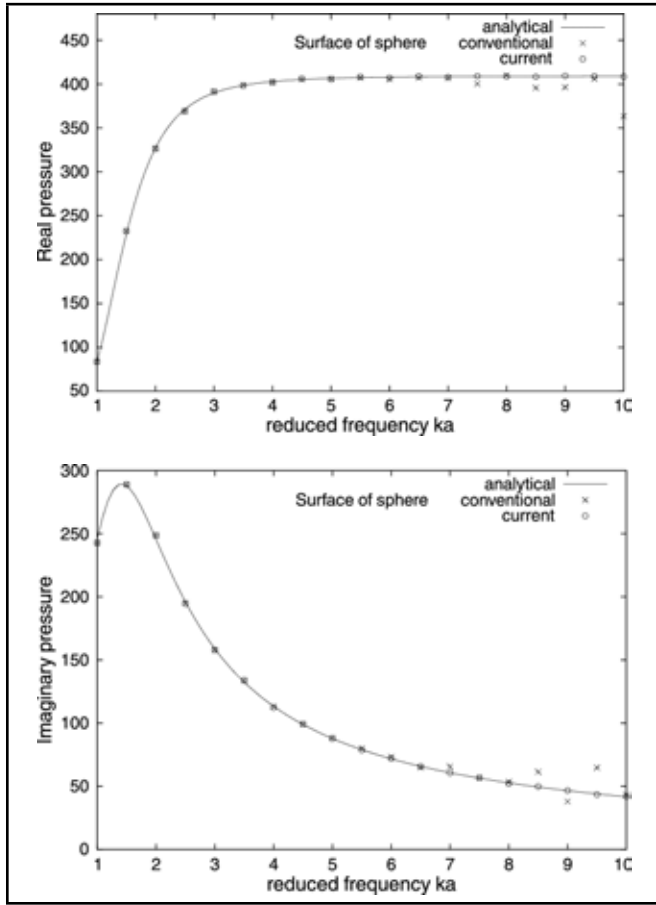


Figure 4. Comparison of the numerically and analytically obtained real and imaginary parts of the surface pressure for various frequencies in the oscillating sphere problem.

Using the approach outlined in Seybert, Wu, and Wu,³⁰ we find that the pressure field outside the sphere as a function of the radial coordinate r is given by

$$\tilde{p} = Ne^{-ikr}/(rD);$$

where

$$N = -2e^{i(kr_2+k_s(r_1+r_2))}k_s^3(\lambda + 2\mu)\omega^2p_0r_1^3r_2^3\rho_f;$$

$$D = e^{2ik_s r_1} [-4\mu + 4ik_s\mu r_1 + k_s^2(\lambda + 2\mu)r_1^2] \cdot \left[(-i + kr_2) \left(\frac{-4\mu - 4ik_s\mu r_2 + k_s^2(\lambda + 2\mu)r_2^2}{k_s^2(\lambda + 2\mu)r_2^2} \right) + \omega^2 r_2^2 (i - k_s r_2) \rho_f \right] - e^{2ik_s r_2} [-4\mu - 4ik_s\mu r_1 + k_s^2(\lambda + 2\mu)r_1^2] \cdot \left[(-i + kr_2) \left(\frac{-4\mu + 4ik_s\mu r_2 + k_s^2(\lambda + 2\mu)r_2^2}{k_s^2(\lambda + 2\mu)r_2^2} \right) + \omega^2 r_2^2 (i + k_s r_2) \rho_f \right].$$

We take $r_1 = 10$ m, $r_2 = 12.5$ m, $E = 2 \times 10^{11}$ Pa, $\nu = 0.25$ (where E and ν denote the Young modulus and Poisson ratio of the solid, respectively), $\rho_s = 7800$ kg/m³, $\rho_f = 1000$ kg/m³, $c = 1500$ m/s, and $p_0 = 1$ Pa (note that we have used properties for a heavy fluid where a coupled analysis is more relevant). A uniform mesh of 16×16 axisymmetric elements was used to mesh half the spherical domain, which comprises both the structure and the acoustic fluid (it has been verified that similar results are obtained using three-dimensional elements). The results for the pressure at the surface $r = 12.5$ m and at the bounding sphere $r = 50$ are shown

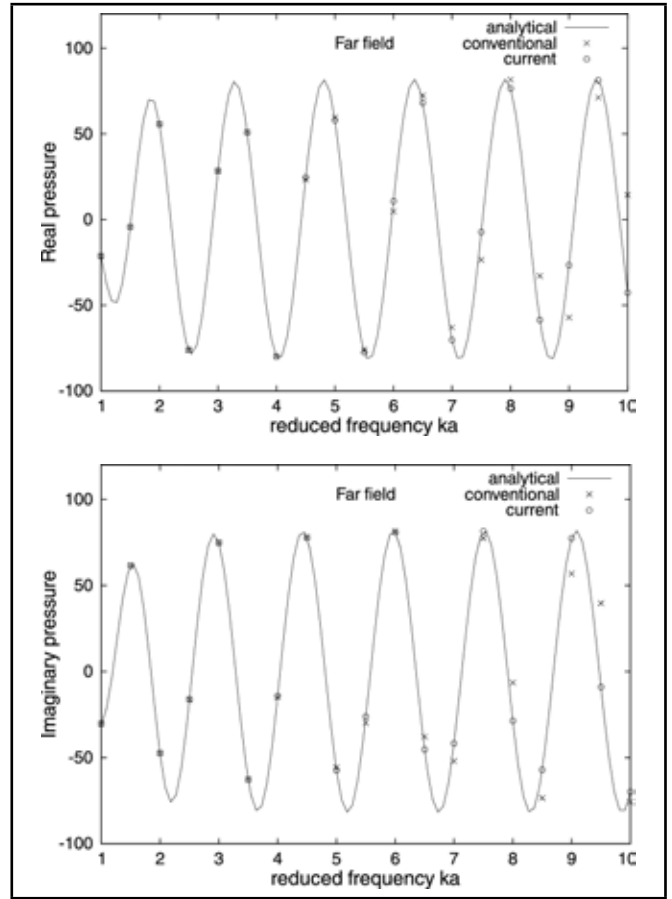


Figure 5. Comparison of the numerically and analytically obtained real and imaginary parts of the pressure at $r = 50$ for various frequencies in the oscillating sphere problem.

Table 1. Comparison of surface and far-field pressures in the hollow sphere radiation problem.

kr_1	B9	A9	Analytical
Surface pressure ($r = 12.5$)			
5	0.65368 - 0.18626i	0.65385 - 0.18657i	0.65359 - 0.18690i
8	0.01624 - 0.07858i	0.01662 - 0.08122i	0.01662 - 0.08122i
10	0.01187 - 0.05114i	0.00811 - 0.05596i	0.00811 - 0.05596i
Far-field pressure ($r = 50$)			
5	0.16793 - 0.02541i	0.16729 - 0.03016i	0.16723 - 0.03025i
8	0.01943 + 0.00618i	0.02070 + 0.00097i	0.02070 + 0.00097i
10	0.01188 - 0.00644i	0.00475 - 0.01331i	0.00475 - 0.01331i

in Table 1. Similar to the observation in the previous problems, the results obtained using the conventional formulation are poor at high frequencies, while the proposed formulation yields accurate results at high frequencies even in the far-field.

4.4. Scattering from a Rigid and Elastic Hollow Sphere

A plane wave of the form $p_i e^{ik_z z}$ is incident on a rigid sphere as shown in Fig. (7). The analytical solution³¹ for the scattered pressure field is given by

$$p_{\text{scat}} = -p_i \sum_{n=0}^{\infty} (2n + 1) i^n \frac{j'_n(ka)}{h'_n(ka)} h_n(kr) P_n(\cos \theta);$$

where r is the (spherical) radial coordinate, θ is the angle between the z -axis and the radial coordinate, j_n is the spherical Bessel function of the first kind, h_n is the Hankel function of the second kind, P_n are Legendre polynomials, and primes denote derivatives of the function.

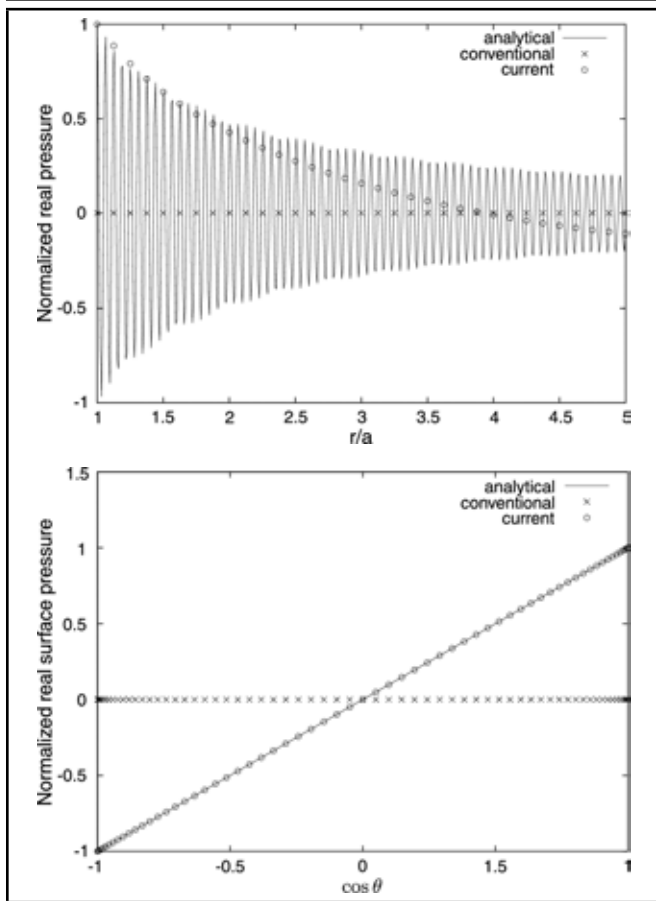


Figure 6. Comparison of the numerically and analytically obtained (normalized) real part of the pressure as a function of r/a and $\cos \theta$, respectively, for $ka = 100$ in the oscillating sphere problem.

We take $p_i = 1$, $a = 10$, $\rho_f = 1.2$, $c = 341$, $R = 50$, and discretize the domain using an $n_r \times n_\theta = 64 \times 32$ axisymmetric mesh. The backscattered pressure on the surface and in the far-field (i.e., $p_{scat}|_{\theta=\pi}$ at $r = 10$ and $r = 50$) is tabulated in Table 2. Both the B9 and A9 elements perform equally well in this case, both in the near and far-field. The reason is that even though the $e^{-ik|x|}$ component is present in the solution, the transverse part of the solution oscillates more rapidly than this part. Note, however, that even in such a case, the solution using the proposed strategy is no worse than the conventional one.

Now consider the case when the scattering is due to a hollow elastic sphere of inner radius b and outer radius a . Unlike

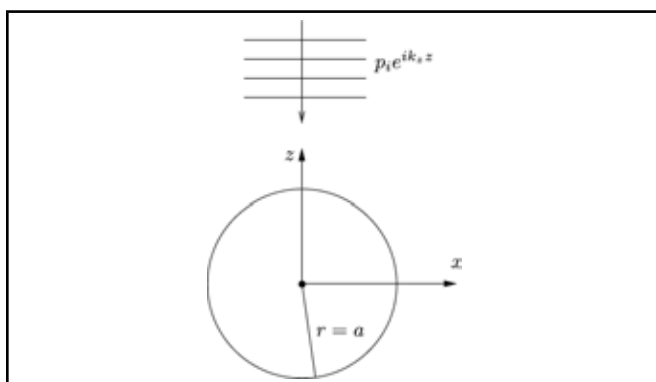


Figure 7. Scattering of a plane wave from a rigid sphere.

Table 2. Comparison of backscattered surface and far-field pressures when the sphere is rigid.

$k_z a$	B9		A9		Analytical	
	Surface backscattered pressure ($r = 10$)					
1	-0.51049	-0.22125i	-0.51049	-0.22125i	-0.50655	-0.22612i
5	-0.54813	-2.08572i	-0.54803	-2.08568i	-0.55389	-2.07178i
9	0.42105	-0.53238i	0.41863	-0.53435i	0.44242	-0.54739i
Far-field backscattered pressure ($r = 50$)						
1	0.04383	+0.01860i	0.04383	+0.01860i	0.04425	+0.01994i
5	0.11147	-0.42893i	0.11143	-0.42893i	0.11214	-0.43208i
9	-0.80695	-0.30955i	-0.80763	-0.30765i	-0.81531	-0.31005i

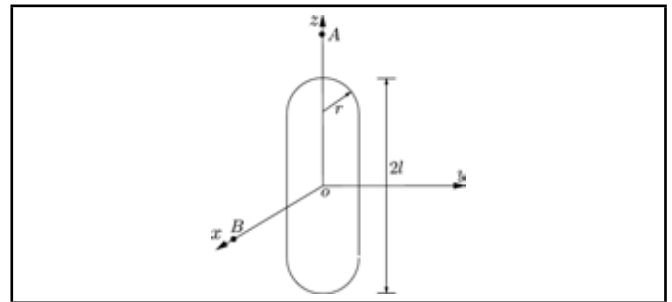


Figure 8. Pulsating cylinder with hemispherical end caps.

the case of the rigid sphere discussed above, this needs to be solved using the coupled formulation discussed in section 3. I use the same geometrical data and the data for hard rubber,³⁰ namely, $b = 0.5$ m, $a = 1$ m, $E = 2.3 \times 10^9$ Pa, $\nu = 0.4$, $\rho_s = 1100$ kg/m³, $\rho_f = 1026$ kg/m³, and $c = 1500$ m/s. I chose $R = 10.5$ and meshed the total domain (structure and acoustic fluid) using an $n_r \times n_\theta = 80 \times 64$ axisymmetric mesh and, in order to show the performance of the three-dimensional elements, one-fourth of the domain using an $n_r \times n_\theta \times n_\phi = 40 \times 16 \times 8$ mesh comprised of wedge and hexahedral elements. The results for various values of $k_z a$ are shown in Table 3 and compared against the values presented by Seybert, Wu, and Wu.³⁰ The results obtained with the conventional formulation are almost identical to the ones shown above and hence not shown again. The wedge/hexahedral mesh was deliberately chosen to be much coarser than the axisymmetric mesh to show that good results can be obtained even using a coarse mesh. Although the match with the results of Seybert, Wu, and Wu³⁰ is good at the lower frequencies, significant deviation at the higher frequencies occurs. I believe the reason for this deviation is that those researchers used a coarse mesh which does not capture the solution accurately at the higher frequencies; I have carried out a mesh refinement study and verified that the A9 results presented in Table 3 are close to the converged results. The accuracy of the results can also be improved further by using a mixed formulation³² for the structural analysis rather than the displacement-based formulation that has been used in generating the above results.

4.5. Cylinder with Hemispherical End Caps

I consider both radiation and scattering for a problem involving a cylinder with hemispherical end caps (see Fig. (8)).^{9,33,34} First I consider the radiation problem. The cylinder pulsates with a uniform normal velocity of unit magnitude over the entire surface. The dimensions used are $l = 3.5$, $r = 1$, and $R = 23.5$. For the radiation case, the fluid properties used are the same as in the pulsating sphere example. Symmetry con-

Table 3. Comparison of backscattered pressures at various distances when the hollow sphere is elastic; Bracketed values show the magnitude of the pressure.

$k_z a$	A9			W18/S27			$ P_{scat} ^{30}$
Surface backscattered pressure ($r = 1$)							
0.2	$-0.9437E-2 + 0.4911E-2i$	$(0.1064E-1)$	$-0.9462E-2 + 0.4917E-2i$	$(0.1066E-1)$	$0.1063E-1$		
0.4	$-0.4414E-1 + 0.1349E-1i$	$(0.4615E-1)$	$-0.4418E-1 + 0.1349E-1i$	$(0.4620E-1)$	$0.4606E-1$		
0.6	$-0.1452E0 + 0.2999E-1i$	$(0.1483E0)$	$-0.1447E0 + 0.3010E-1i$	$(0.1478E0)$	$0.1455E0$		
0.8	$-0.8658E0 + 0.8683E-1i$	$(0.8701E0)$	$-0.8425E0 + 0.8540E-1i$	$(0.8468E0)$	$0.7441E0$		
1.0	$0.6857E0 + 0.1250E0i$	$(0.6970E0)$	$0.6990E0 + 0.1256E0i$	$(0.7102E0)$	$0.7419E0$		
Backscattered pressure at $r = 3$							
0.2	$-0.3641E-3 + 0.5893E-3i$	$(0.6927E-3)$	$-0.3726E-3 + 0.5952E-3i$	$(0.7023E-3)$	$0.7039E-3$		
0.4	$-0.1571E-2 + 0.1700E-2i$	$(0.2315E-2)$	$-0.1583E-2 + 0.1739E-2i$	$(0.2352E-2)$	$0.2959E-3$		
0.6	$-0.6828E-2 + 0.4254E-2i$	$(0.8045E-2)$	$-0.6764E-2 + 0.4337E-2i$	$(0.8035E-2)$	$0.1118E-1$		
0.8	$-0.6228E-1 + 0.3689E-1i$	$(0.7238E-1)$	$-0.6039E-1 + 0.3599E-1i$	$(0.7030E-1)$	$0.6783E-1$		
1.0	$0.5645E-1 - 0.5132E-1i$	$(0.7629E-1)$	$0.5780E-1 - 0.5238E-1i$	$(0.7800E-1)$	$0.7248E-1$		
Backscattered pressure at $r = 10$							
0.2	$0.6466E-4 + 0.6618E-4i$	$(0.9253E-4)$	$0.6599E-4 + 0.6905E-4i$	$(0.9551E-4)$	$0.9751E-4$		
0.4	$0.1900E-3 - 0.1308E-3i$	$(0.2307E-3)$	$0.1983E-3 - 0.1407E-3i$	$(0.2432E-3)$	$0.5866E-3$		
0.6	$0.9077E-3 - 0.4914E-3i$	$(0.1032E-2)$	$0.8723E-3 - 0.4973E-3i$	$(0.1004E-2)$	$0.2597E-2$		
0.8	$-0.7941E-2 - 0.1353E-1i$	$(0.1569E-1)$	$-0.7698E-2 - 0.1309E-1i$	$(0.1519E-1)$	$0.1647E-1$		
1.0	$0.1315E-1 - 0.1402E-1i$	$(0.1922E-1)$	$0.1349E-1 - 0.1435E-1i$	$(0.1969E-1)$	$0.1698E-1$		

Table 4. Comparison of pressures at points A and B in the pulsating cylinder with hemispherical caps problem.

ω	B9		A9		B18/B27		W18/S27		Bhandakkar and Jog ⁹	
Pressure at A										
62.83	24.409	-4.899i	24.416	-4.902i	24.409	-4.899i	24.416	-4.902i	24.457	-4.917i
157.08	-36.716	-14.800i	-36.726	-14.797i	-36.716	-14.799i	-36.726	-14.797i	-36.391	-14.809i
318.03	11.010	+14.170i	10.968	+14.117i	11.010	+14.169i	10.968	+14.117i	11.13	+14.04i
475.66	-28.154	-27.635i	-28.251	-27.688i	-28.157	-27.633i	-28.251	-27.687i	-28.392	-27.061i
Pressure at B										
66.06	24.373	-9.955i	24.380	-9.959i	24.373	-9.955i	24.380	-9.959i	24.157	-8.035i
157.94	-55.500	-6.130i	-55.522	-6.121i	-55.500	-6.130i	-55.522	-6.121i	-55.622	-6.110i
315.38	36.407	-85.483i	35.938	-85.767i	36.407	-85.483i	35.938	-85.767i	36.002	-85.528i
472.26	76.511	+83.703i	80.274	+80.448i	76.511	+83.702i	80.274	+80.448i	79.592	+80.361i

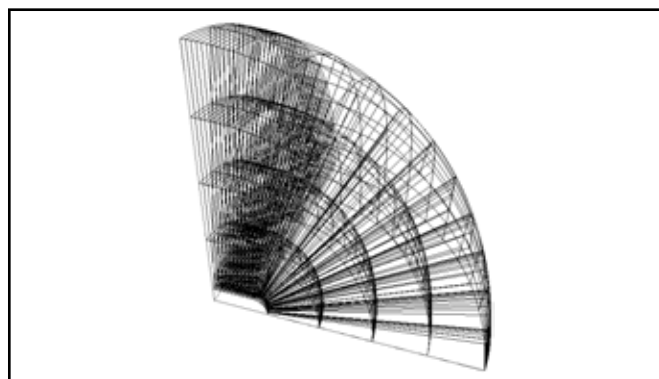


Figure 9. A typical mesh for the cylinder with hemispherical end caps problem; for clarity, fewer elements are shown in the radial direction than actually used.

considerations allow us to model one-eighth of the structure. A mesh of $n_r \times n_\theta \times n_\phi = 20 \times 20 \times 10$ (where ϕ is the circumferential direction) was used to model one-eighth of the structure as shown in Fig. (9). Solutions were also obtained using an axisymmetric mesh of $n_r \times n_\theta = 20 \times 20$ (roughly four elements per wavelength). The solutions at points A and B with coordinates $(0, 0, 10)$ and $(10, 0, 0)$, respectively, compared against the solutions in Bhandakkar and Jog,⁹ are presented in Table 4. Note that the solutions presented with our strategy are the raw nodal values, while the ones in Bhandakkar and Jog⁹ have been obtained using the Helmholtz integral equation. The proposed method yields a better approximation at point B at the highest frequency considered. The coarse mesh results obtained by using a $n_r \times n_\theta \times n_\phi = 8 \times 20 \times 10$ mesh and $R = 16.5$ are shown in Table 5, demonstrating the better accuracy of the proposed formulation, especially at higher frequencies.

Now I consider the scattering by the same cylinder of a plane wave that is incident along the x -axis and given by $e^{ik_x x}$. The fluid properties used are $\rho_f = 1026 \text{ kg/m}^3$ and $c = 1500 \text{ m/s}$.

Table 5. Comparison of coarse-mesh pressures at point A in the pulsating cylinder with hemispherical caps problem.

ω	B18/B27		W18/S27		Bhandakkar and Jog ⁹	
62.83	24.459	-5.036i	24.498	-5.055i	24.457	-4.917i
157.08	-37.052	-14.795i	-37.139	-14.755i	-36.391	-14.809i
318.03	10.606	+14.704i	10.916	+13.988i	11.13	+14.04i
475.66	-22.997	-31.793i	-28.839	-27.975i	-28.392	-27.061i

Table 6. Comparison of scattered pressures at points B and C in the cylinder with hemispherical caps problem; Bracketed values show the magnitude of the pressure.

$k_x a$	B18/B27			W18/S27		
Pressure at B						
1.5	$1.809E-2 + 0.161i$	(0.162)	$2.721E-2 + 0.160i$	(0.162)		
2.25	$-4.177E-2 + 0.232i$	(0.235)	$3.831E-2 + 0.242i$	(0.245)		
3	-0.109	$-0.242i$	-0.265	$-0.266i$	(0.268)	
Pressure at C						
1.5	-0.187	$+0.122i$	(0.223)	$-0.181 + 0.131i$	(0.223)	
2.25	$6.994E-2 + 0.337i$	(0.344)	$0.182 + 0.313i$	(0.361)		
3	-0.122	$+0.273i$	(0.299)	$0.463 - 0.185i$	(0.498)	

The discretization used is similar to that in the radiation case, with a mesh of $n_r \times n_\theta \times n_\phi = 20 \times 20 \times 20$ used to mesh one-fourth of the domain. The results for the forward and backscattered pressures at points B and C with coordinates $(10, 0, 0)$ and $(-10, 0, 0)$, respectively, are presented in Table 6 ($a = 1$), and when compared against Fig. (12) of Chen and Liu,³⁴ again show the high accuracy of the proposed formulation.

4.6. Vibrating Circular Piston in a Baffle

A circular piston of radius $a = 10$ centred at the origin vibrates with a normal velocity v_n . The analytical expression for the pressure field³⁵ at a point $(0, 0, z)$ along the axis is given by

$$\tilde{p} = \rho_f c v_n \left(e^{-ik\sqrt{a^2+z^2}} - e^{-ikz} \right).$$

The properties used are $\rho_f = 1.2$ and $c = 341$. The variables v_n and R were chosen to be 1 and 50, respectively. A uniform mesh of $n_r \times n_\theta = 40 \times 32$ axisymmetric elements

Table 7. Comparison of surface and far-field pressures along the axis for the circular piston example.

ka	B6/B9	B6/B9/A9	Analytical
		Pressure at $z = 0$	
1	188.109 +344.338i	188.109 +344.338i	188.108 +344.330i
5	293.389 -391.894i	293.413 -391.924i	293.125 -392.392i
10	761.414 -217.362i	762.958 -215.072i	752.548 -222.613i
		Pressure at $z = 50$	
1	-38.206 +13.090i	-38.206 +13.090i	-38.222 +13.397i
5	22.840 +198.795i	23.12 +198.831i	22.972 +199.211i
10	68.789 +380.338i	85.709 +376.840i	88.500 +378.631i

was used to discretize the domain with conventional triangular six-noded elements, denoted by B6, used in the layer closest to the origin. I use conventional elements up to $r_1 = 10$, and the proposed elements beyond r_1 and the results are compared against a mesh comprised of conventional elements alone; see Table 7. Not surprisingly, the near-field accuracy is almost the same, while the far-field accuracy is better with the proposed formulation.

To show that good far-field results are obtained even at high frequencies, I take $R = 80$ and $ka = 8\pi$, with the other properties the same as above. A uniform mesh of $n_r \times n_\theta = 120 \times 64$ axisymmetric elements is used to discretize the domain. In order to compare the results with Fig. (7.4.2) of Kinsler et al.,²⁸ one must normalize the pressures by a factor of $2\rho_f cv_n$. The results are shown in Fig. (10). From the plot of the absolute pressure, it may appear that the errors in the conventional formulation are small. However, in reality, the significant errors in the real and the imaginary parts of the conventional formulation, especially in the far field, cancel each other as seen from the plot for the real value of the pressure.

5. CONCLUSIONS

A finite element method has been proposed for exterior acoustic problems that favours outgoing waves and hence provides higher accuracy both in the near and far-field compared to other methods based on absorbing boundary conditions. The computational domain and input data are the same as for the conventional method (i.e., no extra variables are introduced). In addition, the cost of constructing the element stiffness matrix is also almost the same. Although the resulting global matrix as given in Eq. (24) is unsymmetric, it is sparse so that the computational cost is not increased significantly. The proposed elements, similar to standard finite elements, are based on Cartesian coordinates, use standard Gaussian quadrature and Lagrange interpolations, and, hence barring a few situations, can be used even in the direct vicinity of the radiator or scatterer, thereby circumventing the need of using an inner mesh of conventional elements. The method is similar to the PML method in that each layer surrounding the radiator or scatterer absorbs acoustic radiation so that no boundary condition on the truncated boundary needs to be imposed.

Bibliography

¹ Givoli, D. Non-reflecting boundary conditions, *Journal of Computational Physics*, **94**, 1–29, (1991).
² Qi, Q. and Geers, T. L. Evaluation of the perfectly matched

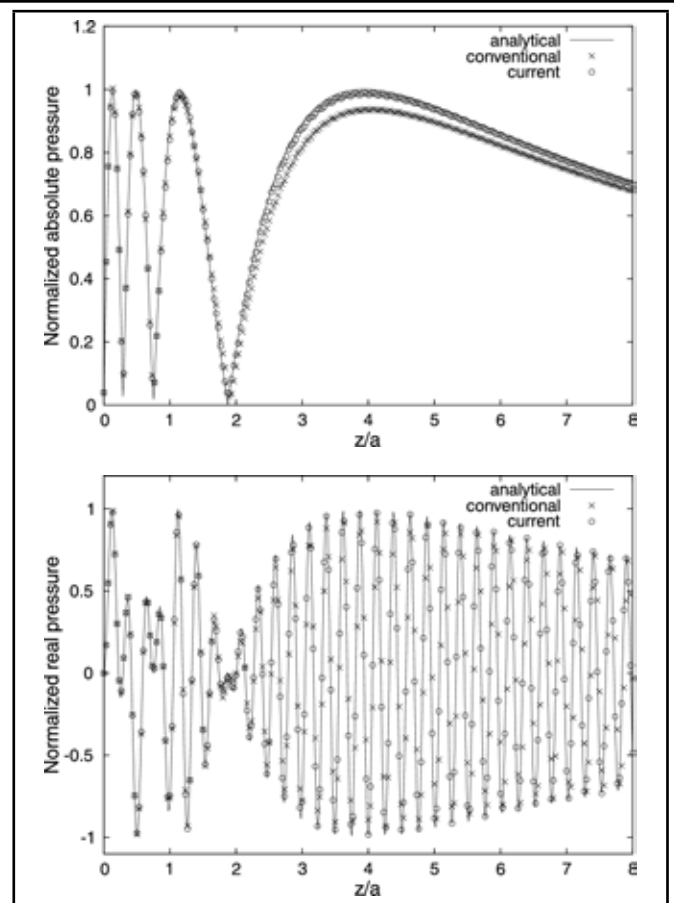


Figure 10. Comparison of the numerically and analytically obtained normalized pressures $|\bar{p}|/(2\rho_f cv_n)$ and $\bar{p}_r/(2\rho_f cv_n)$ along the axis of the piston as a function of z/a for $ka = 8\pi$.

layer for computational acoustics, *Journal of Computational Physics*, **139**, 166–183, (1998).

³ Burnett, D. S. A three-dimensional acoustic infinite element based on a prolate spheroidal multipole expansion, *Journal of the Acoustical Society of America*, **96** (5), 2798–2816, (1994).
⁴ Burnett, D. S. and Holford, R. L. Prolate and oblate spheroidal acoustic infinite elements, *Computer Methods in Applied Mechanics and Engineering*, **158**, 117–142, (1998).
⁵ Burnett, D. S. and Holford, R. L. An ellipsoidal acoustic infinite element, *Computer Methods in Applied Mechanics and Engineering*, **164**, 49–76, (1998).
⁶ Gerdes, K. A review of infinite element methods for exterior Helmholtz problems, *Journal of Computational Acoustics*, **8** (1), 43–62, (2000).
⁷ Astley, R. J. Infinite elements for wave problems: a review of current formulations and an assessment of accuracy, *International Journal for Numerical Methods in Engineering*, **49**, 951–976, (2000).
⁸ Astley, R. J. and Coyette, J. P. The performance of spheroidal infinite elements, *International Journal for Numerical Methods in Engineering*, **52**, 1379–1396, (2001).

- ⁹ Bhandakkar, T. K. and Jog, C. S. An alternative implementation of the Burnett family of acoustic finite elements, *Journal of the Acoustical Society of America*, **118** (4), 2295–2301, (2005).
- ¹⁰ Dreyer, D. and Estorff, O. Improved conditioning of infinite elements for exterior acoustics, *International Journal for Numerical Methods in Engineering*, **58**, 933–953, (2003).
- ¹¹ Harari, I. A survey of finite element methods for time-harmonic acoustics, *Computer Methods in Applied Mechanics and Engineering*, **195**, 1594–1607, (2006).
- ¹² Shirron, J. J. and Giddings, T. E. A finite element model for acoustic scattering from objects near a fluid-fluid interface, *Computer Methods in Applied Mechanics and Engineering*, **196**, 279–288, (2006).
- ¹³ Huttunen, T. H., Kaipio, J. P., and Monk, P. The perfectly matched layer for the ultra weak variational formulation of the 3D Helmholtz equation, *International Journal for Numerical Methods in Engineering*, **61**, 1072–1092, (2004).
- ¹⁴ Bayliss, A. and Turkel, E. Radiation boundary conditions for wave-like equations, *Comm. Pure and Appl. Math.*, **XXXIII**, 707–725, (1980).
- ¹⁵ Astley, R. J. Infinite elements, In Marburg, S. and Nolte, B. Editors, *Computational acoustics of noise propagation in fluids*, Springer, (2008).
- ¹⁶ Atkinson, F. V. On Sommerfeld's radiation condition, *Philosophical Magazine*, **40**, 645–651, (1949).
- ¹⁷ Astley, R. J. Wave envelope and infinite elements for acoustical radiation, *International Journal for Numerical Methods in Fluids*, **3**, 507–526, (1983).
- ¹⁸ Astley, R. J. and Eversman, W. Finite element formulations for acoustical radiation, *Journal of Sound and Vibration*, **88**, 47–64, (1983).
- ¹⁹ Astley, R. J., Macaulay, G. J., and Coyette J. P. Mapped wave envelope elements for acoustical radiation and scattering, *Journal of Sound and Vibration*, **170**, 97–118, (1994).
- ²⁰ Astley, R. J., Macaulay, G. J., Coyette, J. P., and Cremers L. Three-dimensional wave-envelope elements of variable order for acoustic radiation and scattering. Part I. Formulation in the frequency domain, *Journal of the Acoustical Society of America*, **103** (1), 49–63, (1998).
- ²¹ Shirron, J. J. and Dey, S. Acoustic infinite elements for non-separable geometries, *Computer Methods in Applied Mechanics and Engineering*, **191**, 4123–4139, (2002).
- ²² Bossut, R. and Decarpigny, J. N. Finite element modeling of radiating structures using dipolar damping element, *Journal of the Acoustical Society of America*, **86** (4), 1234–1244, (1989).
- ²³ Bettess, P. and Chadwick, E. Wave envelope examples for progressive waves, *International Journal for Numerical Methods in Engineering*, **38** (15), 2487–2508, (1995).
- ²⁴ Cremers, L. and Fyfe, K. R. On the use of variable order infinite wave envelope elements for acoustic radiation and scattering, *Journal of the Acoustical Society of America*, **97** (4), 2028–2040, (1995).
- ²⁵ Everstine, G. C. Finite element formulations of structural acoustic problems, *Computers and Structures*, **65** (3), 307–321, (1997).
- ²⁶ Gupta, A. WSMP: Watson Sparse Matrix Package Part II—direct solution of general sparse systems, *IBM Research Report RC 21888 (98472)*, (2000).
- ²⁷ Gupta, A. Recent advances in direct methods for solving unsymmetric sparse systems of linear equations, *ACM Transactions on Mathematical Software*, **28** (3), 301–324, (2002).
- ²⁸ Kinsler, L. E., Fray, A. R., Coppens, A. B., and Sanders, J. V. *Fundamentals of acoustics*, John Wiley and Sons, New York, (2000).
- ²⁹ Malecki, I. *Physical foundations of technical acoustics*, Permagon Press, Warszawa, (1969).
- ³⁰ Seybert, A. F., Wu, T. W., and Wu, X. F. Radiation and scattering of acoustic waves from elastic solids and shells using the boundary element method, *Journal of the Acoustical Society of America*, **84** (5), 1906–1912, (1988).
- ³¹ Junger, M. C. and Feit, D. *Sound, structure, and their interactions*, MIT Press, Cambridge, (1972).
- ³² Jog, C. S. Improved hybrid elements for structural analysis, *Journal of the Mechanics and Materials of Structures*, **5** (3), 507–528, (2010).
- ³³ Li, S. and Huang, Q. An improved form of the hypersingular boundary integral equation for exterior acoustic problems, *Engineering Analysis and Boundary Elements*, **34**, 189–195, (2010).
- ³⁴ Chen, S. H. and Liu, Y. J. A unified boundary element method for the analysis of sound and shell-like structure interactions. I. Formulation and verification, *Journal of the Acoustical Society of America*, **106** (3), 1247–1254, (1999).
- ³⁵ Skudrzyk, E. *The foundations of acoustics*, Springer-Verlag, New York, (1971).

The Prediction of Nonlinear Responses and Active Stiffness Control of Moving Slender Continua Subjected to Dynamic Loadings in a Vertical Host Structure

Stefan Kaczmarczyk and Philip Picton

School of Science and Technology, The University of Northampton, St. George's Avenue, Northampton, NN2 6JD, UK

(Received 21 December 2011, accepted 14 September 2012)

Slender continua such as long ropes, cables, and belts are used as tension and payload-carrying members in various engineering applications. They are deployed in terrestrial mine/underground equipment and high-rise building installations through to tethered offshore tension members, tethered space satellite systems and rotating momentum-exchange tethers in Earth's orbit. The slender continua are inherently nonlinear, leading to large nonlinear responses with passages through resonances taking place when the time-varying natural frequencies of the system approach the frequency of the inertial load resulting from the dynamic loadings. In this paper, the lateral nonlinear dynamic behaviour of long slender continua moving at speed in a tall host structures is analysed. A mathematical model comprising non-stationary, nonlinear ordinary differential equations is used to describe the dynamic behaviour of the system equipped with a multi-modal active stiffness controller. The active control is implemented by an axial motion of the support, which results in substantial reduction of the response.

1. INTRODUCTION

Moving continuous tensioned slender structural elements, such as ropes, cables, belts, and tethers, are pivotal components of many engineering systems. The applications include crane and mine hoists, offshore and marine installations, vertical transportation systems in buildings, and space tether propulsion systems. Due to their relatively low weight, flexibility, and low internal damping, these continua often vibrate at large amplitudes and exhibit a broad range of complex nonlinear dynamic phenomena.

The dynamic behaviour of systems with moving tensioned members has attracted considerable attention. Numerous aspects of their dynamic response characteristics in transport installations, in particular in building elevators, mine hoists and space systems, have been studied.¹⁻⁵ A broad range of sources of excitation are present in such systems. These include transient loads as well as periodic forces. The excitations produced by earthquakes and high winds may lead to adverse dynamic behaviour of these tension members installed in large civil structures and tall buildings. Substantial research in the area of rope and cable dynamics has been devoted to the issue of mitigating the effects of their dynamic responses. Various control techniques have been developed to suppress their lateral response, mainly for use in cable civil structures such as suspended bridges and cable-stayed bridges. Passive methods involve the application of viscous dampers placed near the cable support and acting in a lateral direction.⁶ Semi-active control strategies include the application of magnetorheological dampers that achieve significant vibration reduction compared to viscous dampers.⁷ Active vibration control methods using boundary lateral motion^{8,9} or longitudinal motion¹⁰⁻¹³

have also been considered. The latter strategy utilizes the fact that the longitudinal elastic stretching of the slender element is coupled with its lateral motion. An actuator is used to produce a longitudinal oscillatory motion of the support in order to cause the time variation of transverse (lateral) stiffness which in turn results in extracting energy from the system. Such an active control method is termed "active stiffness control."

The aim of this paper is to develop a mathematical model to predict the dynamic behaviour of long slender continua deployed in tall host structures. The objectives include to determine the dynamic responses when these continua are subjected to harmonic excitation due to a low-frequency sway of the host structure and to investigate the effectiveness of a suitable strategy to control the effects of the sway. Active stiffness control is considered to mitigate the effects of passage through resonances when a slender continuum, such as a wire rope or cable, moves at speed and comes to rest, exhibiting large dynamic displacements.

2. VIBRATION MODEL AND CONTROL STRATEGY

The planar model of a slender element, representing a rope or cable and modelled as a taut string of time-varying length $L(t)$ moving at speed in a vertical cantilevered host structure, is depicted in Fig. (1). The element has mass per unit length m , elastic modulus E , and an effective cross-sectional area A . It is wrapped around a drum at the bottom end with its upper end attached to a support moving at speed $v(t)$, while the host structure is subjected to bending deformations described by the shape function $\Psi(z)$, with z denoting a coordinate measured from ground level. The bending deformations produce a har-

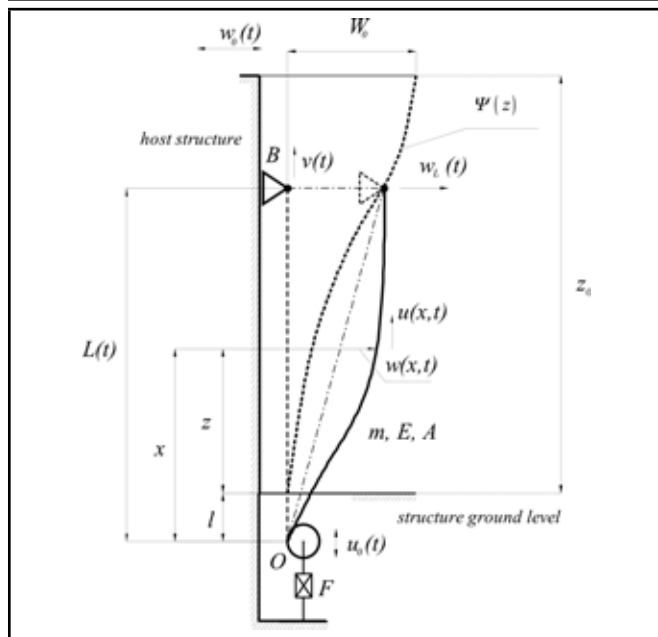


Figure 1. Slender element moving in a vertical host structure.

monic motion $w_0(t)$ of frequency Ω and amplitude W_0 measured at the level defined by the coordinate z_0 . The system is equipped with the actuator F acting on the drum assembly, which produces an axial motion $u_0(t)$ according to a suitable feedback-control strategy in order to achieve the active stiffness control.

The bending motions (sway) of the structure result in an inertial dynamic load acting upon the element and its dynamic response is represented by the lateral displacements denoted as $w(x, t)$, where x is measured from the origin O placed at distance l below ground level. The lateral response $w(x, t)$ is coupled with axial (longitudinal) motions that are denoted as $u(x, t)$. It is assumed that the motion of the host structure is not influenced by the response of the slender element. Thus, in the model used in this work, the excitation is treated as a kinematic ideal excitation with the swaying structure being treated as an ideal source of energy.¹⁴ For practical applications involving modelling interactions between tall building structures and slender components, such as ropes and cables employed in vertical transportation systems, this is an acceptable simplification.

2.1. Vibration Model

The mean tension of the element is expressed as

$$T_m(x, t) = T_0 + mx[g + a(t)]; \tag{1}$$

where T_0 represents a constant tension term, $a(t) = \dot{v}(t)$ is the acceleration of the upper support (an overdot denotes the time derivative) and g is the acceleration of gravity. The axial Green's strain measure due to stretching of the element is given as¹⁵

$$\varepsilon = u_x + \frac{1}{2}w_x^2; \tag{2}$$

where $(\)_x \equiv \frac{\partial(\)}{\partial x}$. The equations governing the undamped dynamic displacements $u(x, t)$ and $w(x, t)$ can be developed

by applying Hamilton's principle, which yields

$$m \frac{d^2u}{dt^2} - EA\varepsilon_x - ma(t) = 0; \tag{3}$$

$$m \frac{d^2w}{dt^2} - [T_0 + m(g + a(t))x]w_{xx} + m(g + a(t))w_x - EA(\varepsilon w_x)_x = 0; \tag{4}$$

where

$$\frac{d^2(\)}{dt^2} = (\)_{tt} + 2v(\)_{xt} + v^2(\)_{xx} + a(\)_x \tag{5}$$

and $(\)_t \equiv \frac{\partial(\)}{\partial t}$. For tensioned members, such as wire ropes and metallic cables, the lateral frequencies are much lower than the longitudinal frequencies. For tall structures, such as high-rise towers and buildings, the bending motion frequencies Ω are much smaller than the fundamental longitudinal frequencies of the element, and we can assume that no interaction will take place between the lateral modes and the longitudinal modes. Thus, the longitudinal inertia of the element can be neglected in Eq. (3) so that the model is reduced to one equation only.¹⁶ This leads to the following equation for the lateral response:

$$mw_{tt} - \left\{ T_0 + m \left[\frac{1}{2}a(t)L(t) - v^2(t) + gx \right] + \frac{EA}{L(t)} \left[\frac{1}{2} \int_0^{L(t)} w_x^2 dx + u_0(t) \right] \right\} w_{xx} + m[a(t) - g]w_x + 2mv(t)w_{xt} = 0; \tag{6}$$

where the spatial coordinate x is defined in a time-variant domain $0 < x < L(t)$. The lateral displacements at the boundaries are defined as

$$w(0, t) = 0; \quad w[L(t), t] = w_L(t); \tag{7}$$

where $w_L(t)$ represents lateral displacements of the structure corresponding to the upper end of the element (see Fig. (1)). In order to accommodate the excitation in the equation of motion (Eq. 6)) the overall lateral displacements of the rope are expressed as

$$w(x, t) = \bar{w}(x, t) + \frac{x}{L(t)}w_L(t); \quad 0 \leq x \leq L(t); \tag{8}$$

where $\bar{w}(x, t)$ are the displacements relative to the stretched configuration of the element. In this analysis, the deformation shape function $\Psi(z)$ is assumed to be related to the fundamental mode of the host structure and is approximated by a cubic polynomial as follows:

$$\Psi(z) = 3\left(\frac{z}{z_0}\right)^2 - 2\left(\frac{z}{z_0}\right)^3 \tag{9}$$

so that the lateral displacement at $x = L$ can be expressed as

$$w_L(t) = \Psi_L w_0(t); \tag{10}$$

where

$$\Psi_L = 3\left(\frac{L(t) - l}{z_0}\right)^2 - 2\left(\frac{L(t) - l}{z_0}\right)^3 \tag{11}$$

and $l = L(0)$.

Using the transformation in Eq. (8) in Eq. (6), an approximate solution to the nonlinear partial differential equation of motion is sought by using the Galerkin method with the following finite series:

$$\bar{w}(x, t) = \sum_{n=1}^N \Phi_n [x; L(t)] q_n(t); \quad (12)$$

where $\Phi_n [x; L(t)] = \sin \frac{n\pi}{L(t)} x$; $n = 1, 2, \dots, N$; with N denoting the number of modes, are the natural vibration modes of the corresponding taut string of length $L = L(t)$ with the tension given as

$$T(t) = T_0 + \frac{1}{2} m a(t) L(t); \quad (13)$$

and $q_n(t)$; $n = 1, 2, \dots, N$ represent the modal displacements. This results in the following set of N ordinary differential equations:

$$\begin{aligned} & \ddot{q}_r(t) + 2\zeta_r \omega_r(t) \dot{q}_r(t) + \\ & + \lambda_r^2(t) \left\{ \bar{c}^2(t) - v^2(t) + c^2 \left[\frac{1}{2} \left(\frac{w_L(t)}{L(t)} \right)^2 + \frac{u_0(t)}{L(t)} \right] \right\} q_r(t) + \\ & + \sum_{n=1}^N K_{rn}(t) q_n(t) + \sum_{n=1}^N C_{rn}(t) \dot{q}_n(t) + \\ & + \left(\frac{\lambda_r(t)}{2} c \right)^2 q_r(t) \sum_{n=1}^N \lambda_n^2(t) q_n^2(t) = Q_r(t); \\ & r = 1, 2, \dots, N; \quad (14) \end{aligned}$$

where cubic nonlinearities arising due to the effect of rope stretching are present; the modal damping represented by the ratios ζ_r has been added; $\omega_r(t)$; $r = 1, 2, \dots, N$ are the undamped time-varying natural frequencies of the element; $\bar{c}(t) = \sqrt{\frac{T(t)}{m}}$ and $c = \sqrt{\frac{EA}{m}}$ represent the lateral wave speed and the longitudinal wave speed, respectively; $\lambda_r(t) = \frac{r\pi}{L(t)}$; $K_{rn}(t)$; $C_{rn}(t)$ are time-variant coefficients; and $Q_r(t)$ is the modal excitation given as

$$K_{rn}(t) = \begin{cases} \frac{r^2 \pi^2}{4}, & n = r \\ \frac{2g}{L(t)} \left\{ \left[\left(\frac{a(t)}{g} - 1 \right) \frac{nr}{n^2 - r^2} + \frac{2rn^3}{(n^2 - r^2)^2} \right] [(-1)^{r+n} - 1] \right\}, & n \neq r \end{cases}; \quad (15)$$

$$C_{rn}(t) = \frac{4v(t)}{L(t)} \begin{cases} 0, & n = r \\ \frac{nr}{n^2 - r^2} [(-1)^{r+n} - 1], & n \neq r \end{cases}; \quad (16)$$

$$Q_r(t) = \frac{2}{r\pi L(t)} \left\{ \begin{aligned} & (-1)^r L(t) \ddot{w}_L(t) + \\ & - \left[(g - a(t)) w_L(t) + \right. \\ & \left. - 2v(t) \dot{w}_L(t) \right] [(-1)^r - 1] \end{aligned} \right\}. \quad (17)$$

It is also evident that the host structure motion $w_L(t)$ appears in Eq. (14) together with the axial motion $u_0(t)$ applied at the lower boundary as parametric excitation terms.

2.2. Control Strategy

A feedback control algorithm is needed to achieve active stiffness control. For example, a non-collocated control strategy based on the measurements of the response expressed as

$$u_0(t) = \Phi [\mathbf{q}(t), \dot{\mathbf{q}}(t)]; \quad (18)$$

where Φ represents a suitable control law and \mathbf{q} and $\dot{\mathbf{q}}$ denote the modal displacement vector and the modal velocity vector, respectively, can be considered. The feasibility of the active stiffness control of ropes and cables based on various non-collocated feedback control has been studied extensively. In particular, the implementation of feedback control in terms of vibration modes has been investigated by many researchers. In the modal control law proposed by Chen,¹⁰ the feedback for axial support motion is given as

$$u_0(t) = \frac{a_u}{\omega_r} \frac{q_r \dot{q}_r}{|q_r|}; \quad (19)$$

where a_u is the control gain. In the event of primary resonance, when the frequency of the excitation Ω is near the natural frequency ω_r , this control algorithm results in the axial motion at a frequency equal to twice the natural frequency of the rope (at the parametric resonance; $2\omega_r$) with the phase shift of the control motion relative to the response of the system equal to $\frac{\pi}{2}$ (which is achieved by the product of the modal displacement and the modal velocity). Fujino, Warnitchai, and Pacheco¹¹ developed Chen's concept further and proposed the following feedback control law:

$$u_0(t) = \frac{2a_u}{\omega_r} \frac{q_r \dot{q}_r}{q_r^2 + \left(\frac{\dot{q}_r}{\omega_r} \right)^2}. \quad (20)$$

The algorithms of Eqs. (19) and (20) are single-mode controllers. They are effective in suppressing the target mode. However, control spillover might occur when the uncontrolled modes are excited to some degree by the active control system. This effect might have a detrimental influence on the performance of the system. In order to address this issue Achkire, Bossens, and Preumont applied a collocated control strategy with positive integral force feedback.¹² However, Wang and Xu demonstrated that multimode feedback for the axial motion can be used in active stiffness control.¹³ In such a control strategy, the modal spillover phenomenon can be avoided. In this study, a multimode feedback law was applied. This law accommodates all modes involved in series (12) and is given as

$$u_0(t) = a_u \frac{\sum_{n=1}^N q_n \dot{q}_n}{\sum_{n=1}^N \omega_n^2 q_n^2}. \quad (21)$$

3. CASE STUDY

The dynamic performance of the system comprising a steel wire rope of mass per unit length $m = 1.3 \text{ kg/m}$, having the modulus of elasticity $E = 0.7 \times 10^5 \text{ N/mm}^2$ and an effective cross-sectional area $A = 148 \text{ mm}^2$, is considered. The modal damping ratios of 0.3% are used across all modes.¹² The rope is being accelerated from rest when its initial length is $l = 3.75 \text{ m}$, at the rate of 1.2 m/s^2 and is moving upwards at

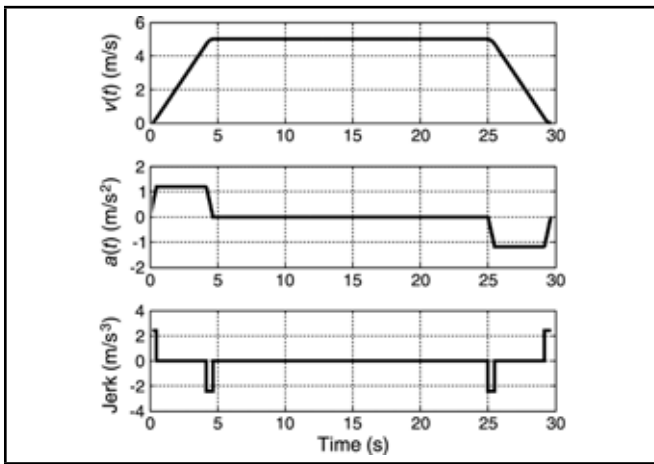


Figure 2. Velocity, acceleration, and jerk time profile.

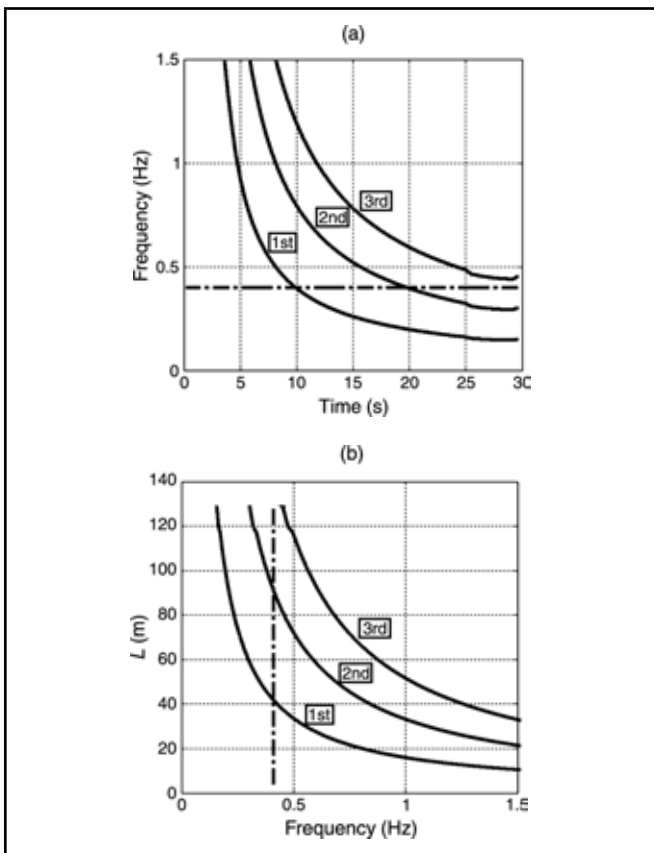


Figure 3. Variations of the first three natural frequencies (a) versus time and (b) versus length of the rope together with the frequency of the excitation (dashed line).

a speed of 5 m/s, later being decelerated at the rate of 1.2 m/s² and coming to rest after 29.7 s, having reached the maximum length $L_{max} = 128.75$ m. The velocity, acceleration and jerk time profiles of the upper end of the rope are shown in Fig. (2).

The jerk value of 2.4 m/s³ has been applied to smooth the acceleration time profile.

The host structure is subjected to a harmonic motion of frequency 0.4 Hz ($\Omega = 2.513$ rad/s) and amplitude 0.25 m measured at $z_0 = 137.75$ m above the ground floor level. This results in an inertial load acting upon the rope during its travel and after it has reached its maximum length remaining stationary. In order to predict the dynamic response and to assess the

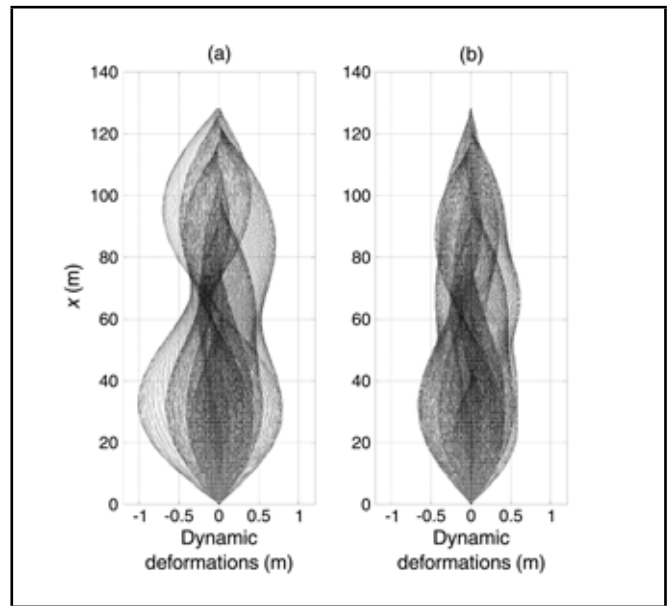


Figure 4. The dynamic operational shapes during travel: (a) without control and (b) with control.

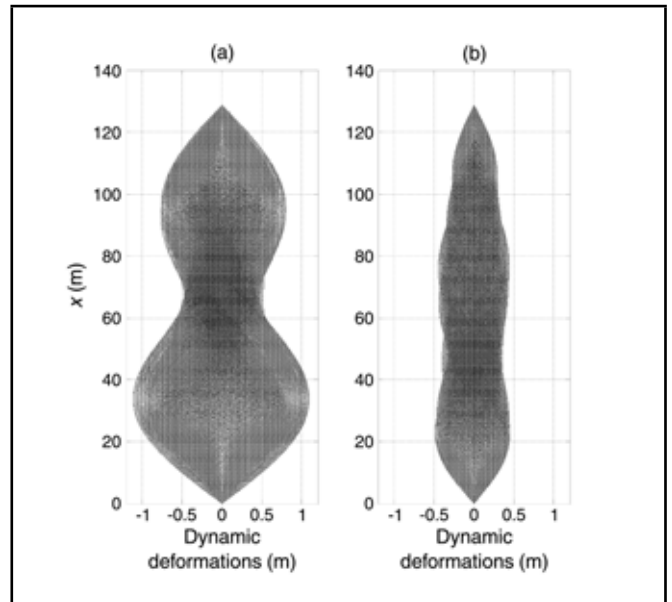


Figure 5. The dynamic operational shapes at rest: (a) without control and (b) with control.

performance of the controller, the equations of motion represented by Eq. (14) are integrated numerically using an explicit Runge-Kutta fourth- and fifth-order formula. The numerical procedure is started from the initial instant $t_0 = 0$ when the rope begins to move and is carried out until the final simulation time, chosen as $t_f = 120$ s. The results are shown in Figs. (3)–(9) and are discussed in the following sections.

The length variation of the rope results in changes of its mass and stiffness characteristics so that slow variations of the natural frequencies occur.² In addition, the natural frequencies are affected by the speed and acceleration of the transport motion. The variations of the first three natural frequencies versus time and length of the rope are shown in Figs. (3a) and (3b), respectively, together with the frequency of the excitation Ω (expressed in Hz and represented by a dashed line). The natural frequencies decrease as the length of the rope increases. After

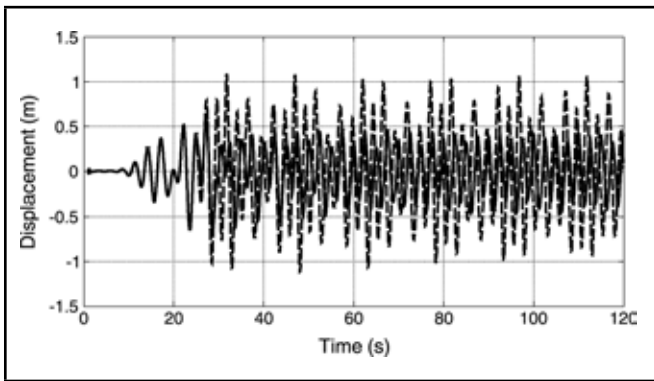


Figure 6. Vibrations (displacements) of the rope at quarter span without control (dashed line) and with active control (solid line).

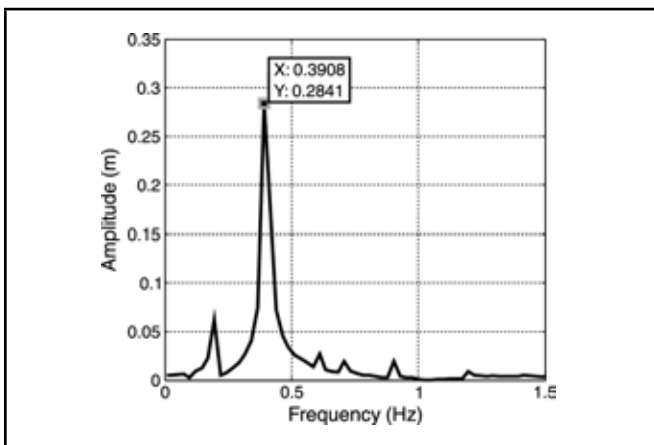


Figure 7. FFT frequency spectrum of the response $\bar{w}[L_{\max}/4, t]$ with active control corresponding to the time interval $t \in [60, 100]$ s.

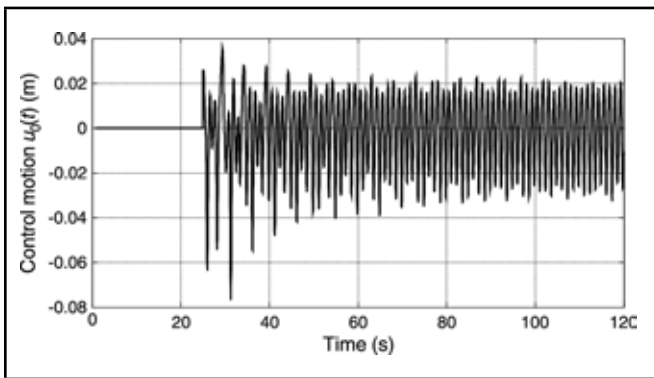


Figure 8. Control motion.

approximately 10 s, a passage through the fundamental resonance takes place when the rope reaches the length of 41.7 m, followed by the second mode resonance after 20 s corresponding to the length of 91 m.

The dynamic deformation (operational) shapes of the rope, without control and with the controller activated at the time instant $t = 25$ s with the gain a_u adjusted to 0.1, are presented in Figs. (4) and (5), during travel and when the system is stationary after the rope has been fully extended, respectively. As is evident from Fig. (4a), during the first stage of travel the deformation shapes reflect the fundamental mode character of the response, but after the second mode resonance takes place, the second-mode becomes dominant, with the rope subjected

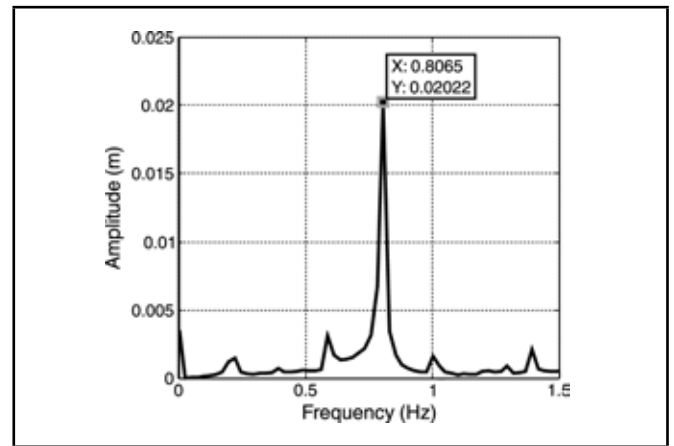


Figure 9. FFT frequency spectrum of the control motion corresponding to the time interval $t \in [60, 100]$ s.

to large amplitude vibrations. Large displacements and the influence of second mode resonance are evident from the operational shapes corresponding to the stage after the rope has reached its maximum length and the system is stationary, presented in Fig. (5a). The results presented in Figs. (4b) and (5b) show that the resonance motions are suppressed and the deformations of the rope are reduced.

The effect of the active stiffness control is demonstrated further in Fig. (6), where the corresponding combined time response plots representing the dynamic displacements of the rope $\bar{w}[L(t)/4, t]$ (during travel) and $\bar{w}[L_{\max}/4, t]$ (fully extended and stationary after 29.7 s) recorded at its quarter span versus time are shown. The results demonstrate that, without feedback control, large motions of the rope, with the amplitudes exceeding 1 m, occur. However, when the active control system is applied the response is reduced by about 50% (the displacements are less than 0.5 m after the rope reaches its maximum length and the system is at rest). The fast Fourier transformation (FFT) frequency spectrum of the response of the system with active control corresponding to the time interval $t \in [60, 100]$ s is shown in Fig. (7). The dominant frequency of the response is equal to the frequency of the sway excitation (0.4 Hz).

The axial control motion u_0 is plotted versus time and shown in Fig. (8). At the beginning, shortly after the control system is activated, the maximum displacement at the actuator end is approximately 7.5 cm. But after about 60 s from the start, the maximum peak amplitude is decreased to about 4 cm. The frequency spectrum of the control motion corresponding to the time interval $t \in [60, 100]$ s is shown in Fig. (9). The support motion has the dominant frequency equal to twice the frequency of the excitation (0.8 Hz).

4. CONCLUSIONS

The equations of motion of a slender continuum represented by a rope moving at speed within a tall host structure derived in this paper accommodate the nonlinear effects of rope stretching. This model is used to determine the response of the system under the load due to the sway of the host structure and to demonstrate the application of active stiffness control. Numerical simulation results show the effect of transient resonance conditions on the dynamic response of long slender continua

deployed in tall structures. The continua suffer from large lateral displacements that often exceed allowable limits. This issue often arises in many engineering systems. For example, in high-rise structures, traction drive elevator systems employ long ropes and cables, which results in the need to predict and control flexible low-frequency modes and nonlinear, non-stationary dynamic phenomena.

The active stiffness control system proposed in this work facilitates extracting energy from the vibrating slender continua, moving at speed and then being stationary in the host structure, through dynamic axial motion implemented at the support. It has been demonstrated by means of a case study that the active stiffness control of the lateral response can substantially reduce the response and the effects of passage through primary resonances. A relatively small amplitude of the axial motion is required to achieve the active stiffness control.

However, it should be noted that the axial motion at the boundary may either generate or dissipate energy, depending on the phase shift angle between the control signal and the response. For the control to be effective, the control law, such as given by Eq. (21), must be strictly observed. Otherwise, the axial motion may act as parametric excitation leading to energy generation and instability in the system.

ACKNOWLEDGMENTS

Support received from ThyssenKrupp Elevator Corporation for the research work reported in this paper is gratefully acknowledged.

Bibliography

- ¹ Chi, R. M. and Shu, H. T. Longitudinal vibration of a hoist rope coupled with the vertical vibration of an elevator car, *Journal of Sound and Vibration*, **148**, 154–159, (1991).
- ² Kaczmarczyk, S. The passage through resonance in a catenary-vertical cable hoisting system with slowly varying Length, *Journal of Sound and Vibration*, **208**, 243–269, (1997).
- ³ Ziegler, S. W. and Cartmell, M. P. Using motorised tethers for payload orbital transfer, *AIAA Journal of Spacecraft and Rockets*, **38** (6), 904–913, (2001).
- ⁴ Terumichi, Y., Kaczmarczyk, S., Turner, S., Yoshizawa, M., and Ostachowicz, W. Modelling, simulation and analysis techniques in the prediction of non-stationary vibration response of hoist ropes in lift systems, *Materials Science Forum*, **440–441**, 497–504, (2003).
- ⁵ Salamaliki-Simpson, R., Kaczmarczyk, S., Picton, P., and Turner S. Non-linear modal interactions in a suspension rope system with time-varying length, *Applied Mechanics and Materials*, **5–6**, 217–224, (2006).
- ⁶ Chen, S., Darivandi, N., and Ghrib, F. The design of an optimal viscous damper for a bridge stay cable using energy-based approach, *Journal of Sound and Vibration*, **296**, 4689–4704, (2010).
- ⁷ Zhou, Q., Nielsen, S. R. K., and Qu W. L. Semi-active control of three-dimensional vibrations of an inclined sag cable with magnetorheological dampers, *Journal of Sound and Vibration*, **329**, 1–22, (2006).
- ⁸ Baicu, C. F., Rahn, C. D., and Nibali, B. D. Active boundary control of elastic cables: theory and experiment, *Journal of Sound and Vibration*, **198**, 17–26, (1996).
- ⁹ Fung, R. F., Wu, J. W., and Wu, S. L. Exponential stabilization of an axially moving string by linear boundary feedback, *Automatica*, **35**, 177–181, (1999).
- ¹⁰ Chen, J. C. Response of large space structures with stiffness control, *Journal of Spacecraft and Rockets*, **21**, 463–467, (1984).
- ¹¹ Fujino, Y., Warnitchai, P., and Pacheco, B. M. Active stiffness control of cable vibration, *Trans. ASME Journal of Applied Mechanics*, **60**, 948–953, (1993).
- ¹² Achkire, Y., Bossens, F., and Preumont, A. Active damping and flutter control of cable-stayed bridges, *Journal of Wind Engineering and Industrial Aerodynamics*, **74–76**, 913–821, (1998).
- ¹³ Wang, L. Y. and Xu, Y. L. Active stiffness control of wind-rain induced vibration of prototype stay cable, *International Journal for Numerical Methods in Engineering*, **74**, 80–100, (2008).
- ¹⁴ Nayfeh, A. H. and Mook, D. T. *Nonlinear Oscillations*, John Wiley & Sons, New York, (1979).
- ¹⁵ Kaczmarczyk, S. and Ostachowicz, W. Transient vibration phenomena in deep mine hoisting cables. Part 1: mathematical model, *Journal of Sound and Vibration*, **262** (2), 219–244, (2003).
- ¹⁶ Nayfeh, A. H. and Pai, P. F. *Linear and Nonlinear Structural Mechanics*, John Wiley & Sons, Hoboken, New Jersey, (2004).

Sinem Öztürk was born in Istanbul, Turkey, in 1982. She received BSc and MSc degrees in mechanical engineering at Istanbul Technical University, Istanbul, Turkey, in 2005 and 2008, respectively. Since 2008, she has been pursuing a PhD degree at Istanbul Technical University. In 2007, she joined the Division of Machine Theory and Systems Dynamics and Control (MT&SDC) Group of the Department of Mechanical Engineering, Istanbul Technical University, as a research assistant. Her current research interests include theory of machines, mechanical vibrations, modal testing, engineering acoustics, dynamics of mechanical systems, and noise and vibration control. She is a fellow of the Turkish Chamber of Mechanical Engineers.



Haluk Erol is Professor of Mechanical Engineering at the Istanbul Technical University. Dr. Erol teaches machine theory, mechanical vibrations, engineering acoustics, and noise and vibration control courses. His research areas are in parallel to his courses: machine dynamics and industrial noise and vibration control. Dr. Erol is involved in research and development projects and has directed graduate studies and industrial application projects. He works mainly on the industrial applications of noise and vibration control, and he has been a consultant to more than 25 industrial clients. He is also the author of numerous articles in professional and academic journals.

Sudib K. Mishra was born in 1981. He is currently Assistant Professor at the Indian Institute of Technology, Kanpur, UP, India. Dr. Mishra obtained his bachelor's degree in civil engineering from the Bengal Engineering College, his Master's in structural engineering from the Indian Institute of Technology, Bombay, India, and PhD from the University of Arizona, Tucson, USA, majoring in engineering mechanics. He was a postdoctoral associate in the Department of Mechanical and Aerospace Engineering at the University of California, Irvine, USA. Dr. Mishra's research interests include multiscale multiphysics modelling, passive control systems, optimization, structural stability, and reliability analysis.



Subrata Chakraborty was born in 1969 and is currently a professor at the Bengal Engineering and Science University, Shibpur, India. He is a fellow of the Indian National Academy Engineering and the Institution of Engineers (India). Dr. Chakraborty completed his bachelor's degree in civil engineering from Bengal Engineering College of Calcutta University in 1991 and master's in technology and PhD in civil engineering with structural engineering specialization from the Indian Institute of Technology Kharagpur in 1993 and 1997, respectively. He was a postdoctoral researcher at University of Cambridge, United Kingdom, University of Arizona, USA, and Technical University of Aachen, Germany. In general, Prof. Chakraborty's research interests include the field of stochastic finite element method, stochastic sensitivity analysis, stochastic dynamics and seismic reliability analysis, health monitoring of structures, vibration control, reliability analysis, and robust optimization.

About the Authors

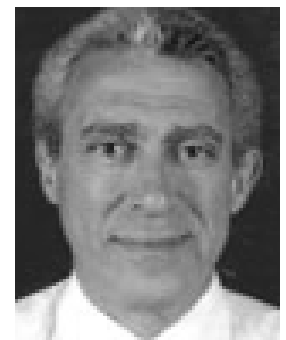
Fesmi Abdul Majeed is currently a PhD student in mechatronics engineering at University of Loughborough, United Kingdom. She received her Master's degree in control engineering from University of Sheffield, UK and her bachelor's degree in electrical and electronics engineering from NITC, India. She worked at the Petroleum Institute in Abu Dhabi, UAE (2009–2012) as a research assistant as part of her PhD research project. Her research areas are vibrations in rotary drilling, sensor technologies, adaptive and self-tuning control, and failure and fault detection in mechanical systems.

Hamad Karki is currently Assistant Professor in the Mechanical Engineering Department at the Petroleum Institute in Abu Dhabi, UAE. He obtained his bachelor's, Master's, and PhD (2008) in mechatronics engineering from Tokyo University of Technology, Japan. His research interests are mainly mobile and manipulator robots and vibrations of drilling for oil.



Mansour Karkoub received a BS degree in mechanical engineering with highest distinction in 1984, MSME in 1990, and PhD in 1994 all from the University of Minnesota, Minneapolis, Minnesota. He held a faculty position at Kuwait University from 1994–005 and at INRIA, France, from 2002–2003. Also, he held a faculty position at the Petroleum Institute in Abu Dhabi, UAE from 2005–2009. He has been with the Mechanical Engineering Department, Texas A&M University, Qatar, since 2009. His research interests are robust control, robotics, mechatronics, and vibration engineering.

Youssef Abdel-Magid is currently Professor and Dean of Engineering at the Petroleum Institute in Abu Dhabi, UAE. He received his Master's and PhD degrees from University of Manitoba in the years 1972 and 1976. He received his bachelor's from Cairo University in 1969. Prior to joining the Petroleum Institute, he held a faculty position at KFUPM, Saudi Arabia, from 1985 to 2004. His research expertise is in the areas of adaptive and robust control, applications of artificial intelligence techniques in controller design, and power system optimization and control.



C. S. Jog obtained his PhD from the Theoretical and Applied Mechanics Department at the University of Illinois at Urbana-Champaign in 1994 and has been on the faculty of the Mechanical Engineering Department at the Indian Institute of Science, Bangalore, since 1997. He has authored a book Foundations and Applications of Mechanics: Volume I: Continuum Mechanics; Volume II: Fluid Mechanics, Alpha Science Intl. Ltd., 2007. His main research interests are in the areas of developing finite-element based methodologies for structures, fluids, and their interaction.



Phil Picton is Professor of Intelligent Computer Systems, and from 2005 to 2010, he was Head of Engineering at the University of Northampton, United Kingdom. He has a considerable research record in the area of artificial intelligence and neural networks. In particular, he has worked on multidisciplinary projects in which artificial intelligence has been applied to a wide range of problems. For the last five years, he has been working with the British Institute of Non-Destructive Testing (BINDT) to produce a distance-taught degree in non-destructive testing on which he teaches ultrasonic testing, radiographic testing, and vibration monitoring and analysis. He has published over 100 papers and written two books.

Stefan Kaczmarczyk is Professor of Applied Mechanics at the University of Northampton, United Kingdom. He has an extensive international track record in research and consulting in the area of dynamics and vibration, with particular applications in vertical transportation and material handling systems. He has published over 80 journal and international conference papers and co-authored a book in this field. For the last 10 years, Professor Kaczmarczyk has been leading the Postgraduate Programme in Elevator Engineering at the University of Northampton. He has been invited to speak at national and international meetings and to serve on the scientific committee of a number of international conferences.

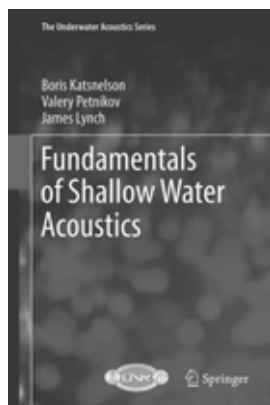


Fundamentals of Shallow Water Acoustics

By: Boris Katsnelson, Valery Petnikov, and James Lynch
Springer, 2012, 540 p., 202 illus., Hardcover
ISBN: 978-1-4419-9777-7
Price: US \$169

This book provides an analytical approach to low- and medium-frequency underwater acoustics in continental shelf areas. The foreword describes the purpose of the book in terms of a remedy for what other textbooks dedicated to the subject of low-frequency shallow water acoustics lack. Hence, the focus is filling the gap by supplying comprehensive information of relevance to shallow water acoustics. This book begins with a thorough description of significant environmental features such as variable topography, oceanographic fronts, and internal waves. Subsequent analysis demonstrates that these features are of primary importance rather than secondary issues in shallow water acoustics.

Shallow water acoustic propagation is analysed using normal modes to represent the dominant physical acoustical features in shallow water. It is shown that this is more informative in shallow water than the ray-tracing and parabolic equation approaches adopted in deep water underwater acoustics. The modus operandi is the calculation of the acoustical field as a function of range, depth, and time. The approach is initially derived for the simplest case known as the “Pekeris waveguide” then progressively extended to cases with variable sound speed profile, depth, and sediment properties. One particular feature, uncovered by the analysis, is the differing group velocity between the acoustical modes in typical shallow water environments at low frequency. Measurement results are



provided to show how this leads to different arrival times of the modes. Furthermore, mathematical explanations are provided for the dependency of the attenuation of the modes as a function of environmental properties and frequency. At one juncture, it is noted that both theory and measurement indicate that the absorption in the water column is relatively small, such that it can be ignored in shallow water at the frequencies discussed in this monograph. Oceanographic measurement activities are described and used as the basis for application of the mathematics. Examples are supplied from the Barents Sea to the north of Russia and the Atlantic Ocean to the east of the USA. Reworking these examples would enable readers to confirm that they have understood the analysis.

A key implication from the analysis is that sonar equipment, signal-processing techniques, and acoustical transmissions designed for deep water application may exhibit unexpected characteristics in shallow water environments. For example, the varying time delay and absorption of the modes are likely to cause an active sonar system to receive multiple echoes from the same target—potentially leading to a false estimate of range. An understanding of the environment and usage of the mathematics would enable the received signal to be better understood and the target better defined. However, the level of mathematics used in this book goes well beyond the Fourier theory and introductory time-series analysis. For example, solutions to the wave equation are sought using eigenvalues of the Sturm-Liouville form on the assumption that readers are familiar with the approach. Contour integration in the complex plane is also employed as an analysis technique. Readers lacking strong graduate-level mathematical abilities would derive limited benefit from this book.

In summary, this book provides the mathematics and supporting evidence needed to gain an understanding of low-frequency shallow water acoustics. Applying this book to real problems will be an intellectual challenge, but a potentially worthwhile alternative to using deep water models.

Adrian Brown

*Defence Science & Technology Laboratory
Portsmouth, Hampshire, UK*